

# **EVALUATION OF A GAMMA TITANIUM ALUMINIDE FOR HYPERSONIC STRUCTURAL APPLICATIONS**

A Thesis  
Presented to  
The Academic Faculty

by

Carrell Elizabeth Weeks

In Partial Fulfillment  
Of the Requirements for the Degree  
Master of Science in Mechanical Engineering

Georgia Institute of Technology  
May 2005

# **EVALUATION OF A GAMMA TITANIUM ALUMINIDE FOR HYPERSONIC STRUCTURAL APPLICATIONS**

Approved by:

Dr. W. Steven Johnson, Advisor  
School of Materials Science and Engineering  
School of Mechanical Engineering  
*Georgia Institute of Technology*

Dr. Erian Armanios  
School of Aerospace Engineering  
*Georgia Institute of Technology*

Dr. Christopher Lynch  
School of Mechanical Engineering  
*Georgia Institute of Technology*

Date Approved: April 11, 2005

*In loving memory*

*of*

*my “Pops”*

*Charles Harold Allen*

*June 16, 1924 – February 9, 2005*

*With gratitude for his gift of my education*

*and*

*for teaching me to value it*

## ACKNOWLEDGEMENTS

There are many people I would like to thank and acknowledge for their support and help during this research effort. First of all, I would like to thank my advisor, Dr. Steven Johnson, for his guidance and assistance throughout this chapter of my career. His constantly open door, concern for my best interests, and technical guidance have been integral to furthering my engineering education. In addition to my advisor, I would like to thank Dr. Erian Armanios and Dr. Christopher Lynch for being on my thesis committee.

I owe many thanks to Rick Brown for keeping my machines running and my specimens glowing, as well as patiently answering my numerous technical questions and letting me know where to find good Cajun cooking this far from home. I would like to thank former graduate student Dr. Ben Church for volunteering his time and helping me with the dilatometry equipment, as well as processing my data from the thermal expansion testing. I would also like to thank graduate students Kip Findley and Heather Major Sharpe for helping me use the cutting and polishing equipment, finding an oven for my specimens, and providing constant encouragement. I thank the staff in the Mechanical Engineering Machine Shop for working with me and machining my samples.

Many thanks go out to Keith Bird of the Metals and Thermal Structures Branch at NASA Langley Research Center for hosting my visit to those facilities and providing technical supervision of this project. Additionally, I must thank NASA LaRC for their generous funding and support, which made this project possible.

Next, I would like to thank my fellow MPRL researchers for providing not only technical advice and help in locating various tools and parts, but also for their support and companionship. I want to thank Matt Hammond for readily helping me with alignment issues, random leaks, and various other technical problems. To Shelby Highsmith I give my most heartfelt gratitude for his constant support and friendship; for entertaining me and getting me through all of my Atlanta ordeals with a helping hand and a friendly beverage.

Finally, my warmest thanks go to the rest of my friends here in Atlanta and elsewhere, especially Christie, for their continuing support. And most importantly, I thank my family for all the support and love they have given me throughout the years. My dad inspired my engineering career with answers to all my questions about how things work. My mom constantly provides encouragement and sends wonderful Louisiana cooking my way. My siblings Stephen, Paul, Andrew, and Katie give me invaluable support and advice. With visits, e-mails, phone calls, and joyous holiday get-togethers, they and my extended family have inspired and encouraged me in all of my accomplishments. I strive to make them proud in all of my endeavors.

## TABLE OF CONTENTS

ACKNOWLEDGEMENTS .....	iv
LIST OF TABLES .....	viii
LIST OF FIGURES .....	ix
LIST OF SYMBOLS .....	xii
SUMMARY .....	xvi
CHAPTER 1    INTRODUCTION .....	1
CHAPTER 2    BACKGROUND .....	4
2.1    Hypersonic Flight Programs and Applications .....	4
2.1.1 <i>The Vision for Space Exploration [2]</i> .....	7
2.1.2 <i>Thermal Protection Systems</i> .....	7
2.2    Other High Temperature Applications .....	11
2.3    Metal Matrix Composites.....	12
2.3.1 <i>Titanium Matrix Composites</i> .....	17
2.3.2 <i>Modeling MMC Behavior</i> .....	20
2.3.2.1 <i>AGLPLY</i> .....	21
2.4    Gamma Titanium Aluminides.....	23
2.4.1 <i>History of Gamma Titanium Aluminide Development</i> .....	24
2.4.2 <i>General Properties</i> .....	25
2.4.3 <i>Properties After High Temperature Exposure</i> .....	30
2.5    Gamma MET.....	31
2.5.1 <i>Mechanical Properties</i> .....	32
2.5.2 <i>Oxidation Behavior</i> .....	36
CHAPTER 3    MATERIAL.....	39
3.1    Gamma-MET Rolled Sheet Material .....	39
3.2    Foil Matrix Material.....	42
3.3    SCS-6 and Ultra-SCS Silicon Carbide Fibers.....	47

3.4	Nextel 610 Alumina Fiber.....	48
CHAPTER 4 ANALYTICAL AND EXPERIMENTAL METHODS .....		50
4.1	Experimental Equipment and Procedures.....	50
4.1.1	<i>Dilatometry</i> .....	50
4.1.2	<i>Microscopy</i> .....	52
4.1.3	<i>Mechanical Testing Equipment</i> .....	53
4.1.3.1	<i>Mechanical Testing Procedures</i> .....	57
4.2	Manufacturing at NASA LaRC.....	59
4.3	Analytical Modeling Using AGLPLY .....	62
CHAPTER 5 RESULTS AND DISCUSSION.....		65
5.1	Experimental Tests.....	65
5.1.1	<i>Coefficient of Thermal Expansion</i> .....	65
5.1.2	<i>Poisson's Ratio</i> .....	67
5.1.3	<i>Tensile Testing</i> .....	68
5.1.4	<i>Fractography</i> .....	78
5.2	Analytical Predictions .....	79
5.2.1	<i>Material Parameters</i> .....	80
5.2.2	<i>Calculating the "Lock-up" Temperature</i> .....	83
5.2.3	<i>Residual Stresses</i> .....	84
5.2.4	<i>Subsequent Monotonic Loading Capabilities</i> .....	88
5.3	Manufacturing at NASA LaRC.....	92
CHAPTER 6 CONCLUSIONS.....		96
CHAPTER 7 RECOMMENDATIONS .....		100
REFERENCES .....		102

## LIST OF TABLES

Table 2.1: Tensile properties of Ti-46.5Al-4(Cr,Nb,Ta,B)at.% .....	32
Table 5.1: Material properties results from load control testing.....	70
Table 5.2: Material properties results from displacement control testing.....	72
Table 5.3: Material properties comparison for exposed and unexposed specimens .....	77
Table 5.4: $\gamma$ -MET material parameters used in AGLPLY simulations .....	82
Table 5.5: Ultra-SCS material parameters used in AGLPLY simulations .....	82
Table 5.6: Nextel 610 material parameters used in AGLPLY simulations [90, 91].....	82
Table 5.7: Overall laminate properties of $[0]_4$ Ultra-SCS/ $\gamma$ -MET .....	89
Table 5.8: Overall laminate properties of $[0]_4$ Nextel 610/-MET .....	91



## LIST OF FIGURES

Figure 2.1: X-15 research vehicle and X-30 National Aerospace Plane (NASA photos) ..	5
Figure 2.2: Experimental (X) demonstrators: (a) the X-33, (b) the X-34, and (c) the X-37 (NASA photos) .....	6
Figure 2.3: B-52B takes off and Pegasus booster rocket ignites to send the X-43A on its record setting flight on Nov. 16, 2004. (NASA photos) .....	6
Figure 2.4 Current Shuttle Thermal Protection System Layout.....	8
Figure 2.5: Thermal protection system concepts [16].....	9
Figure 2.6: X-33's Inconel 617 TPS panel [17].....	10
Figure 2.7: Truss core of TiAl sheet made by BF Goodrich Aerospace [18].....	11
Figure 2.8: $\gamma$ -TiAl turbine wheel casting by Howmet Corporation [18].....	12
Figure 2.9: Longitudinal stress-strain diagram of a continuous fiber MMC [21].....	13
Figure 2.10: Longitudinal stress-strain response of a cross-ply MMC [21].....	14
Figure 2.11: Coefficient of thermal expansion mismatch causing residual stresses.....	16
Figure 2.12: Ultimate strength for a) several titanium alloys and b) their composite systems [23] .....	18
Figure 2.13: AGLPLY ply coordinate system [46].....	22
Figure 2.14: Central part of the equilibrium Ti-Al phase diagram [64] .....	26
Figure 2.15: Mechanical property trends of gamma TiAl based alloys with test temperature and microstructure [61].....	28
Figure 2.16: Trends in strength and elongation of Ti-46.5Al-4(Cr,Nb,Ta,B)at.% as function of temperature [81] .....	33
Figure 2.17: S-N curves at RT and 700C of Ti-46.5Al-4(Cr,Nb,Ta,B)at.% with two different heat treatments [77].....	34
Figure 2.18: Creep curves for Ti-46.5Al-4(Cr,Nb,Ta,B)at.% at 700°C and 800°C and a stress of 200 MPa [77] .....	34

Figure 2.19: Stress intensity range vs. crack extension for PA microstructure of $\gamma$ -MET [82].....	35
Figure 2.20: $da/dN$ vs. $\Delta K$ curves for both PA (denoted FG) and DFL microstructures of $\gamma$ -MET [82].....	36
Figure 2.21: Isothermal mass gain per unit area of samples oxidized for 48 hours at various temperatures [79].....	37
Figure 2.22: Oxide chemical composition vs. distance at 800°C [79].....	38
Figure 3.1: Micrograph of etched $\gamma$ -MET sheet material [79].....	40
Figure 3.2: Dogbone coupon of the sheet material .....	41
Figure 3.3: RF plasma spray deposition facility at NASA LaRC: (a) schematic of plasma torch and (b) superstructure [80].....	44
Figure 3.4: Thin sheets of foil produced by plasma spray deposition of pre-alloyed powers ready for VHP consolidation .....	45
Figure 3.5: Flaws in the consolidated “fiberless” panels included: a) surface asperity, b) delaminated sections, and c) surface markings [79] .....	46
Figure 3.6: Monotonic results of consolidated material at 21°C: a) load control test b) strain control test [79] .....	47
Figure 3.7: Cross-sectional diagrams of the Ultra-SCS fiber [26].....	48
Figure 4.1: Dilatometry laboratory configuration with data acquisition .....	51
Figure 4.2: Servo-hydraulic Test Frame and peripheral equipment .....	53
Figure 4.3: Induction coil used in testing program, with susceptors heated and glowing .....	55
Figure 4.4: IN-718 susceptors with thermocouple welded to outside (top) and groove for specimen thermocouples (bottom) .....	57
Figure 4.5: Fiber mat (a) before and (b) after removal of every other fiber .....	60
Figure 4.6 Vacuum hot press facility: (a) lay-up on molybdenum die, (b) die on molybdenum platens in furnace, (c) closed furnace chamber and controls .....	61
Figure 4.7: Typical VHP temperature/force profile [80] .....	62
Figure 5.1: Coefficient of thermal expansion vs. temperature for 3 specimens .....	66
Figure 5.2: Average measured CTE with the linear interpolation of the data used in AGLPLY simulations .....	67

Figure 5.3: Poisson's ratio measured at room temperature under cyclic loading .....	68
Figure 5.4: Stress-strain curves of sheet material from load control testing.....	70
Figure 5.5: Stress-strain curves of sheet material from displacement control testing .....	72
Figure 5.6: Stress-strain curve comparisons of unexposed specimens and specimens exposed to 700°C for 5 hours.....	74
Figure 5.7: Stress-strain curve comparisons of unexposed specimens and specimens exposed to 800°C for 5 hours.....	75
Figure 5.8: Cross-sectional fracture surfaces of material tested at room temperature in conditions: a) unexposed and b) exposed to 800°C for 5 hours.....	78
Figure 5.9: Matrix residual axial stress due to thermal mismatch for various fiber volumes of an [0]4 Ultra-SCS/ $\gamma$ -MET composite .....	85
Figure 5.10: Matrix residual axial stress due to thermal mismatch for various fiber volumes of an [0]4 Nextel 610/ $\gamma$ -MET composite .....	87
Figure 5.11: Generic hypersonic flight profile [45].....	88
Figure 5.12: Cracking in [0]2 SCC-6/ $\gamma$ -MET panel (VHP-110) after consolidation .....	93
Figure 5.13: Cross-sectional view of composite samples a) VHP 110 and b) VHP 113..	94

## LIST OF SYMBOLS

$\alpha$	coefficient of thermal expansion
$\epsilon$	strain
$\sigma$	stress
$\nu$	Poisson's ratio
$\gamma$ -MET	commercial name for Ti-46.5Al-4(Cr,Nb,Ta,B)at.% alloy
ASRP	advanced sheet rolling process
ASTM	American Society for Testing and Materials
at.%	atomic percent
BDTT	brittle-ductile transition temperature
$^{\circ}\text{C}$	degrees Celsius, unit measure of temperature
cm	centimeters, unit measure of length - $10^{-2}$ meters
CVD	chemical vapor deposition
CTE	coefficient of thermal expansion
DFL	designed fully lamellar microstructure
DP	duplex microstructure
E	Young's modulus
EDM	electron discharge machining
EDX	electron dispersive x-ray
$^{\circ}\text{F}$	degrees Fahrenheit, unit measure of temperature
f	subscript designation for fiber properties
FCG	fatigue crack growth

g	gram, unit measure of mass
GPa	gigapascal, unit measure of stress - $10^9$ Pascals
GTRI	Georgia Tech Research Institute
HCF	high cycle fatigue
HIP	hot isostatic pressing
hrs	hour, unit measure of time - 3600 seconds
ksi	kilopounds-force/inch <sup>2</sup> , unit measure of stress - $10^3$ psi
IHPTET	Integrated High Performance Turbine Engine Technology
ISS	International Space Station
L	subscript designation for overall laminate properties
LaRC	Langley Research Center, Hampton, VA
lb <sub>f</sub>	force pound, unit measure of force
LCF	low cycle fatigue
LVDT	linear variable differential transformer
m	subscript designation for matrix properties
μm	micrometer, unit measure of length – $10^{-6}$ meters
min	minute, unit measure of time – 60 seconds
mm	millimeter, unit measure of length – $10^{-3}$ meters
mm/mm	unit measure of strain
ME	mechanical engineering
MMC	metal matrix composite
MPa	megapascal, unit measure of stress – $10^6$ Pascals
MPRL	Material Properties Research Laboratory, Georgia Tech

MSE	material science engineering
MTS	Mechanical Testing and Simulation, company
N	Newton, unit measure of force
NASA	National Aeronautics and Space Administration
NASP	National Aero-Space Plane
NG	near gamma microstructure
NIST	National Institute of Standards and Testing
NL	near lamellar microstructure
Pa	Pascals, unit measure of stress
PA	primary annealed microstructure
PMC	polymer matrix composite
P/M	powder metallurgy
RD	roll direction
RLV	Reusable Launch Vehicle
RT	room temperature
sec	seconds, unit measure of time
SEM	scanning electron microscope
SSTO	single stage to orbit
T	temperature
TMC	titanium matrix composite
TMF	thermomechanical fatigue
TPS	thermal protection system
UTS	ultimate tensile strength

$v_f$	fiber volume fraction
VHP	vacuum hot press
YS	yield strength

## SUMMARY

Titanium matrix composites (TMCs) have been extensively evaluated for their potential to replace conventional superalloys in high temperature structural applications, with significant weight-savings while maintaining comparable mechanical properties. New gamma titanium aluminide alloys and an appropriate fiber could offer an improved TMC for use in intermediate temperature applications (400-800°C). The purpose of this investigation is the evaluation of a gamma titanium aluminide alloy with nominal composition Ti-46.5Al-4(Cr,Nb,Ta,B)at.% as a structural material in future aerospace transportation systems, where very light-weight structures are necessary to meet the goals of advanced aerospace programs.

Mechanical characterization testing of the alloy was performed over the potential usable temperature range. Thermal expansion behavior of the alloy was evaluated, as thermal mismatch of the constituents is an expected problem in composites employing this matrix material. Monotonic testing was conducted on rolled sheet material samples of the alloy at room temperature, 700°C, and 800°C to obtain material properties. The alloy exhibited good strength and stiffness retention at elevated temperatures, as well as improved ductility. The modulus degraded by 20% and 30% at 700°C and 800°C respectively. Yield strength similarly degraded by 20% and 27% at the two elevated temperatures, while ultimate strength only degraded by 4% and 17% respectively. The ductility, on the other hand, increased from less than 1% elongation to 2.7% at 700°C and over 20% at 800°C.



Monotonic testing was also conducted on specimens exposed to elevated temperatures (700°C and 800°C) for 5 hours to determine the degradation effects of high temperature exposure and oxidation. The exposure did not significantly affect the alloy properties at elevated temperatures, although some slight improvement was observed. The materials were tested at the same temperatures at which they were exposed. The modulus of the exposed specimens remained the same as the unexposed specimens at 700°C and increased by 8% at 800°C. Yield strength improved by about 10% at 700°C and 3% at 800°C. Ultimate strength was increased by less than 2% at each temperature. Ductility decreased from 2.7% elongation to 2.2% elongation at 700°C, but remained above 20% for the exposed specimen at 800°C. For the room temperature testing the same increases in strength and stiffness were observed for the exposed specimens compared to the unexposed specimens. The specimen exposed to 700°C had a negligible increase in modulus, a 12% increase in yield strength, and a 5% increase in ultimate strength. The specimen exposed to 800°C exhibited a 6% increase in modulus, a 6% increase in yield strength, and a 10% increase in ultimate strength. Room temperature ductility, however, decreased for specimens exposed to either elevated temperature, by 54% and 28% for the exposures at 700°C and 800°C respectively. The exposure significantly decreased the already low room temperature ductility.

Analytical modeling using AGLPLY software was conducted to predict the residual stress state after composite consolidation due to thermal mismatch as well as the potential mechanical behavior of  $[0]_4$  laminates with a  $\gamma$ -MET matrix. Silicon carbide (Ultra-SCS) and alumina (Nextel 610) fibers were selected as potential reinforcing materials for the analysis. High residual stresses were predicted due to the thermal mismatch in the

materials. Laminates with Nextel 610 fibers were found to offer the best potential for a composite in this comparison, because they are a better thermal match for the matrix. Coupons of SCS-6/ $\gamma$ -MET were manufactured with different volume fractions. Both manufacturing attempts resulted in transverse cracking in the matrix from the residual thermal stress.

## **CHAPTER 1**

### **INTRODUCTION**

On March 27, 2004, the X-43A research vehicle made aviation history with the first successful flight of a scramjet powered airplane at hypersonic speeds, reaching a test speed of Mach 7. A little over half a year later, the last X-43A vehicle, with extra thermal protection, bested its predecessor's record by flying at nearly Mach 9.8, demonstrating the present and immediate future of hypersonic flight. The ultimate applications of this technology include hypersonic airplanes and next generation reusable launch vehicles (RLVs). An integral component of these applications will be more durable thermal protection systems (TPS) that can endure the extreme environments of hypersonic flight. For example, on February 1, 2003, the space shuttle Columbia and its crew of 7 astronauts were tragically lost during re-entry. Investigations into this disaster led to the conclusion that pieces of foam insulation broke off from the fuel tank during take-off and impacted the left wing, damaging the carbon-carbon TPS tiles there [1]. This tragedy reminds us of the dangers present in space flight, and the need to develop technologies to increase the safety and reduce costs associated with space missions.

In the President's Vision for Space Exploration, announced in February 2004, he emphasizes that:

Preparing for exploration and research accelerates the development of technologies that are important to the economy and national security. The space missions in this plan require advanced systems and capabilities that will accelerate the development of many critical technologies including power, computing, nanotechnology, biotechnology, communications, robotics, and materials [2].

Development of light-weight, high strength materials systems for TPS are necessary to reach the goals set forth in this program. The National Aeronautical and Space Administration (NASA) is evaluating several different advanced material systems to improve the durability of the TPS and prevent incidents like the Columbia tragedy. Current materials systems under investigation include nickel superalloys, nickel aluminides, iron aluminides, and titanium aluminides.

Titanium aluminides and their composites are promising candidates as advanced structural materials for high temperature application because of their attractive combination of low density, oxidation resistance, high modulus, and strength retention at elevated temperatures [3-6]. They offer a significant weight-savings and similar mechanical performance characteristics compared to nickel superalloys, which can help attain weight-savings and cost reduction goals in future RLVs. The purpose of this research is to evaluate a potential candidate material, an advanced gamma titanium aluminide alloy, to provide a better understanding of the mechanical behavior of this material, as well as the behavior of composite systems with this matrix material.

The main objectives of this research were to evaluate the mechanical properties of this alloy, and incorporate that data into modeling of composite laminates to assess the feasibility and performance of these systems at temperatures encountered during hypersonic flight. Monotonic tensile testing was performed on the alloy over a range of temperatures from 21°C-800°C. Thermal expansion testing was also performed in order to fully characterize the alloy for modeling. In an effort to determine the usable temperature range, tensile experiments were performed on materials that had been exposed to elevated temperatures in order to characterize the degradation effects of

oxidation. The mechanical property data was implemented into a composite laminate code to analytically determine the stress-strain response of the constituents and predict overall laminate behavior. This data was used to determine the feasibility of manufacturing various composite systems. Finally, attempts were made to manufacture samples of a composite system using this matrix material.

The remainder of this thesis is divided into six chapters. Chapter 2 provides the motivation and historical background information relevant to this research and these systems. Chapter 3 describes the alloy with respect to its composition, microstructure, and manufacturing processes, as well as detailing the geometry of the test specimens. The fibers considered for use in composite systems are also described. Chapter 4 gives descriptions of all test equipment and experimental procedures used during testing. It also discusses the analytical model used. Chapter 5 presents the results from the experimental testing, the analytical modeling, and the attempts at composite manufacturing. The results are summarized and discussed in Chapter 6, and the major conclusions are listed. Chapter 7 provides recommendations for future work in this field of research.

## **CHAPTER 2**

### **BACKGROUND**

Gamma titanium aluminides and titanium matrix composites (TMCs) have received increased attention over the past 20 years as hot structural materials in the aerospace industry as well as in other high temperature applications. The following chapter explains some of the motivation behind the research efforts into lightweight, high strength and stiffness materials for various high temperature applications. It also discusses some of the previous research and development of TMCs and gamma alloys as well as the status quo of the technologies.

#### **2.1 Hypersonic Flight Programs and Applications**

NASA has a continuing need to develop new technologies to deliver payloads into orbit at reduced risk and cost. The technologies of particular interest to this research are high temperature structural materials (hot structures) for hypersonic vehicles; these are structures that do not require a separate thermal protection system (TPS).

Hot structures for hypersonic vehicles debuted in the late 1950s with the X-15, the first hypersonic research vehicle [7, 8]. It employed an Inconel-X and titanium alloy metallic primary structure in a heat-sink design. Development in hot structures technologies refocused under the ambitious X-30, or National Aerospace Plane (NASP), program which was initiated in 1987 to accelerate technologies for space flight (see Figure 2.1). It was originally conceived as a feasibility study for a single-stage-to-orbit (SSTO) airplane which could take off and land horizontally [9]. This program considered

technologies ranging from air-breathing scramjet engines to advanced materials including various metal matrix composites (MMCs), titanium-based alloys, and TMC skin structures for thermal protection. However, the NASP program was canceled in 1993 due to high costs and concerns with the complexity of systems.



Figure 2.1: X-15 research vehicle and X-30 National Aerospace Plane (NASA photos)

The NASP program was followed by series of experimental (X) technology demonstrators (see Figure 2.2) aimed at lowering launch costs from \$10,000 to \$1,000 per pound. They were to demonstrate technologies, including advanced material systems, for use in second generation Reusable Launch Vehicles (RLVs). Future RLV's will require a greatly improved TPS to achieve the ambitious goal of reducing the cost of delivering a payload to orbit by an order of magnitude. The X-33, initiated in 1996, considered Inconel 617 and various titanium based alloys for its TPS [10]. The X-34, also started in 1996, was to have all composite primary and secondary structures, including lightweight metal matrix composite airframe structures and advanced thermal protection systems [11]. However, upon progress evaluation, both the X-33 and X-34 programs were concluded in 2001 as the investment costs began to outweigh the benefits.

The X-37, begun in 1999, was created to demonstrate technology as it operates in the orbital, re-entry, and landing phases of flight [12].

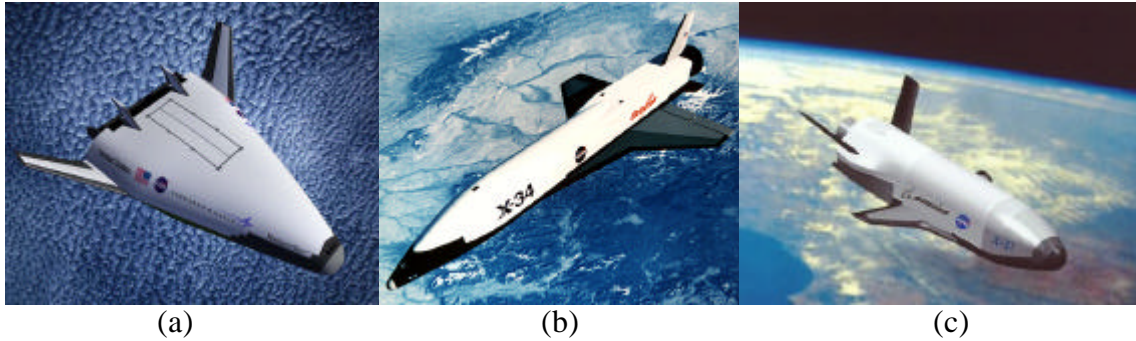


Figure 2.2: Experimental (X) demonstrators: (a) the X-33, (b) the X-34, and (c) the X-37 (NASA photos)

NASA's X-43A recently made aviation history with its first successful flight of a scram-jet powered airplane at hypersonic speeds in March 2004 [13]. The research vehicle (see Figure 2.3) broke its own record in mid-November 2004, flying at nearly Mach 9.8, demonstrating the present and immediate future of hypersonic flight, with its accompanying need for advanced lightweight material systems.



Figure 2.3: B-52B takes off and Pegasus booster rocket ignites to send the X-43A on its record setting flight on Nov. 16, 2004. (NASA photos)



### ***2.1.1 The Vision for Space Exploration [2]***

In January 2004, President George W. Bush announced a new “Vision for Space Exploration” that involves human and robotic missions to the Moon and eventually to Mars and beyond. The vision sets forth goals that include: returning the Space Shuttle safely to flight, completing the International Space Station (ISS), sending robotic and then human expeditions to the Moon, and conducting robotic expeditions to Mars in preparation for future human expeditions. The Presidential Commission for implementation of this policy identified as one of seventeen “enabling technologies” critical to attainment of these objectives:

Advanced structures – extremely lightweight, multi-function structures with modular interfaces, the building block technology for advanced spacecraft [14].

Clearly, investigation into lightweight, high temperature materials, such as gamma titanium aluminides, advances these goals. It is necessary to investigate new, lightweight, durable materials for use on future hypersonic aircraft.

### ***2.1.2 Thermal Protection Systems***

In considering new materials for thermal protection systems, it is useful to begin with the current Space Shuttle TPS layout as a reference (see Figure 2.4). The primary structure is made of aluminum, and requires a thermal protection system to protect it from the extreme conditions encountered during flight – the leading edge surfaces can reach temperatures up to 3000°F during re-entry. The present silica tile and flexible ceramic blanket thermal protection system, applied to the majority of the shuttle surface, allows a decoupling of the structural design from the TPS to a large degree. However, the need for a separate TPS results in increased weight as well as high costs associated

with maintenance and repair. In one study, the maintenance burden for the thermal protection system was estimated at nearly 32,000 hours per mission [15].

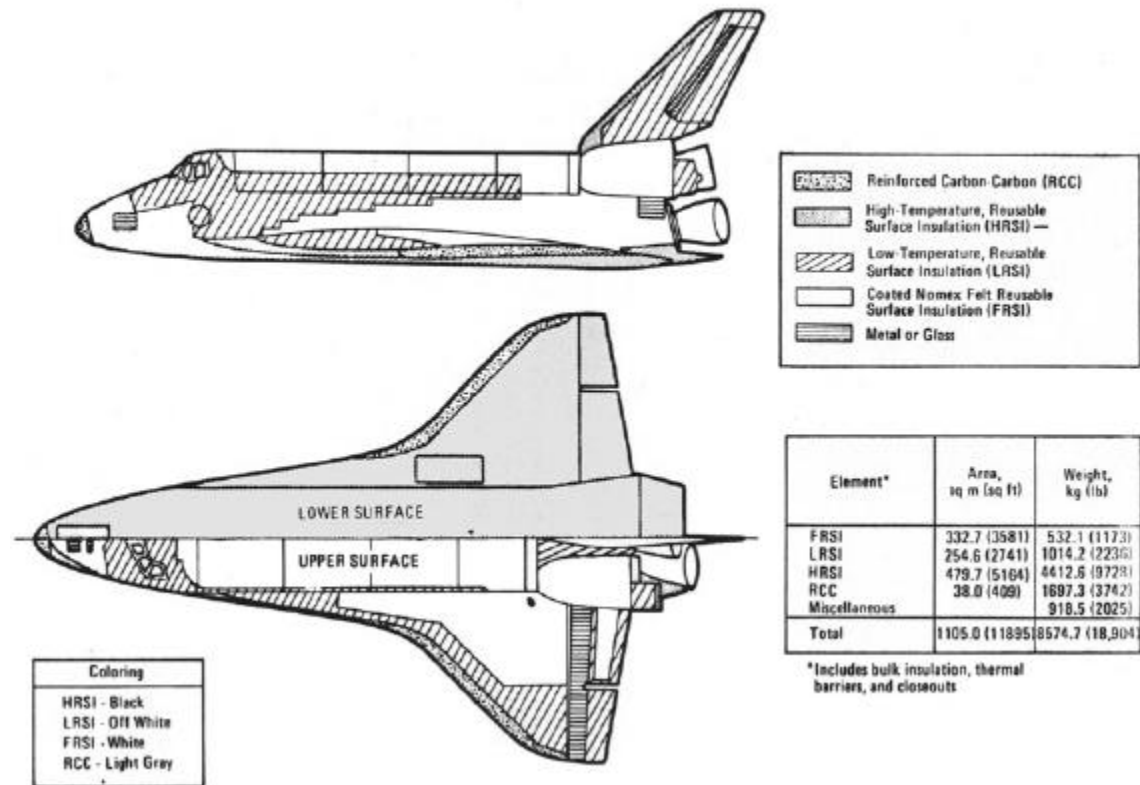


Figure 2.4 Current Shuttle Thermal Protection System Layout

Other concepts considered for thermal protection systems (see Figure 2.5) can be categorized into three groups: passive, semi-passive, and active. The latter groups include concepts for active cooling of the structure, whereas a passive TPS employs high temperature structural materials, such as hot structures. The use of hot structures technology, materials that meet structural requirements in addition to withstanding high temperature conditions, is desirable because of its simplicity. This technology allows for design without a separate TPS, saving size and weight. In addition, hot structures can be

readily inspected. They offer good potential because they could possibly be designed to be damage tolerant using standard aircraft design practices [7].

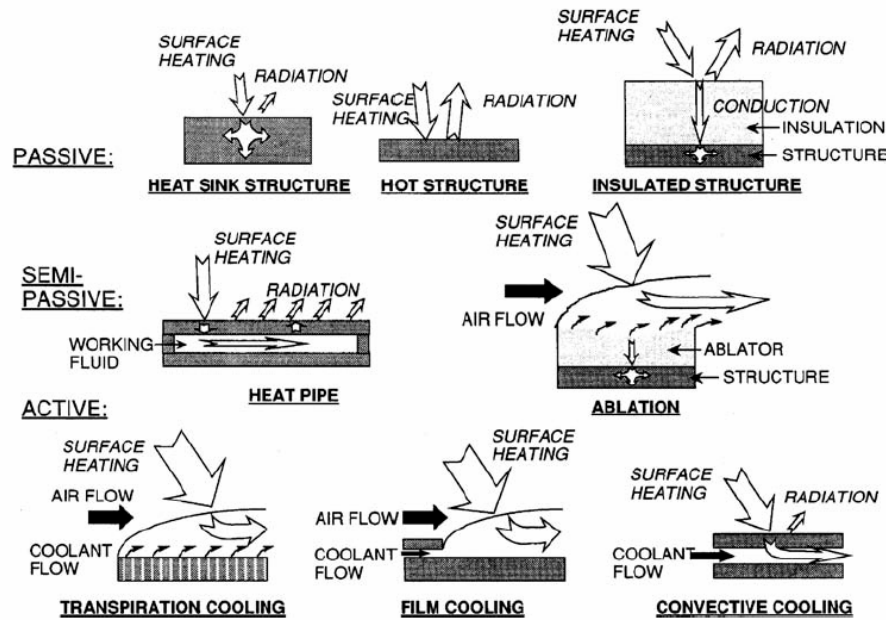


Figure 2.5: Thermal protection system concepts [16]

High temperature metallic materials, such as iron, nickel and titanium aluminide intermetallics, and their composites are candidates for hot structures TPS. For example, the panels that made up the TPS on the X-33's underside were made with Inconel 617 (see Figure 2.6). These metallic panels are easily installed and removed, reducing costs associated with maintenance and repair.



Figure 2.6: X-33's Inconel 617 TPS panel [17]

Superalloys are generally considered for these applications because of their excellent creep, strength, toughness, oxidation resistance, and general long-term stability at temperature. However, those materials tend to be relatively heavy. Lower density high temperature metals currently in development could replace conventional superalloys in future metallic TPS concepts. For example, BF Goodrich Aerospace successfully manufactured a truss core of  $\gamma$ -TiAl sheet from separately formed corrugations. Covering the top and bottom with face sheets of the same material results in the Figure 2.7 cross sections, which look like a corrugated box. This production process supports the potential use of TiAl for the skin of a future hypersonic vehicle [18].

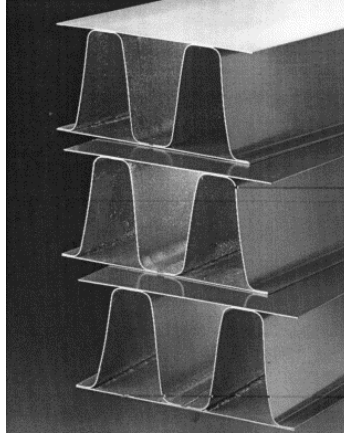


Figure 2.7: Truss core of TiAl sheet made by BF Goodrich Aerospace [18]

## 2.2 Other High Temperature Applications

As a hot structural material, gamma titanium aluminides are attractive for several other high temperature applications in the 550-750°C service range. They have been reviewed for use in turbine blades, turbine wheels (see Figure 2.8), engine components, and outlet-nozzles of large engines service in advanced turbine engines [18-20]. For example, in the design of the large exhaust nozzle of High Speed Civil Transport (HSCT) propulsion system, several critical components are fabricated from  $\gamma$ -TiAl: the divergent flame uses wrought gamma, the nozzle sidewall is a hybrid fabrication of both wrought gamma face sheet and cast gamma substructure [20]. However, these concepts are generally still in the development stage.

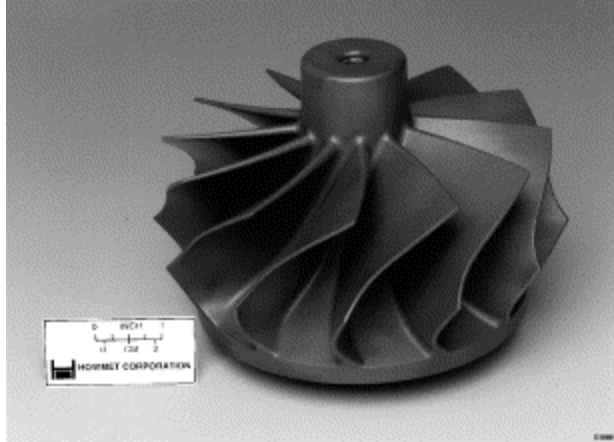


Figure 2.8:  $\gamma$ -TiAl turbine wheel casting by Howmet Corporation [18]

### 2.3 Metal Matrix Composites

For high temperature applications, metal matrix composites (MMCs) have an advantage over polymeric matrix composites (PMCs) in that metals typically have a higher yield strength, modulus, and maximum application temperature than polymers. MMCs consist of a high strength and stiffness reinforcing material embedded in a metallic matrix. These reinforcements are generally continuous fibers, discontinuous fibers (whiskers), or particulates.

Discontinuous reinforced composites mostly exhibit improved stiffness, but these reinforcements do little for improving strength. Continuous fibers, on the other hand, improve both the stiffness and strength of the laminate, as the fibers carry much of the load. Initially, under unidirectional tensile loading, both the fibers and the matrix deform elastically. At this stage, the longitudinal elastic modulus of the composite can be computed with the rule of mixtures (Equation 2.1)

$$E_L = E_f v_f + E_m v_m \quad (2.1)$$

where  $E$  is the Young's modulus,  $v$  is the volume fraction,  $f$  denotes the fiber properties,  $m$  denotes the matrix properties, and  $L$  denotes the overall laminate properties. From this equation, one could deduce that a metal matrix (which is stiffer and stronger by an order of magnitude) would contribute more to the stiffness and strength of a composite than would a polymer matrix. Continuing with the loading, generally the matrix will yield plastically while the fiber remains elastic, resulting in a reduced modulus (see Figure 2.9).

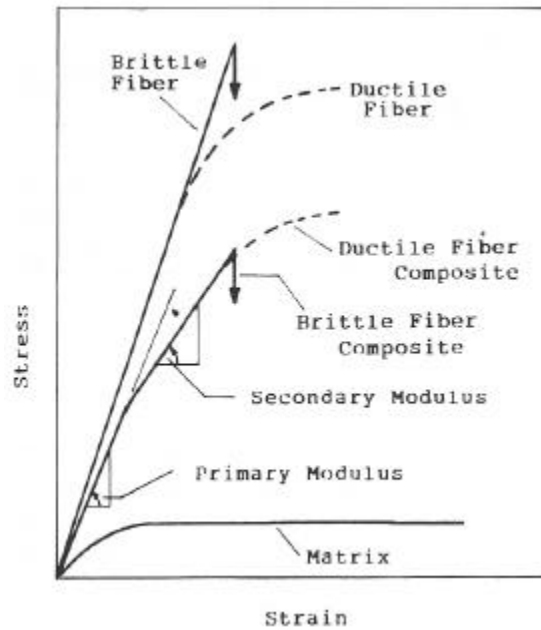


Figure 2.9: Longitudinal stress-strain diagram of a continuous fiber MMC [21]

When the fibers are oriented in the transverse direction,  $90^\circ$  from the loading directions, the fibers do not contribute much to the overall strength of the composite. They rather act as hard inclusions – and therefore stress concentrations, which lead to

matrix cracking and interface debonding. Cross-plyed laminates ( $0^\circ$  and  $90^\circ$  plies) exhibit a slightly nonlinear response to longitudinal loading, as can be seen in Figure 2.10. This is due to the failure of the  $90^\circ$  plies below the ultimate strain of the composite; this failure point is called the knee. The initial modulus is easily calculated using the rule of mixtures mentioned earlier. The secondary modulus is predicted by assuming that none of the  $90^\circ$  plies are carrying any load, so that only the  $0^\circ$  plies contribute to the modulus. The composite then fails at the ultimate strain of the  $0^\circ$  plies.

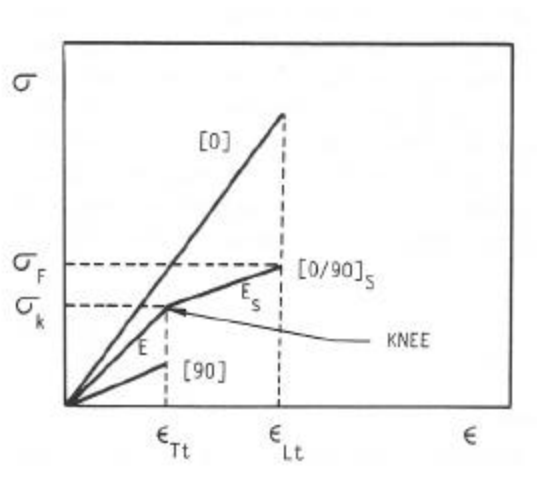


Figure 2.10: Longitudinal stress-strain response of a cross-plyed MMC [21]

The failure modes in MMCs can be grouped into four main categories [22]. The first, fiber dominated damage, is demonstrated in Figure 2.9; when the laminate strain reaches the ultimate strain of the brittle fiber, fractures in the fiber lead to composite failure. Matrix dominated damage occurs when the ultimate strain of the matrix is less than that of the fiber. In this case, the matrix cracks before the fibers such that the fibers must carry more load, reaching their ultimate stress more quickly, and leading to overall laminate failure. Or, during fatigue loading, cyclic yielding can cause fatigue damage and microcracking in the matrix, but not the fiber, leading to matrix-dominated damage.



When the strain to failure is similar for both the fiber and matrix, cracks tend to propagate through both equally, leading to another damage mechanism called self-similar crack growth. Finally, the interface between the fiber and matrix is sometimes weaker than either of the constituent materials. Interface failure is the result of debonding between the fiber and matrix, which can occur before either of the constituents fails.

As the metallic matrix contributes more to the strength of MMCs, they tend to have a more complex damage state than PMCs. When the brittle fibers and ductile matrix deform elastically, the behavior is relatively easy to predict using classical lamination theory. However, in MMCs, the overall composite deformation is complicated when the matrix deforms plastically, and subsequent composite behavior becomes more difficult to predict.

Additionally, since the matrix has an active contribution to the stress-strain behavior of MMCs, the fiber/matrix interface is a crucial aspect of the MMC behavior. Damage to the interface or debonding can occur under transverse tension and longitudinal shear loading. In MMCs chemical reactions at the constituent interface are also of great concern, during both processing and application. These systems have a tendency toward corrosion at the interface between the matrix and fibers, especially at high temperatures. The reaction products are generally brittle, and can be a site of premature crack initiation. Coatings applied to the fibers have been shown to reduce the problem of fiber/matrix reactivity in different MMCs, but the coatings generally increase the cost of the fiber [21].

A coefficient of thermal expansion (CTE) mismatch can also be a problem with MMCs. Cooling from consolidation temperatures can cause substantial residual stresses

in both the fiber and matrix, which also creates shear stresses in the interface. Since the constituents are bonded together, the fibers do not allow the matrix to contract freely, nor does the matrix allow the fibers to contract freely. For example, for the negative temperature change depicted in Figure 2.11, the unrestrained matrix would contract by a strain amount of  $\alpha_m \Delta T$ , whereas the unconstrained fiber would only contract by a strain amount of  $\alpha_f \Delta T$  (where  $\alpha$  denotes the coefficient of thermal expansion, the subscript  $m$  denotes matrix properties, the subscript  $f$  denotes fiber properties and  $\Delta T$  indicates a temperature change).

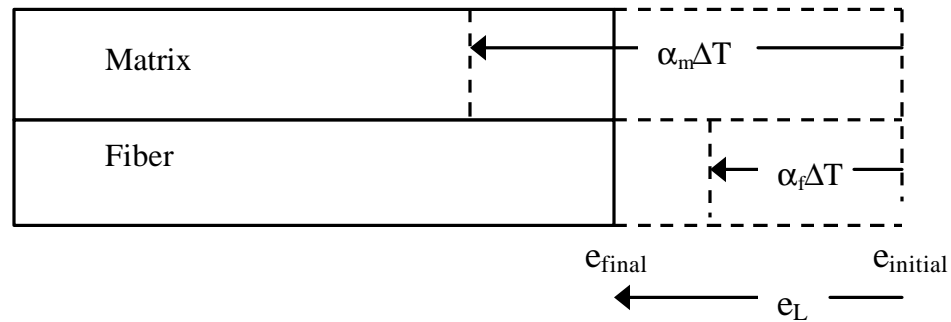


Figure 2.11: Coefficient of thermal expansion mismatch causing residual stresses

However, since they are bonded together, each constituent limits the other – they must strain to the same final amount, denoted  $e_{final}$ . Therefore, the fiber restricts the matrix to the final overall laminate strain of  $e_{final}$ , and the matrix forces the fiber to contract down to the final overall laminate strain of  $e_L$ . This induces a positive strain in the constrained matrix ( $\alpha_m \Delta T - e_L$ ) to reach the overall laminate strain, and a negative strain in the fiber ( $\alpha_f \Delta T - e_L$ ). The example depicted would result in tensile residual stresses in the matrix, and compressive residual stresses in the fiber. This demonstrates

what happens when the CTE of the matrix is higher than that of the fiber; upon cool-down from consolidation temperatures the matrix “wants” to contract more than the fiber. The residual stresses in both the matrix and the fibers are not negligible. If the residual stress is too great, a thermal mismatch can result in transverse cracking in the matrix from the induced residual tensile stress.

### ***2.3.1 Titanium Matrix Composites***

Titanium matrix composites (TMCs) are attractive enabling materials because they display high strength and stiffness-to-density ratios at moderate to high temperatures (400-800°C). The Integrated High Performance Turbine Engine Technology initiative (IHPTET), with a basic goal of doubling engine capability by the year 2003, was a major driver in the development of TMCs [23]. In the intended application of rotating components, such as impellers, disks, and bladed disks (blisks), TMCs offer a weight savings of 30-50% over conventional nickel superalloys. They have demonstrated feasibility and performance capability in components such as engine shafts and fan blades. Their first application in a production aircraft is the actuator piston rods in the engine of the U.S. Air Force’s F-22 fighter plane. TMCs were also extensively studied during the NASP program for use in the aircraft skin.

Several TMC systems have been extensively studied and characterized [23]. The titanium matrix materials of some of these TMCs include the following: Ti-15-3, Timetal®21S, Ti-6-4, Ti-24-11, and orthorhombic titanium alloys (such as Ti-22Al-23Nb). A comparison of the strengths for several of these titanium alloys and their respective composite systems is given in Figure 2.12. Oxidation and creep limit the usage temperature for most of these alloys. Environmental degradation embrittles the

surface layer, and can increase the fiber/matrix reaction zone, reducing fatigue life and strength. Jin, et al. [24] found that oxidation was a function of applied load as well as temperature, noting an increased oxide scale under applied load than similar specimens with no loading. Prior to weakening the fiber/matrix interface, the surface oxide layer that forms has, however, been found to initially increase ultimate tensile strength and yield strength, though ductility is sacrificed [25].

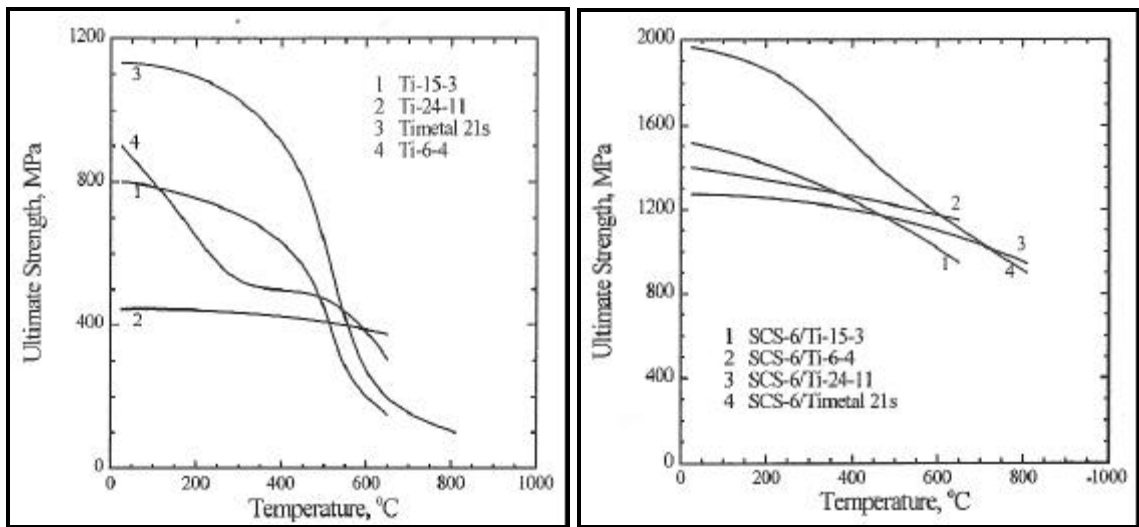


Figure 2.12: Ultimate strength for a) several titanium alloys and b) their composite systems [23]

The TMCs compared in Figure 2.12 are all reinforced with the continuous silicon carbide fiber, SCS-6, manufactured by Specialty Materials, Inc. (previously Textron, Inc.). Silicon carbide fibers have been the conventional choice for TMCs since their inception in the late 1970s, with a high strength (3600 MPa at room temperature) and low reactivity with the titanium matrix. The SCS-6 fiber is the industry standard. This fiber consists of silicon carbide deposited on a carbon monofilament core via chemical vapor deposition (CVD) processing. A thin coating of carbon minimizes the reaction zone

between the fiber and the titanium matrix – a problem with boron and alumina fibers. In recent years, Specialty Materials has developed a new higher strength silicon carbide fiber, designated the Ultra-SCS. Though similar to the SCS-6 in composition, these new fibers have a higher modulus and 50% higher tensile strength than the SCS-6 [26].

TMCs generally have a weak fiber-matrix interface. In a study of SCS-6/Ti-15-3 laminates, Johnson, et al. [27] reported a knee at stress levels as low as 140-200 MPa, well below the matrix yield strength of 690 MPa, though the knee typically signifies failure of the off-axis plies. However, in this case the modulus was lower upon unloading, indicating damage to the laminate. The off-axis laminate plies suffered fiber/matrix interface failures at stress levels as low as 138 MPa (20 ksi), significantly affecting the mechanical properties. Because of the weak interfaces, the systems suffer stiffness loss and fatigue damage in just a few cycles. The interface is not only weak because of chemical reactions, but also due to the residual stresses that arise from the thermal mismatch of the constituents [28].

Deformation and failure mechanisms during monotonic loading differ among plies in TMCs. In tension, 0° plies exhibit high plasticity, whereas 90° plies suffer from microcracking and debonding damage. This is because strength in the 0° plies is controlled by the fibers, while it is controlled by the matrix and the weak interface in 90° plies. Also, the compressive strength is generally higher than the tensile strength for TMCs, due to the residual thermal stresses from fabrication [29].

Fatigue failure mechanisms in 0° laminates include fiber-dominated damage, crack initiation at damaged fibers, and preferential matrix cracking with fiber bridging. Fiber-matrix debonding and crack initiations at fiber-matrix interfaces are common in 90°

laminates. The weak fiber-matrix interfaces in TMCs cause 90° plies to have a much shorter fatigue life than that of 0° [30]. Crack growth rates are improved in TMCs over the unreinforced matrix due to crack tip shielding and fiber bridging effects. Therefore, although TMC fatigue cracks often initiate early, crack propagation life can be very long [31]. Ironically, weak interfaces limit life by promoting crack initiation and growth in 90° plies, and they extend life in 0° plies by with fiber bridging. Testing in isothermal fatigue and in-phase thermomechanical fatigue (TMF) result in fiber-dominated damage, while out-of-phase TMF is dominated by matrix damage [31-35]. Several studies have shown that the stress in the 0° fiber can be used to correlate fatigue life of different laminates containing 0° plies [27, 32, 33].

### **2.3.2 Modeling MMC Behavior**

Several micromechanical models have been developed in order to analytically predict the thermal and mechanical behavior of fibrous composites. Models used for predicting fatigue life vary from complex finite element methods [28, 36, 37], to life-fraction models [38], to mechanistic approaches [39, 40]. Strength of material models such as the multiaxial model in METCAN [41] and the vanishing fiber diameter (VFD) model in AGLPLY [42] have been used to obtain average stresses in the constituents. Many of these models can be modified to account for rate-dependent effects of the constituent phases. This is important because inelastic deformation of metal matrix materials at elevated temperatures is dominated by viscoplasticity [43]. In general, there is a trade-off between the accuracy of the solution and the efficiency of obtaining the solution.

AGLPLY is a program that uses the VFD model to predict the elastic-plastic response of metal matrix composites. It has been used previously to accurately predict  $0^\circ$  stress-strain behavior as well as overall laminate response [22, 27, 44]. Another iteration of the program that also accounts for time-dependent behavior in the matrix is VISCOPLY. VISCOPLY has been used to model the fatigue behavior of Ti-15-3 and Timetal®21S subjected to a hypersonic flight profile, with predictions falling within 10% of the experimental results [44, 45].

Modeling the transverse behavior ( $90^\circ$  plies) of MMCs is challenging due to the complex geometry, nonlinear material behavior, and presence of damage. More complex analyses, such as the FEA model proposed by Foulk et al. [36], attempt to account for environmental degradation as well as damage from material inelasticity, fiber/matrix debonding, and fiber bridging. Again, FEA models are computationally expensive and complex. It is known that matrix cracking generally reduces the fatigue response of TMCs. This aspect can be captured in less complex models such as AGLPLY by simply reducing the effective modulus of the matrix in the program. The degree of reduction varies with test type and amount of matrix cracking, and must be determined experimentally. Other complex damage mechanisms, such as the weak fiber/matrix interface, which is detrimental to the mechanical properties of  $90^\circ$  plies, call for more modifications to AGLPLY. Johnson et al. [27] found that reducing the transverse modulus of the fibers in the  $90^\circ$  by 90% correctly modeled the debonding effects.

#### *2.3.2.1 AGLPLY*

AGLPLY is a two dimensional laminate code that runs from a DOS prompt. The AGLPLY program predicts MMC properties using the VFD model, which was first

proposed by Dvorak and Bahei-El-Din [42]. It was designed to predict, in an average sense, lamina and laminate properties and stress-strain behavior. This model assumes the fibers have a very small (vanishing) diameter, yet they still occupy a finite volume fraction of the composite. In the model, the fibers do not interfere with matrix deformation in the transverse or thickness directions, and only contribute to the stress state in the longitudinal (fiber) direction. The only constraint is in the longitudinal direction – the matrix and fiber must deform equally, which simplifies the governing equations so that complex numerical analysis is not required.

The geometry of the AGLPLY composite model is shown in Figure 2.13. It consists of a symmetric laminate of continuously reinforced fibrous composite layers. Each ply can consist of different fiber and matrix combinations and orientations, specified in the  $i^{\text{th}}$  ply by the angle  $F_i$ .

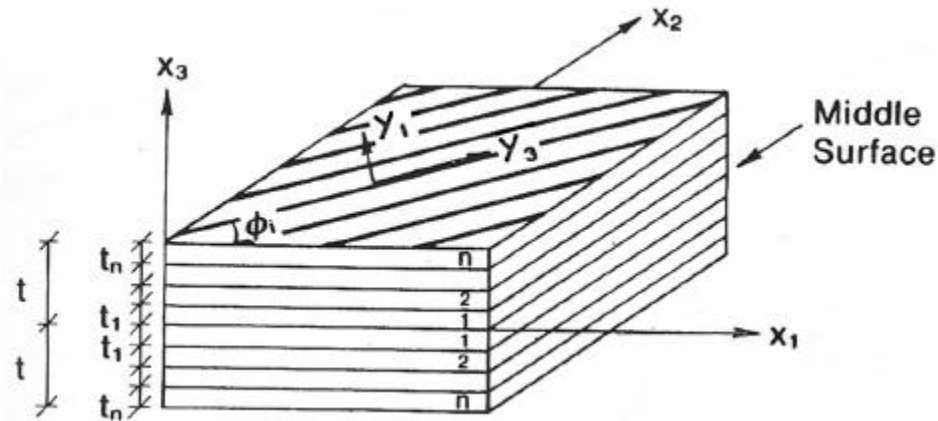


Figure 2.13: AGLPLY ply coordinate system [46]

The model consists of an elastic-plastic matrix unidirectionally reinforced by continuous elastic fibers in each ply. Both constituents are assumed to be homogeneous



and isotropic, and it is further assumed that perfect bonding exists between them. The inputs to the model can be either lamina properties or fiber and matrix properties. The material properties, including Young's modulus, CTE, Poisson's ratio, yield stress, and stress-plastic strain curves, are input as a function of user-selected temperatures. Intermediate material properties are found by linear interpolation between the given data points. The program only models elastic behavior if lamina properties are specified. When fiber/matrix properties are specified, the program assumes that the fiber is always elastic. The matrix, however, may have elastic-plastic properties. The matrix yield is determined by the Von Mises yield criteria.

Any combination of inplane loads and temperature paths can be specified. The program has restart capabilities, allowing for input of piece-wise linear load-time functions in sequential steps. This allows for simulation of fabrication and subsequent loading in sequential job steps. The output consists of the overall elastic laminate properties and the average stresses and strains for both the fiber and matrix in each ply. Instantaneous laminate moduli and CTE are also reported for each load or temperature step [47].

## **2.4 Gamma Titanium Aluminides**

Gamma titanium aluminide alloys have been studied extensively in recent years. They are promising candidates as advanced structural materials for high temperature applications because of their attractive combination of low density (about  $3.8 \text{ g/cm}^3$ ), high melting temperature, good oxidation and burn resistance, high modulus and strength retention at elevated temperatures, and good creep properties [3-5, 48]. The most cited limitations for widespread application of these materials are poor room temperature

ductility, low fracture toughness, fast fatigue crack growth rates, and concern about oxidation resistance above 800°C [3-6, 48, 49]. Generally, mechanical properties are linked to chemistry and microstructure, and they exhibit a trade-off between fracture toughness and ductility [3].

Gamma titanium aluminides have also recently received interest as potential matrix material in TMCs [50-55]. However, due to their low room temperature ductility and the high thermal mismatch between the alloy and silicon carbide fibers, initial attempts at fabrication of  $\gamma$ -TiAl matrix composites resulted in extensive matrix cracking during consolidation [55].

#### ***2.4.1 History of Gamma Titanium Aluminide Development***

The earliest major work on gamma alloy development was initiated by the U.S. Air Force Materials Laboratory. This research, conducted by Pratt and Whitney from 1975-1983, recommended Ti-48Al-1V-(0.1C) as the best alloy composition based on ductility and creep resistance. The second major development program, again initiated by the Air Force and performed by General Electric from 1986-1991 identified a second generation of alloys, Ti-48Al<sub>2</sub>(Cr or Mn)-2Nb with improved ductility, strength, and oxidation resistance [56]. In 1993, GE conducted successful engine tests on a full-set wheel of gamma blades, which improved overall confidence in the material [48, 56].

The initial processing route for fabrication of gamma components was investment casting. However, this processing route can lead to fluctuations in the Al content of more than  $\pm 2$  at.-%, leading to a non-uniform microstructure, and a significant variation in the mechanical properties [5]. Powder metallurgy (P/M) technologies, on the other hand, provide more precise control of composition and microstructure, as well as helping

reduce fabrication costs [57, 58]. More recently, developments in P/M methods and alloying combinations have led to the production of prematerial that can be used for sheet rolling [5, 59, 60]. Plansee AG developed an Advanced Sheet Rolling Process (ASRP), which allows processing on a conventional hot-rolling mill at low rolling speeds, producing thin sheet material with homogenous alloy composition [59]. Using this patented process, Plansee produces sheets of 1mm thickness which are commercially available. In addition, small foils with a thickness down to  $\sim 150\ \mu\text{m}$  have been rolled [59].

The next processing step after producing uniform  $\gamma$ -TiAl sheets is generating useful parts for aerospace and turbine applications. Superplastic forming (SPF) is a technology that enables fabrication of the sheet material into useful geometries [61]. Superplastic forming trials have been performed on a laboratory scale to show the formability of the sheet materials, producing true strains as high as 600% [59]. Other tests in industrial SPF facilities have demonstrated the feasibility of shaping complex geometries. Joining methods for these materials, such as brazing, liquid interface diffusion bonding, and laser welding methods have also been developed. These advances, many developed by BF Goodrich Aerospace Aerostructures Group, led to the successful manufacture of structures such as the truss core previously seen in Figure 2.7 [62, 63].

#### **2.4.2 General Properties**

The composition of engineering  $\gamma$ -TiAl based alloys generally consists of 45-51 at.% Al with 1-10 at.% ternary additions (see Figure 2.14). They consist predominantly of the  $\gamma$ -TiAl phase with a small amount of  $\alpha_2$ -Ti<sub>3</sub>Al phase. The  $\gamma$ -TiAl phase has the L1<sub>0</sub>

ordered face-centered tetragonal structure, and the  $\alpha_2$ -Ti<sub>3</sub>Al has the hexagonal DO<sub>19</sub> structure. The ternary additions serve to improve properties such as: increasing the room temperature ductility, improving high temperature properties, or refining the grain size [4, 5, 48]. For example, additions of V, Mn, Mo and Cr have been shown to increase the room temperature ductility. Oxidation resistance is improved with Ni, Ta, and Si. Creep resistance is improved with C, Si, N, Ta, and W. Fatigue strength is improved with the addition of Nb. And finally, small additions of B and/or W can be used to refine the grain size.

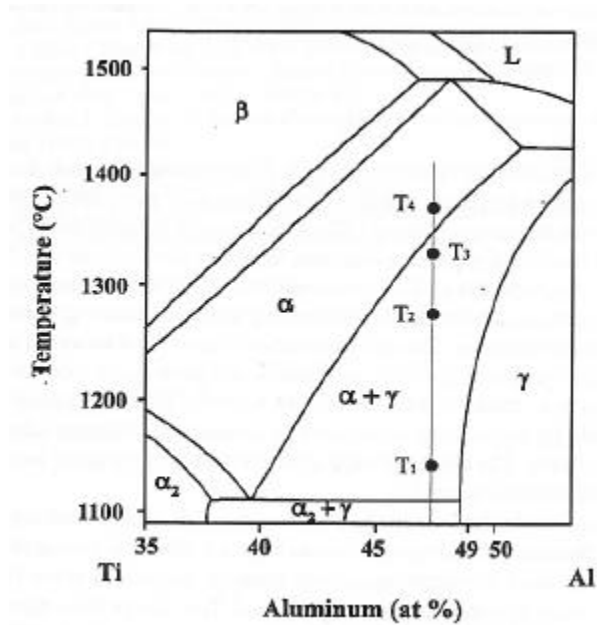


Figure 2.14: Central part of the equilibrium Ti-Al phase diagram [64]

Generally, four distinct microstructures can be developed in TiAl alloys, depending on the thermo-mechanical treatment. The four distinct microstructures have been identified as: near-gamma (NG), duplex (DP), nearly lamellar (NL), and fully lamellar (FL) [3, 48, 58, 64]. Heat treatments in the  $\alpha + \gamma$  two-phase field at temperatures

$T_1$ ,  $T_2$ , and  $T_3$  in Figure 2.14 normally result in NG, DP and NL respectively. When the alloy is heat treated in the  $\alpha$  phase field ( $T_4$  in Figure 2.14), the FL microstructure results. The first two are fine- $\gamma$ -grain based (with grain sizes  $< 70\mu\text{m}$ ), and the latter are lamellar based, with larger grains ( $100\text{-}500\mu\text{m}$ ). Generally, a NG structure contains equiaxed  $\gamma$  grains and small  $\alpha_2$  particles. A DP structure is composed of fine  $\gamma$  grains and lamellar colonies with alternate  $\gamma$  and  $\alpha_2$  plates. The NL structure consists of coarse lamellar colonies with a small amount of fine  $\gamma$  grains, while the FL structure consists of only lamellar colonies. Mechanical properties in  $\gamma$ -TiAl alloys are reliant not only on alloy composition, but also strongly depend on microstructure and grain size.

As can be seen in Figure 2.15, the room temperature (RT) tensile ductility of  $\gamma$ -TiAl alloys only ranges from 0.3% to 4.0% elongation, and the RT tensile strength is typically in the 400-600 MPa range. These alloys demonstrate good strength retention up to about 800°C, and generally have a brittle-ductile transition temperature (BDTT) ranging between 600-820°C. Ductility increases and strength decreases rapidly at temperatures above the BDTT [64]. The near-gamma and duplex structures are associated with relatively low yield and tensile strength values, and moderately high ductility. On the other hand, fully lamellar structures have high tensile strength values both at RT and elevated temperatures, though ductility values of specimens with lamellar structures is much lower [3, 60].

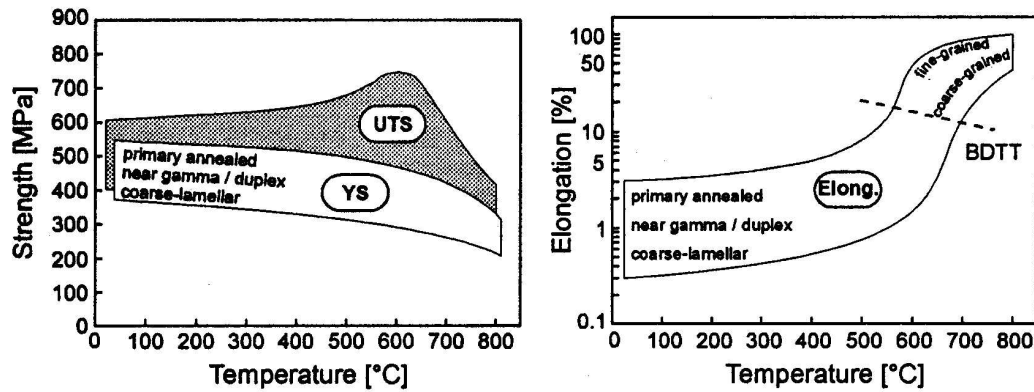


Figure 2.15: Mechanical property trends of gamma TiAl based alloys with test temperature and microstructure [61]

Fracture toughness values are dependent on microstructure, with values ranging from 10-35 MPavm [48, 65]. Alloys with lamellar microstructures have higher fracture toughness than those with equiaxed grains, demonstrating the tradeoff between ductility and fracture toughness. The fracture toughness of these alloys improves with temperature up to a transition temperature (often around 800°C), and decreases thereafter [64, 66]. Fracture mechanisms are also microstructure-dependent: intergranular fracture and cleavage are dominant in duplex microstructures, while translamellar fracture, interfacial delamination, and decohesion of lamellar colonies are more important in lamellar alloys [3, 67]. Fracture mechanisms also change with temperature: transgranular cleavage at room temperature, intergranular fracture at intermediate temperatures above the BDTT (600-800°C), and dimple fracture at higher temperatures [49, 64, 66].

Fatigue crack growth (FCG) rates are higher for these alloys than for superalloys, though fracture toughness is comparable [64]. Smaller grain sizes improve fatigue crack resistance [64, 68]. The fatigue damage process is controlled by the linkage of multiple microcracks (which can be propagating or nonpropagating); the linkage then forms a

macroscopic crack. A significant difference between microstructures is that in the lamellar structure, cracks initiate early, but propagate slowly because of crack wake ligaments. Duplex microstructures, on the other hand, spend the majority of their fatigue lives nucleating microcracks which propagate rapidly [65]. For high cycle fatigue (HCF), duplex microstructures show better fatigue properties at lower temperatures, but fully lamellar structures exhibit longer lives at higher temperatures [48].

Creep resistance, too, is microstructure dependent; it is higher for fully lamellar than for duplex microstructures and appears to increase with grain size [48, 56]. Stress exponents vary widely, depending on microstructure, test temperature, and applied stress level, with activation energies ranging from 280-410 kJ/mole [48]. In general, higher creep resistance is related to lower RT tensile ductility.

It appears that the maximum application temperature for aluminides is determined by oxidation resistance rather than creep or strength retention [64]. In general, the oxidation resistance is higher than that of Ti-alloys, but is still much lower than NiAl-based alloys [5]. Oxidation resistance in alloys is based on the addition of an element which will oxidize selectively and produce a protective surface oxide (such as  $\text{Al}_2\text{O}_3$ ). Initial mass gain behavior of  $\gamma$ -TiAl alloys is characterized by a single-stage parabolic curve, followed by linear behavior and extensive breakaway oxidation (spalling) after an elapse time duration. The time duration varies with increasing temperature. During oxidation, a brittle surface layer forms – which can act as an initiation site for cracks upon loading [5]. The layer formed has two distinct layers: a porous surface layer of pure oxide titania ( $\text{TiO}_2$ ) and a sublayer of intermixed titania and alumina ( $\text{Al}_2\text{O}_3$ ) between the surface and the interface. The titania forms on the surface and grows until the alumina

can form a continuous layer and stop the growth of the transient oxide [69, 70]. Alumina scales, because they have an extremely slow growth rate, are protective at temperatures in excess of 1200°C. However, intermixed alumina/titania scales are generally protective only to about 750-800°C because titania has a much higher growth rate [71].

### ***2.4.3 Properties After High Temperature Exposure***

As all of the potential applications of gamma alloys include high temperature exposure, it is critical to examine what influence this exposure can have on the mechanical properties of the materials. A number of investigators have examined the influence of elevated temperature exposure on a variety of gamma alloys. As noted earlier, the low room temperature ductility of gamma alloys is already a concern. However, after high temperature exposure, tensile ductility is generally reduced even lower.

Dowling and Donlon [72] found the ductility reduced to half the original following exposures of 50 hours at 775°C, which was accompanied by the formation of a thin surface layer. Pather, et al. [73] found that exposure at temperatures higher than 500-600°C significantly reduced the room temperature strength and ductility. They also noted this effect after very short times; for example they reported a 50% decrease in ductility after a 2 hour exposure at 700°C. They attributed this to surface residual stress and surface compositional changes as well as oxygen and hydrogen embrittlement. Kelly, et al. [74] further found that a minimal exposure at 315°C for 10 hours reduced ductility, and that the post exposure ductility loss only occurs at temperatures below 200°C. Lee, et al. [75] investigated and generalized the findings to other alloys and



microstructural conditions, indicating that all gamma alloys produce a detrimental brittle surface layer after elevated temperature exposure.

Plank and Rosenberger [76] studied the effects of high temperature exposure on both the monotonic response of an alloy as well as on its fatigue properties. They, similar to the aforementioned studies, showed a loss of tensile ductility and strength at room temperature of preexposed specimens, though no decrease in ductility was noted at higher temperatures (540° and 760°C). They also noted that exposed specimens displayed a loss of fatigue strength that was most severe at 540°C, though less severe at 760°C, while at room temperature the decrease was less apparent.

## **2.5 Gamma MET**

The gamma titanium aluminide alloy examined in this research is the  $\gamma$ -MET alloy produced by Plansee in Austria. The nominal composition of the alloy is Ti-46.5Al-4(Cr,Nb,Ta,B)at.%, however the specific alloy content is proprietary to Plansee. The chromium is added to improve ductility, and the niobium and tantalum are added to improve oxidation and creep resistance. Trace amounts of boron are added to refine the grain sizes during heat treatments, as boron hinders grain growth during heat treatments in the alpha field [64].

This material is typically manufactured from powder metallurgy  $\gamma$ -TiAl preforms. Final consolidation is achieved by hot-isostatic pressing (HIPing) at nominal conditions of 1000°C, 124 MPa (18 ksi) pressure, over a period of two hours [59]. The prematerial is then subsequently rolled on a conventional hot-rolling mill using Plansee's patented Advanced Sheet Rolling Process (ASRP) [77]. Afterwards, a heat treatment at 1000°C for 2 hours under vacuum gives a primary annealed (PA) microstructure. It is a fine

grained, globular microstructure consisting mainly of  $\gamma$  grains with some small amounts of  $\alpha_2$  and other phases (such as  $\beta$  phase and borides) distributed at grain boundaries and triple points. Heating above the alpha-transus temperature ( $\sim 1320^\circ\text{C}$ ) gives a designed fully lamellar (DFL) microstructure. PA exhibits superior fatigue properties, while DFL shows better creep properties [62].

### 2.5.1 Mechanical Properties

There is a limited amount of mechanical property data in the literature for this specific alloy. Table 2.1 gives a summary of the data found in the literature, to the best of the author's knowledge, as well as the data generated by previous graduate student Jason Craft. A degree of scatter appears in the room temperature data, even among publications that share authors.

Table 2.1: Tensile properties of Ti-46.5Al-4(Cr,Nb,Ta,B)at.%

T ( $^\circ\text{C}$ )	Specimen	E (GPa)	UTS (MPa)	0.2% YS (MPa)	$e_{\text{tot}}$ (%)	$e_p$ (%)
RT	Sheet material (PA) <sup>1</sup>	158	450	436	0.85	--
	Sheet material (PA) <sup>2</sup>	158	526	469	1.5	--
	Sheet material (PA) <sup>3</sup>	138.6	498	481	0.8	0.26
	Sheet material (PA) <sup>4</sup>	155	588	545	1.4	--
	Consolidated plies <sup>5</sup>	162	505	496	0.55	0.24
	Consolidated plies <sup>3</sup>	152	542	542*	0.35	0
450	Consolidated plies <sup>3</sup>	150	532	532*	0.35	0
650	Sheet material (PA) <sup>3</sup>	113	496	312	2.8	2.62
700	Sheet material (PA) <sup>2</sup>	113	505	384	5.1	--
800	Sheet material (PA) <sup>1</sup>	70	245	240	37.5	--

\* Fractured before yielding

<sup>1</sup> Leholm, et al. in *Gamma Titanium Aluminides 1999* [62]

<sup>2</sup> Leholm, et al. in *Titanium '99: Science and Technology* [78]

<sup>3</sup> Craft, J.S., MS Thesis, Woodruff School of Mechanical Engineering [79]

<sup>4</sup> Clemens, et al. in *Gamma Titanium Aluminides 1999* [59]

<sup>5</sup> Hales, et al. in *Gamma Titanium Aluminides 2003* [80]

Figure 2.16 shows the trends for various tensile properties of this material over the full usage temperature range, as reported by Clemens, et al. [59]. As can be seen, the BDTT for this material occurs at approximately 750°C. Above this temperature, the ductility rapidly increases due to mechanical twinning and increased dislocation movements, and results in a drop of overall strength.

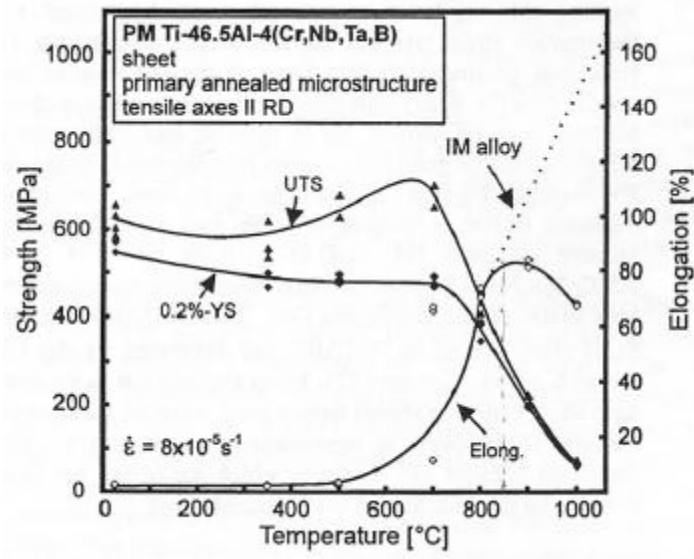


Figure 2.16: Trends in strength and elongation of Ti-46.5Al-4(Cr,Nb,Ta,B)at.% as function of temperature [81]

Chatterjee, et al. [77] studied both fatigue (see Figure 2.17 for S-N curves) and creep behavior (see Figure 2.17) of the sheet material. The PA microstructure demonstrates higher fatigue properties than the DFL microstructure, though the properties decrease with an increase in temperature to 700°C. Creep rates at 700°C are very low, though the values increase by an order of magnitude when increasing temperature to 800°C.

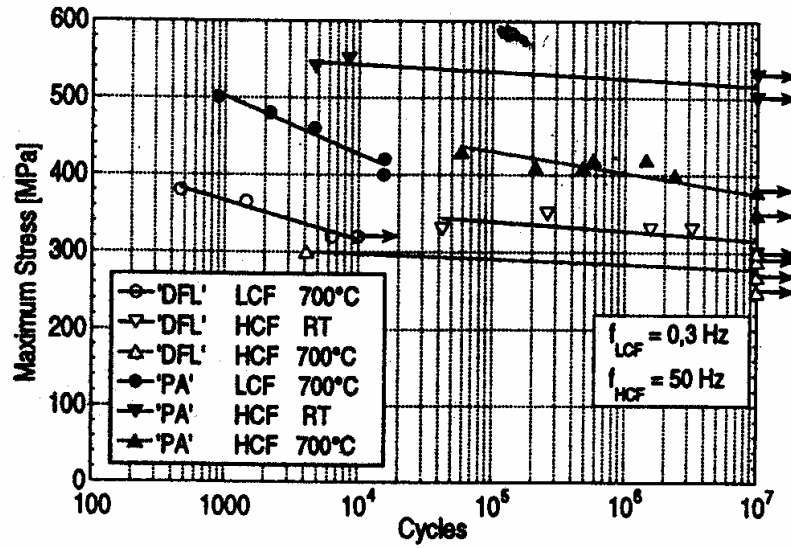


Figure 2.17: S-N curves at RT and 700C of Ti-46.5Al-4(Cr,Nb,Ta,B)at.% with two different heat treatments [77]

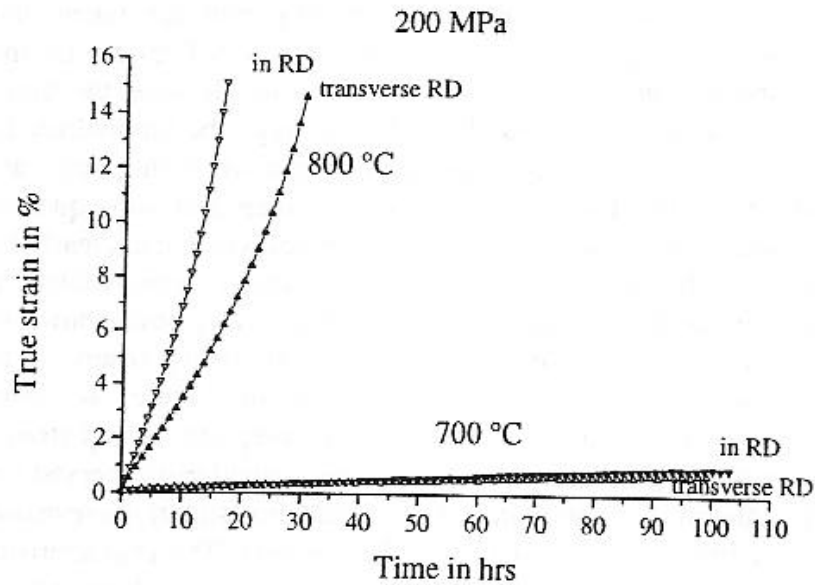


Figure 2.18: Creep curves for Ti-46.5Al-4(Cr,Nb,Ta,B)at.% at 700°C and 800°C and a stress of 200 MPa [77]

Pippan, et al. [82] studied fatigue crack growth and stress intensity range thresholds. The threshold of stress intensity range shows an R-curve behavior, as can be seen in Figure 2.19, where the designation FG denotes the PA microstructure, LT denotes a loading direction parallel to the rolling direction, and TL denotes a loading direction perpendicular to the loading direction. The first propagation of the crack is observed at about 1.7 MPavm, and  $\Delta K_{th}$  is about 4.5 MPavm for the PA microstructure. The  $da/dN$  vs.  $\Delta K$  curves can be seen in Figure 2.20 – this curve is significantly influenced by the stress ratio.

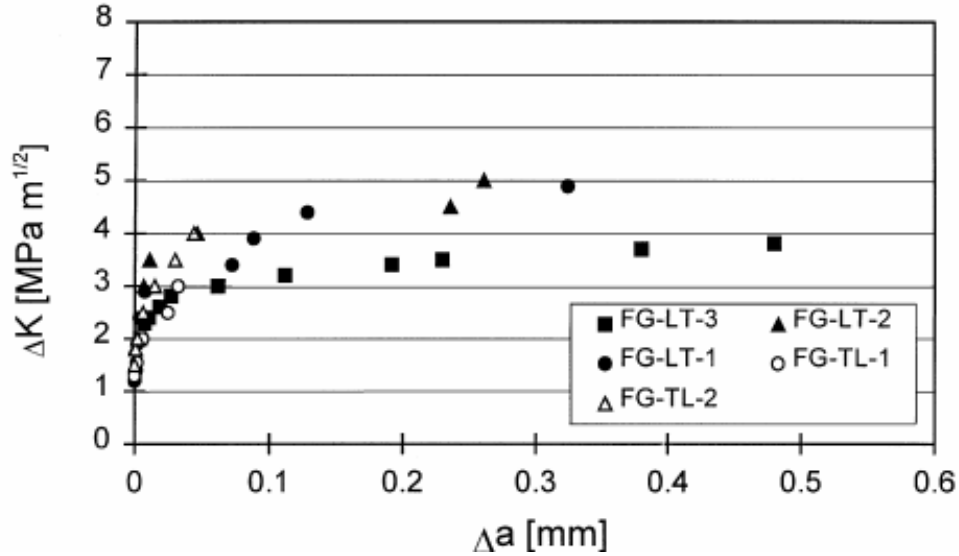


Figure 2.19: Stress intensity range vs. crack extension for PA microstructure of  $\gamma$ -MET [82]

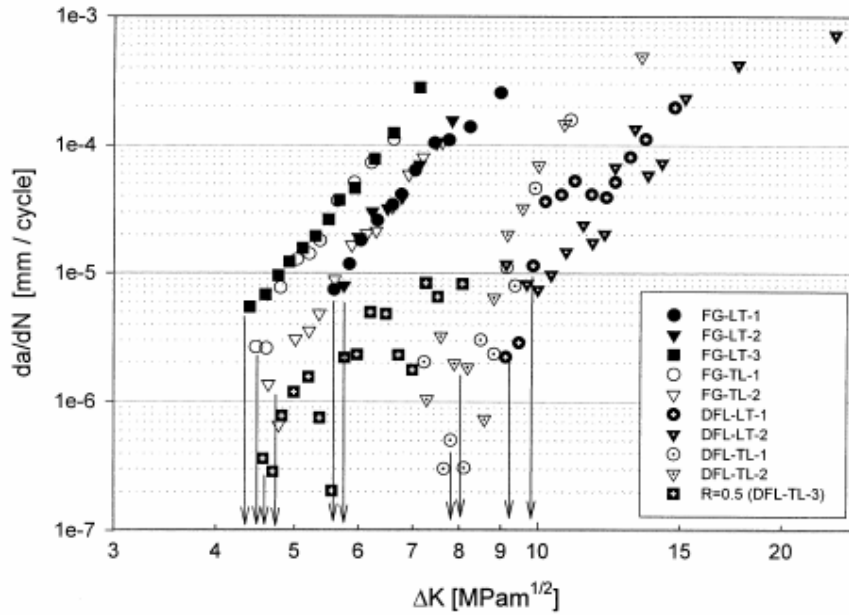


Figure 2.20:  $da/dN$  vs.  $\Delta K$  curves for both PA (denoted FG) and DFL microstructures of  $\gamma$ -MET [82]

### 2.5.2 Oxidation Behavior

The oxidation behavior of this alloy was previously examined by graduate student Jason Craft [79]. This oxidation study noted a parabolic mass gain with oxide composition comparable to other gamma titanium aluminides. The mass gain data measured over the temperature range 700-1000°C as a function of time is presented in Figure 2.21. At 700°C, negligible weight gain was observed over the duration of the test. This leads to the speculation that oxidation effects would be negligible at and below 700°C, and suggests a safe operable temperature for repeated usage.

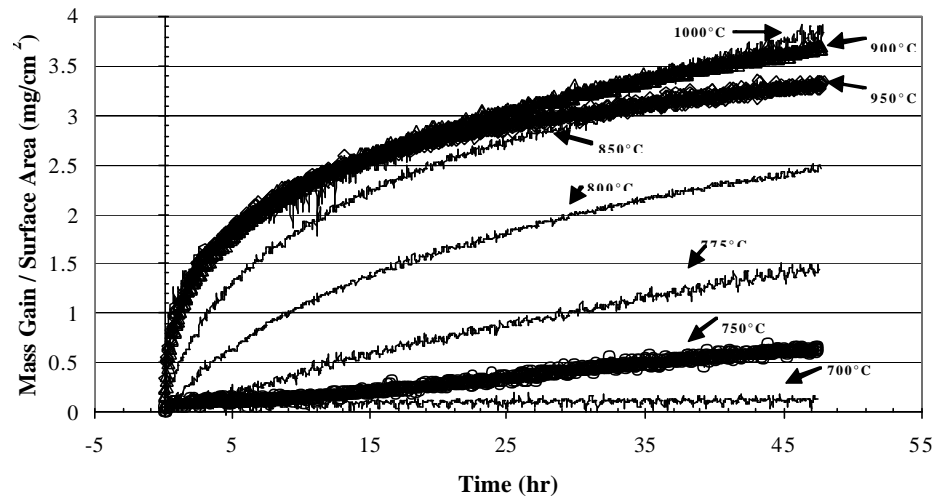


Figure 2.21: Isothermal mass gain per unit area of samples oxidized for 48 hours at various temperatures [79]

SEM inspection of cross-section views of the oxidized surfaces showed the typical multi-layered oxide scale previously documented for gamma titanium aluminide alloys at 800°C and higher. A thin layer of alumina and titania were observed at 750°C and 775°C. However, only a few isolated islands of oxide were observed on samples exposed at 700°C. Electron dispersive x-ray (EDX) was also used to characterize the chemical composition for the various oxides and the base alloy as a function of distance through the cross section (see Figure 2.22). The outer layer was determined to be  $\text{TiO}_2$ , the layer beneath it being  $\text{Al}_2\text{O}_3$ , and the mixed oxide layer adjacent to the alloy/scale interface consisted of a fine mixture of  $\text{TiO}_2$  and  $\text{Al}_2\text{O}_3$ .

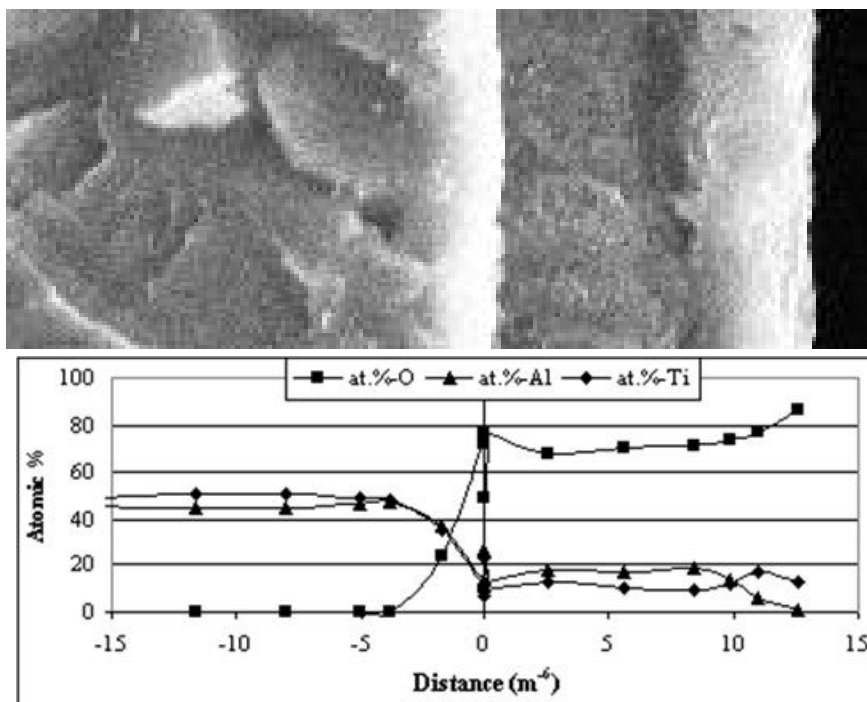


Figure 2.22: Oxide chemical composition vs. distance at 800°C [79]

Mechanical properties after oxidation are the subject of ongoing research in this area. Development of ultrathin protective coatings to improve high temperature oxidation resistance for this material are also underway at NASA LaRC [83].



## **CHAPTER 3**

### **MATERIAL**

The material studied in this program is a gamma titanium aluminide designated  $\gamma$ -MET. This chapter will present the rolled sheet material used for the mechanical testing as well as the foil matrix material (of the same composition) used during titanium matrix composite consolidation attempts at NASA LaRC. The latter sections will discuss the two different reinforcing fibers, the silicon carbide fiber and aluminum oxide fiber, that this research considered for use in gamma titanium aluminide matrix composites.

#### **3.1 Gamma-MET Rolled Sheet Material**

The gamma titanium aluminide sheet material used for the mechanical testing in this research is the  $\gamma$ -MET alloy produced by Plansee in Austria. This material is typically manufactured from powder metallurgy  $\gamma$ -TiAl preforms. Final consolidation is achieved by hot-isostatic pressing (HIPing) at nominal conditions of 1000°C, 124 MPa (18 ksi) pressure, over a period of two hours [59]. The prematerial is then subsequently rolled on a conventional hot-rolling mill using Plansee's patented Advanced Sheet Rolling Process (ASRP) [77]. Two 36 cm x 75 cm (14.2 in x 30 in) sheets of 1 mm thick rolled sheet material manufactured by Plansee were obtained from Goodrich Aerostructures. The nominal composition of the alloy is Ti-46.5Al-4(Cr,Nb,Ta,B)at.%, however the specific alloy content is proprietary to Plansee. The chromium is added to improve ductility, and the niobium and tantalum are added to improve oxidation and

creep resistance. Trace amounts of boron are added to refine the grain sizes during heat treatments – boron hinders grain growth during heat treatments in the alpha field [64].

After the rolling process, subsequent heat treatments are performed. Normally, a heat treatment at 1000°C for 2 hours is applied which gives a primary-annealed (PA) microstructure. The PA microstructure consists of fine-grained globular or equiaxed  $\gamma$  grains with small amounts of  $\alpha_2$  at the grain boundaries and triple points. The grain size is typically around 15-20  $\mu\text{m}$  [61]. The  $\gamma$ -MET sheet material used for this study was previously shown to have a PA type microstructure (see Figure 3.1) [79]. The average grain size appears to be about 20  $\mu\text{m}$ , and the micrograph compares well with previously published micrographs of the PA microstructure.

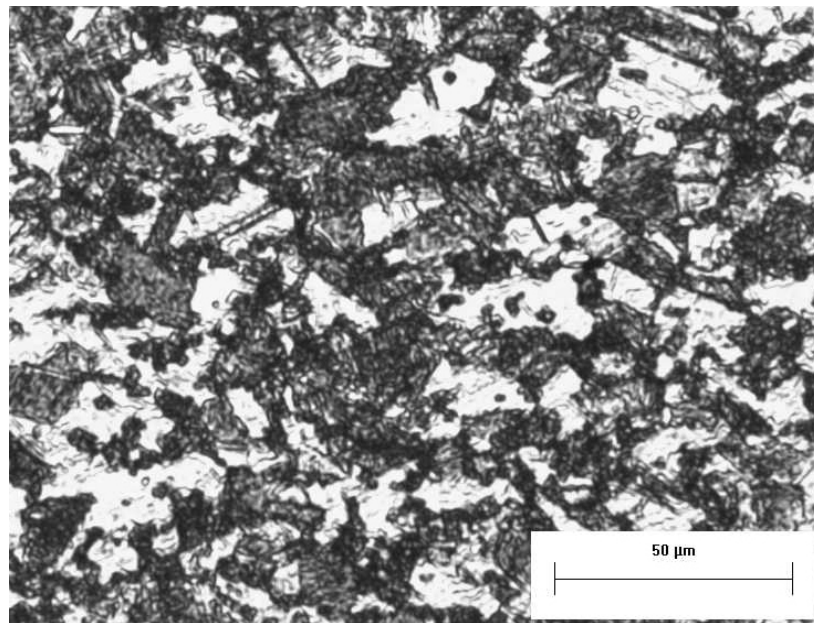


Figure 3.1: Micrograph of etched  $\gamma$ -MET sheet material [79]

The sheet was plasma cut into smaller, workable pieces by the Georgia Tech Research Institute (GTRI) Machine Shop, as attempts to shear the material resulted in brittle cracking. Coupons were cut from these smaller sections in the rolling direction and machined to final dimensions using electron discharge machining (EDM) facilities at the Mechanical Engineering Machine Shop at Georgia Tech. Thirty dogbone specimens were machined (see Figure 3.2) to use for tensile and fatigue testing. The coupons were 17 cm long, 2.54 cm wide at the grip area, 1.91 cm wide in the reduced section with a 3.175 cm radius of curvature, and 1 mm thick. Three additional samples with dimensions of 34.7 mm x 2.5 mm were also machined for use in the dilatometer for CTE testing.

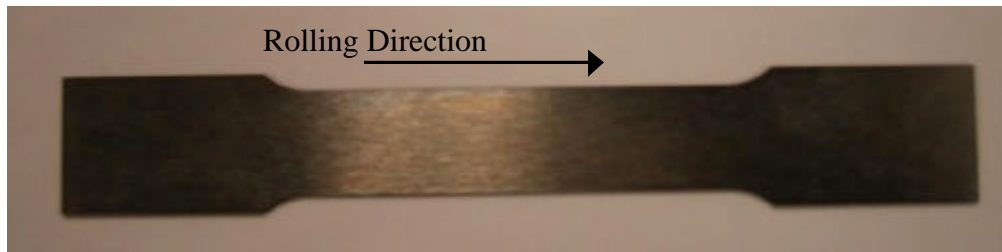


Figure 3.2: Dogbone coupon of the sheet material

Prior to mechanical testing, the edges and faces of the coupons were polished using 400-grit sandpaper to remove any surface flaws developed during consolidation, rolling, or final machining preparation. Of particular concern was eliminating the microcracks along the edges caused during the EDM machining process.

In addition to using the as-received sheet material, several coupons were exposed to elevated temperatures before testing. These coupons were first polished using 400-grit sandpaper to remove surface flaws on the edges and faces. They were then thoroughly cleaned before being placed in the furnace. Five coupons were heated to 800°C at a rate

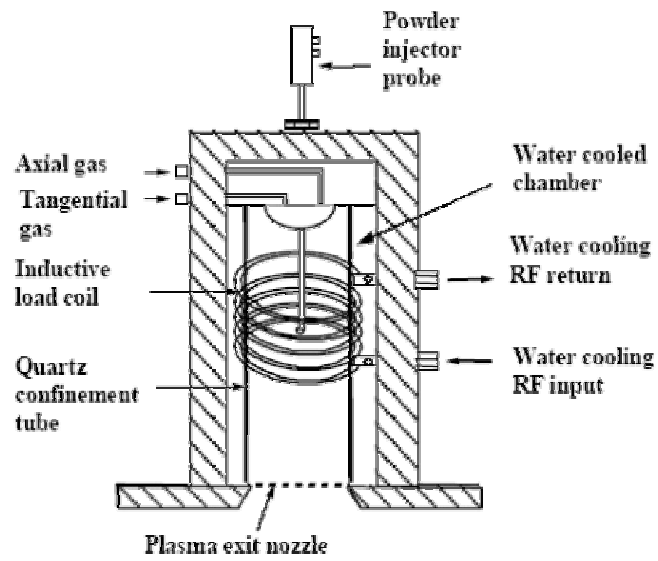
of 20°C/min and held for 5 hours at that temperature to allow the formation of a thin oxide film. Five other coupons were heated to 700°C at a rate of 20°C/min and held for 5 hours at that temperature. All specimens were cooled ambiently; they were removed from the furnace, place on a ceramic surface, and allowed to cool in room temperature air.

### **3.2 Foil Matrix Material**

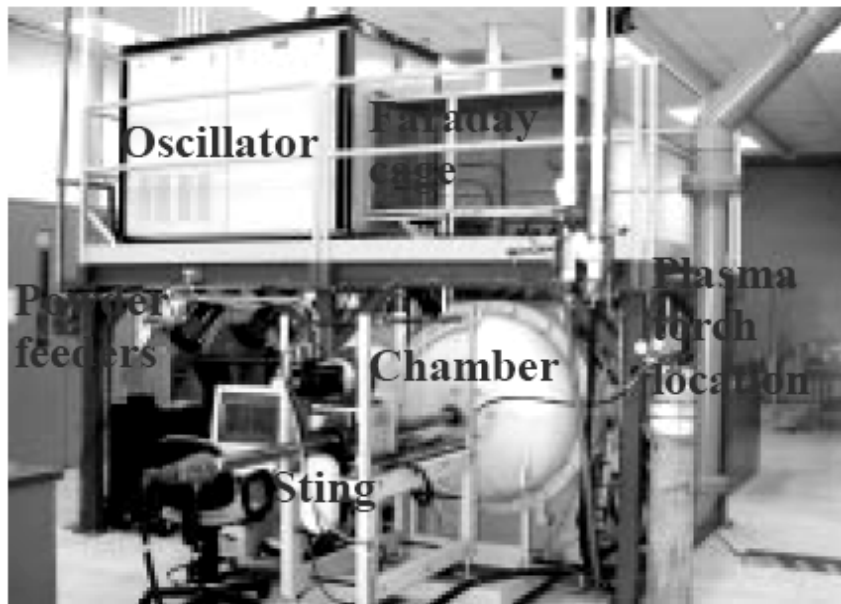
The thin sheets used in the attempt to manufacture titanium matrix composites, a process that will be described in the subsequent chapter, were produced at NASA LaRC. The processing route to produce the very thin sheets (~ .007 in or 0.178 mm thick) of the matrix material was RF plasma spray deposition of pre-alloyed powders. After manufacture, these thin sheets can be used for consolidation via vacuum hot pressing. The powder used to create these sheets has the same nominal composition, Ti-46.5Al-4(Cr,Nb,Ta,B) at.%, developed by Plansee AG and used for their rolled sheet material described previously.

Figure 3.3 shows the RF plasma spray facility at NASA LaRC, which includes a stationary plasma torch mounted on top of a cylindrical chamber. The powder is transported from feeders to the plasma torch by a carrier gas (helium) at a controlled rate and is injected via a water cooled injection probe located above the plasma. The powder then travels through the plasma, melts, and is accelerated through an exit nozzle toward a rotating, translating mandrel. The mandrel is a 30.5 cm diameter x 30.5 cm long water-cooled steel cylinder covered with a mild steel foil substrate. The melted droplets from the plasma solidify on the substrate, and the deposit thickness is controlled via the

deposition time. Upon removal from the mandrel, the deposit is sectioned into sheets of a size suitable for vacuum hot pressing.



(a)



(b)

Figure 3.3: RF plasma spray deposition facility at NASA LaRC: (a) schematic of plasma torch and (b) superstructure [80]

Figure 3.4 shows a hand lay-up of the thin sheets in preparation for consolidation via vacuum hot pressing. The parameters and process used to plasma spray the TiAl powder are described more in depth by Hales et al. [80]. It was interesting to note that the residual stresses induced from being deposited onto the round mandrel surface produces in a curvature in the thin sheets [84]. These stresses were relaxed by placing the sheets in the vacuum hot press (VHP) and heating them to about 1000°C while applying minimal pressure.



Figure 3.4: Thin sheets of foil produced by plasma spray deposition of pre-alloyed powers ready for VHP consolidation

Previously in this research program, graduate student Jason Craft mechanically tested two “fiber-less” panels of this consolidated material [79]. Those two panels consisted of 4 plies of the foil matrix material without any reinforcing fibers. However, the consolidation varied between the two panels. In one case, the plies were misaligned

and delamination was noted between the plies in some areas of the sheet. Rough regions where voids formed were present on the surface of both panels of the material. Flaws noted in the composite panels can be seen in Figure 3.5.

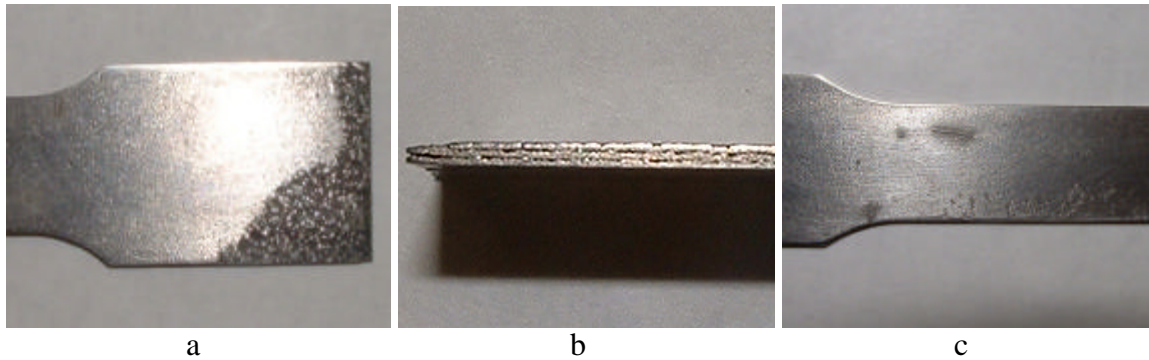


Figure 3.5: Flaws in the consolidated “fiberless” panels included: a) surface asperity, b) delaminated sections, and c) surface markings [79]

Monotonic tensile testing in both load control and strain control of the consolidated material led to brittle failure below the yield point, as can be seen in Figure 3.6. The total strain of the material in both cases was around 0.35%, which is much lower than the room temperature strain seen in the sheet material. NASA LaRC has reported some slightly higher strains-to-failure in their testing of consolidated panels [80], with an average of 0.55%. The low strain-to-failure of the consolidated material is attributed to surface roughness and residual macro- and micro-porosity in the material.



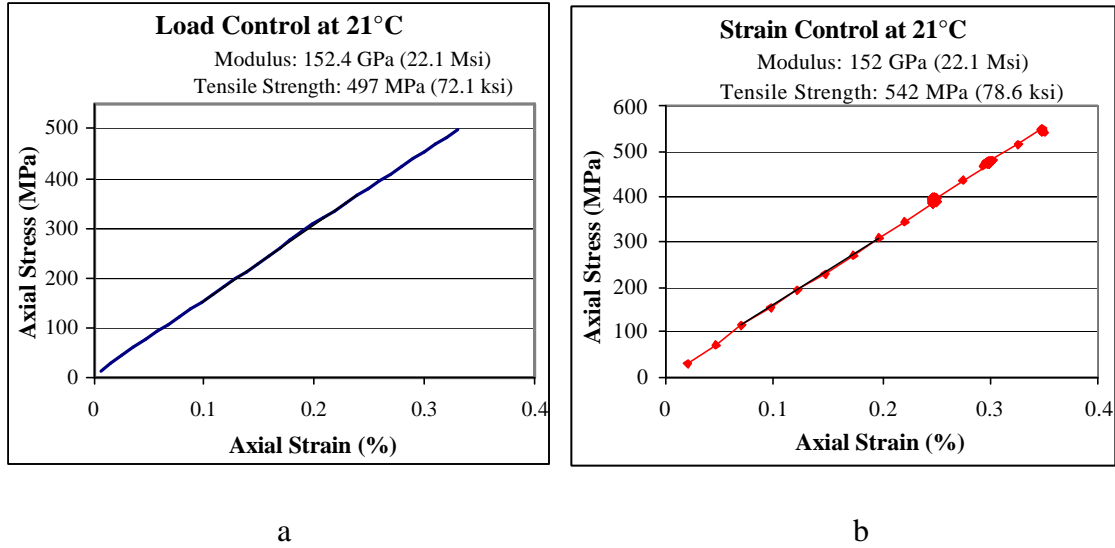


Figure 3.6: Monotonic results of consolidated material at 21°C: a) load control test b) strain control test [79]

### 3.3 SCS-6 and Ultra-SCS Silicon Carbide Fibers

The industry standard fibers used in TMC's for the past 15+ years are silicon carbide fibers, specifically the SCS-6 fiber manufactured by Specialty Materials, Inc. (previously Textron, Inc.) [26]. Silicon carbide fibers are desirable because of their high stiffness and high tensile strength. They also provide very high creep rupture and excellent high temperature performance [51, 52, 54, 55]. The Ultra-SCS fiber is also produced by Specialty Materials, Inc. and has improved mechanical properties: an elastic modulus of ~415 GPa (10% higher than the SCS-6 modulus of 380 GPa) and tensile strength of ~5865 MPa (50% higher than SCS-6 strength of 3450 MPa), the combination of which results in a higher strain to failure for the Ultra-SCS fiber. Both fibers consist of silicon carbide deposited on a carbon monofilament core via chemical vapor deposition (CVD) processing. Both fibers have a diameter of around 140  $\mu\text{m}$ , and also

have similar density and CTE properties. A cross-sectional diagram of the Ultra SCS fiber can be seen in Figure 3.7.

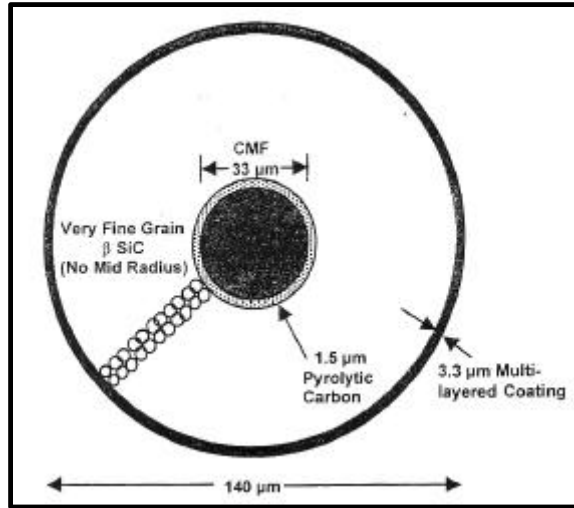


Figure 3.7: Cross-sectional diagrams of the Ultra-SCS fiber [26]

In order to evaluate the strongest option for titanium matrix composites, the analytical modeling used the Ultra-SCS fiber properties to determine the best potential composite properties. The actual composite manufacturing done at NASA LaRC employed the SCS-6 fibers.

### 3.4 Nextel 610 Alumina Fiber

Alumina fibers have received attention in recent years as potential reinforcements in gamma titanium aluminide composites [50-52, 54]. Although they have lower strength and stiffness characteristics, the CTE of alumina fibers is typically higher than that of silicon carbide fibers, which leads to a closer thermal match with gamma titanium aluminides. The Nextel 610 alumina fiber, manufactured by 3M, was selected as an alternative reinforcement for comparison purposes. The fiber is composed of  $\alpha$ - $\text{Al}_2\text{O}_3$

and has a smaller diameter of 10-12  $\mu\text{m}$ . The small diameter creates difficulties in manufacturing a TMC with these fibers, as a large number of fibers would be necessary to achieve even a small fiber volume fraction. The large number of fibers has the disadvantage of difficult/poor fiber distribution and a higher probability of fibers touching, which would have a detrimental effect on mechanical properties. A larger diameter alumina fiber, such as the sapphire  $\text{Al}_2\text{O}_3$  single crystal fiber produced by Saphikon Inc., with a diameter of  $\sim 125 \mu\text{m}$ , would be another possible alumina reinforcement, though the cost of this fiber hinders its manufacturability and it is not yet commercially available.

## CHAPTER 4

### ANALYTICAL AND EXPERIMENTAL METHODS

This chapter will discuss both the 2-D laminate code, AGLPLY, that was used for the analytical modeling portion of this research as well as the specifications and capabilities of the laboratory equipment used for the mechanical characterization of the material. The manufacturing procedure used to make sample TMC's at NASA is also described. The experimental methods used for each phase of the mechanical testing are discussed in detail, so that replication of the testing conditions would be possible.

#### 4.1 Experimental Equipment and Procedures

A variety of laboratory equipment was necessary to conduct mechanical characterization studies of the  $\gamma$ -MET rolled sheet material in this program. The following sections discuss the equipment used for both CTE and mechanical testing as well as the procedures implemented.

##### 4.1.1 Dilatometry

A dual pushrod dilatometer was used to find the CTE property data for the alloy (see Figure 4.1). It utilized a standard resistance furnace, alumina pushrods, and a sapphire reference. A flowing argon atmosphere was used to prevent excessive oxidation of the samples. Together with the furnace, the dual pushrod dilatometer used a linear variable differential transformer (LVDT) to measure specimen displacement. A thermocouple junction floating roughly 1mm directly above the sample monitored temperature. The equipment was located in laboratories managed by Dr. Robert Speyers

of the School of Materials Science and Engineering; graduate student Ben Church assisted in operation of the equipment.

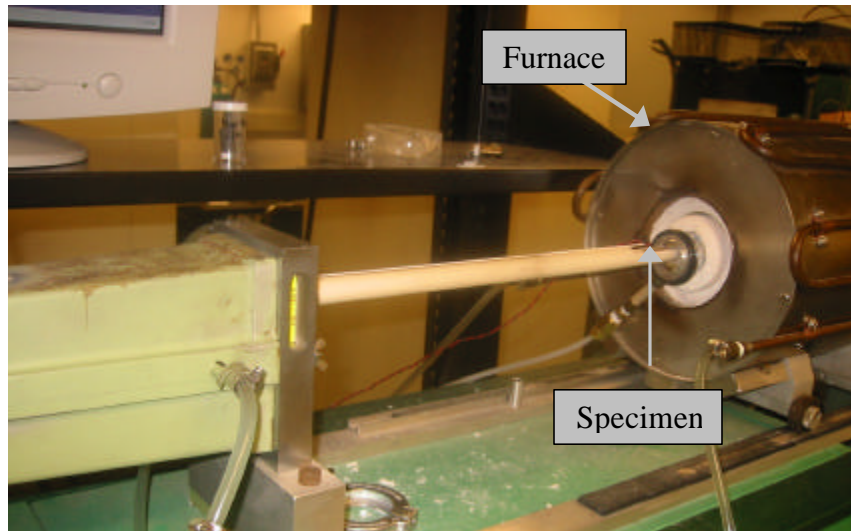


Figure 4.1: Dilatometry laboratory configuration with data acquisition

For the CTE testing, 3 samples of the MET rolled sheet material were cut to a dimension of 34.7 mm x 5 mm. One sample was in the longitudinal rolling direction, and the other two samples were transverse to the rolling direction. A sapphire reference material certified by the National Institute of Standards and Testing (NIST) was used to calibrate the dilatometer, as its CTE is well-known. The furnace was heated uniformly at a constant rate of  $2^{\circ}\text{C}/\text{min}$  from room temperature to a final temperature of about  $1250^{\circ}\text{C}$ . The LVDT measured the expansive displacement of the gamma sheet material relative to the expansion of the sapphire reference material.

The data acquisition recorded running time, furnace temperature, control temperature, and change in length of the sample relative to the sapphire reference

material. The percent change in length relative to the sapphire reference material was applied to the known expansion data of the sapphire to calculate the total expansion of the gamma titanium aluminide sample at each point. The coefficient of thermal expansion was calculated from the displacement versus temperature data. With the raw dilatometer data of  $\Delta l/l_o$  versus  $T$  (where  $l_o$  is the length at room temperature and  $T$  is temperature), the CTE,  $\alpha_T$ , was calculated by a linear regression over small temperature intervals using Equation 4.1:

$$a_T = \frac{n \sum x_i y_i - \sum x_i \sum y_i}{n \sum x_i^2 - (\sum x_i)^2} \quad (4.1)$$

where  $x_i$  represents a  $T$  datum point,  $y_i$  represents a  $\Delta l/l_o$  datum point, and  $n$  is the range over which each regression is performed. The value of  $n = 41$  was used in the calculations, which roughly equates to a 20°C temperature range. A more detailed discussion on the selection of this particular interval can be found in Ben Church's Ph.D. dissertation [85]. The value of  $a_T$ , calculated for each regression was assigned to the median temperature for each particular regression range. It should be noted that these values of  $a_T$  may vary from other calculated values of CTE, such as the mean  $a$  over a specified temperature range, as has been described by James, et al. [86].

#### **4.1.2 Microscopy**

An optical stereo microscope was used to look at the fracture surfaces and the composite panel cross sections. The microscope used was a Leica MZ6. It was equipped with software that enabled taking images at several depths, so that the focus plane

changed, and meshing those images together for a composite image with clear features at every depth.

#### ***4.1.3 Mechanical Testing Equipment***

The mechanical testing equipment consisted of an MTS 810 servo-hydraulic test frame and its peripheral equipment (see Figure 4.2). The test frame is rated at 10 metric tons of force and is equipped with a Teststar computer control with data acquisition, MTS model 647.10A hydraulic grips, and an Ameritherm SP-2.5 induction heater. The computer software is capable of conducting either monotonic or cyclic testing in either load control, displacement control, or strain control.

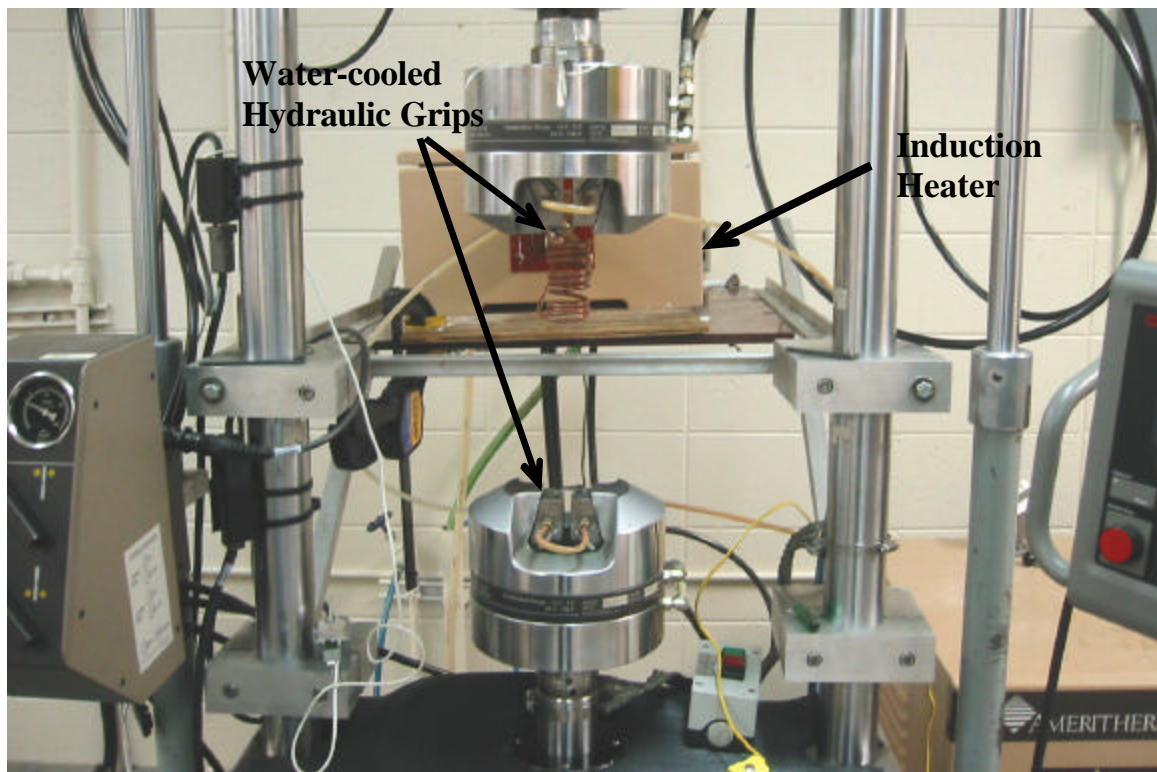


Figure 4.2: Servo-hydraulic Test Frame and peripheral equipment

An Epsilon high temperature extensometer (Model 3448) with ceramic rods was used for strain measurement. The extensometer secured to the test specimen with ceramic fiber cords attached to springs applied in tension. The extensometer measured strain over a gage length of 2.5 cm and was capable of measuring strains up to 0.1 mm/mm. It has the ability to travel  $\pm 10\%$ . For the room temperature tests, a  $0^\circ/90^\circ$  strain gauge rosette was used along with the extensometer. The strain gauges were bonded to the test specimens following the procedures outlined in ASTM E1237-93 [87]. The strain gauges were used to measure the Poisson effect in the material, as well as to validate the room temperature results and the experimental setup.

The gripping inserts used during testing had a diamond-toothed surface (S/N 647617-02). The inserts were water-cooled, so that the induction coil could be in close proximity to the grips. The hydraulic grips have manual pressure controls which allow the user to optimize the gripping pressure for a specific work piece size, geometry, and material.

The Ameritherm induction heater consisted of a main power unit and a remote heating station. The heater is rated at 2.5kW. The main power unit had an Omega Series CN-7100 series programmable temperature controller. The controller took manual input and self-tuned accordingly. The remote heating unit provided the heat source and was attached to the test frame directly behind the specimen. Water was supplied to the main power unit, which sent the flow to the remote heater, through coil, back to the remote heater, and finally to a drain. The water provided cooling to the copper tubing induction coil.



The induction coil itself was designed and manufactured in-house. The initial coil design was based on observations of existing coils that had been used successfully in the past for high temperature experiments. Rick Brown, the technician, gave advice and direction from his observations of past successful coils for the initial iterations. These initial iterations involved making coils with copper tubing of different diameters (1/8", 3/16", and 1/4") and with different numbers of turns. The final coil used can be seen in Figure 4.3, it was manufactured of 3/16" tubing. The concept for the coil design is for the coil to loop around the specimen in a spiral configuration. The coil turns are spaced at 2.5 cm to allow a gap for the extensometer tips to fit through and attach to the specimen.



Figure 4.3: Induction coil used in testing program, with susceptors heated and glowing

As the test specimens were only 1mm thick, it was difficult to design an induction coil that could be turned close enough to couple with the specimen causing it to heat up,

and yet still allow enough water through the tubing so that the coil itself does not overheat. Therefore two susceptors were used (see Figure 4.3 and Figure 4.4), in order to add to the cross sectional area inside the coil. The susceptors heated when placed inside the coil on either side of the specimen, and in turn conducted heat to the specimen through direct contact with it. The susceptors were held in place in contact with the specimen with ceramic ropes.

The susceptors were made of Inconel 718, chosen because of the material's minimal tendency to oxidate at the testing temperatures, in order to avoid contaminating the test specimen with outside oxidation. The bars were machined by the ME Machine shop using the EDM equipment. The final susceptors were 3.75" long with a cross sectional area of 0.625"x0.285". Susceptors with a shorter length were initially used. However, they were shorter than the gage length, leading to a temperature gradient inside the gage length at the ends which caused premature fracture above or below the susceptors where the specimen was at a lower temperature. The final length covered the entire gage length of the test specimens. The width was chosen to maximize surface contact of the susceptor with the specimen, but still allow for attachment of the high temperature extensometer.

A dummy specimen of the  $\gamma$ -MET rolled sheet material was used as a calibration specimen for the coil. Thermocouples were spot-welded at 3 evenly spaced locations across the 2.5 cm gauge length. One of the susceptors was machined with a groove, as can be seen in Figure 4.4, to allow passage of the thermocouple wires during calibration. The coupon was held at zero-load, and the temperature distribution was observed to assess the performance of the coil. The coil was adjusted as necessary to achieve the

desired accuracy. This technique gave a uniform heat distribution, with a gradient within  $\pm 3^{\circ}\text{C}$  of the desired temperature across the 1" gauge length, as specified by ASTM Standard E-21 [88]. A thermocouple attached to the outside of one of the susceptors was also monitored during calibration; the difference between the specimen temperature and the outer thermocouple reading was recorded for the specimen test temperatures. As that temperature gradient was repeatable, it was used as a monitor for the specimen temperature during testing.



Figure 4.4: IN-718 susceptors with thermocouple welded to outside (top) and groove for specimen thermocouples (bottom)

#### *4.1.3.1 Mechanical Testing Procedures*

Monotonic tensile tests were conducted on the sheet material to obtain the general stress-strain behavior of the material. The tests were conducted under isothermal conditions at room temperature,  $700^{\circ}\text{C}$ , and  $800^{\circ}\text{C}$  respectively.

The first set of testing was conducted under load control under a constant load rate of 10.95 lbf/sec. This loading rate was selected as equivalent to a stress rate of 2.56 MPa/sec – which was used by previous testing of TMCs conducted by Johnson et al.

[44], Mirdamadi et al.[45], and previously in this program by Craft [79]. At a steady loading rate, the local strain rate increased rapidly above the yield point. For brittle materials, such as this alloy, an accurate stress-strain curve is difficult to obtain under a steady loading rate due to the rapid, almost immediate fracture that is expected to occur beyond the yield point. Data acquisition was configured to sample time, crosshead displacement, axial load, and axial strain measurements at each incremental change in strain of 0.0005 mm/mm. Load control testing was conducted on one sample at each of the three test temperatures (room temperature, 700°C, and 800°C).

A second set of tests was conducted under displacement control at a constant displacement of 0.0004 in/sec. The crosshead displacement rate was chosen to approximate a strain rate of  $10^{-4}$  mm/mm/sec, which has been used in prior testing of this alloy [59, 62, 78, 79]. Data acquisition was again configured to sample time, crosshead displacement, axial load, and axial strain measurements at each incremental change in strain of 0.0005 mm/mm. Displacement control testing was conducted on samples at room temperature, 700°C, and 800°C. Additionally, two sets of samples were exposed to elevated temperatures for 5 hours before displacement control testing. The first set of coupons were exposed to 800°C for 5 hours, and the second set of coupons were exposed to 700°C for 5 hours. A coupon from the first set was tested at temperature at 800°C, and a coupon from the second set was tested at 700°C. A coupon from each set of exposed specimens respectively was also tested at room temperature.

For each test, a thermocouple welded in the inner groove of one susceptor monitored specimen temperature. The sample was heated to the desired temperature after manually indicating the setpoint temperature on the front panel of the main induction

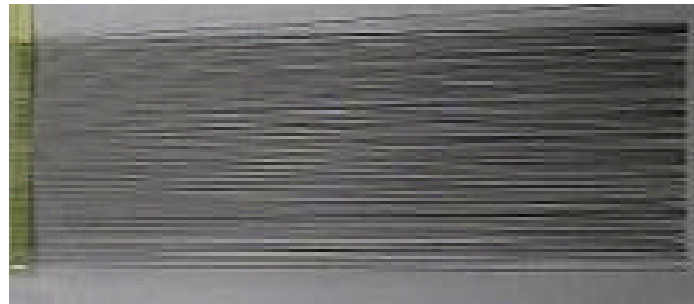
unit. Heating to temperature took approximately 1 min. 45 sec. Prior to heating, the sample was gripped in load control, with zero load applied. This allowed the sample to expand freely during the heating process. The sample was allowed to sit at temperature for 5 minutes prior to testing, to allow the temperature gradient to stabilize along the susceptors and through the specimen. Strain readings due to thermal expansion were not adjusted prior to conducting the test. The temperature was monitored periodically during the test to maintain the testing temperature at  $\pm 2^{\circ}\text{C}$  of the desired temperature.

## **4.2 Manufacturing at NASA LaRC**

The equipment and procedure used to manufacture sample coupons of  $\gamma$ -MET TiAl/SCS-6 composites are described in the following paragraphs. Two sample coupons of gamma titanium aluminide matrix composites with SCS-6 fibers were manufactured at NASA LaRC. The constituents were layers of plasma-sprayed  $\gamma$ -MET foil (described in Section 3.2) as the matrix material and two plies of SCS-6 fiber mat. In the first run, the fiber mat was used without modification. In the second run, every other fiber in the mat was removed to reduce the resulting fiber volume fraction (see Figure 4.5). The laminates were consolidated via vacuum hot pressing.



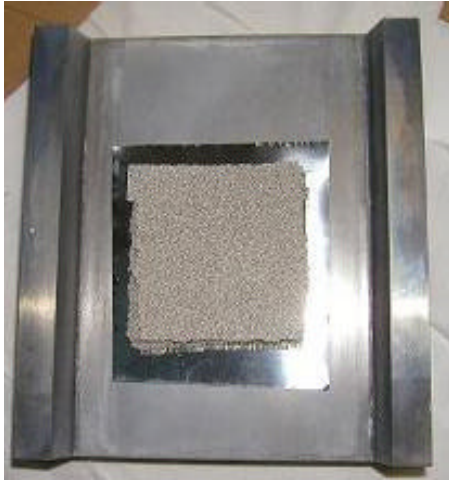
(a)



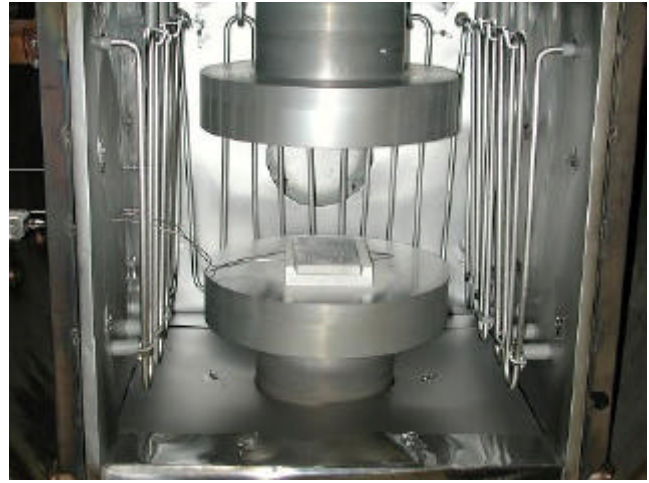
(b)

Figure 4.5: Fiber mat (a) before and (b) after removal of every other fiber

The samples were laid up by hand (see Figure 4.6a). The foil matrix layers were 0.007" thick. The lay-up was as follows: two layers of foil, 1 ply of fibers, 2 layers of foil, 1 ply of fibers, 2 layers of foil. The fiber orientation for both plies was the same, giving an  $[0]_2$  lay-up. The lay-up was placed in a 12.7 cm x 7.6 cm molybdenum die. The lay-up also included thin sheets of molybdenum sandwiching the laminate on either side to protect the laid up material and the die. The VHP facility (pictured in Figure 4.6) has a load capacity of  $1.69 \times 10^6$  N (190 tons) applied to 30.5 cm diameter molybdenum platens. It operates at temperatures up to 1200°C and a vacuum level in the  $10^{-3}$  to  $10^{-4}$  Pa range.



(a)



(b)



(c)

Figure 4.6 Vacuum hot press facility: (a) lay-up on molybdenum die, (b) die on molybdenum platens in furnace, (c) closed furnace chamber and controls

The vacuum hot press cycle used for this work was comprised of a pressure of 103.4 MPa (15 ksi) applied for 2 hours at 1050°C. A typical temperature profile can be seen in Figure 4.7 . For the panel labeled VHP-110, the load was removed when the specimen temperature reached 900°C. For the second panel, labeled VHP-113, the load was removed immediately after consolidation at the consolidation temperature of 1050°C.

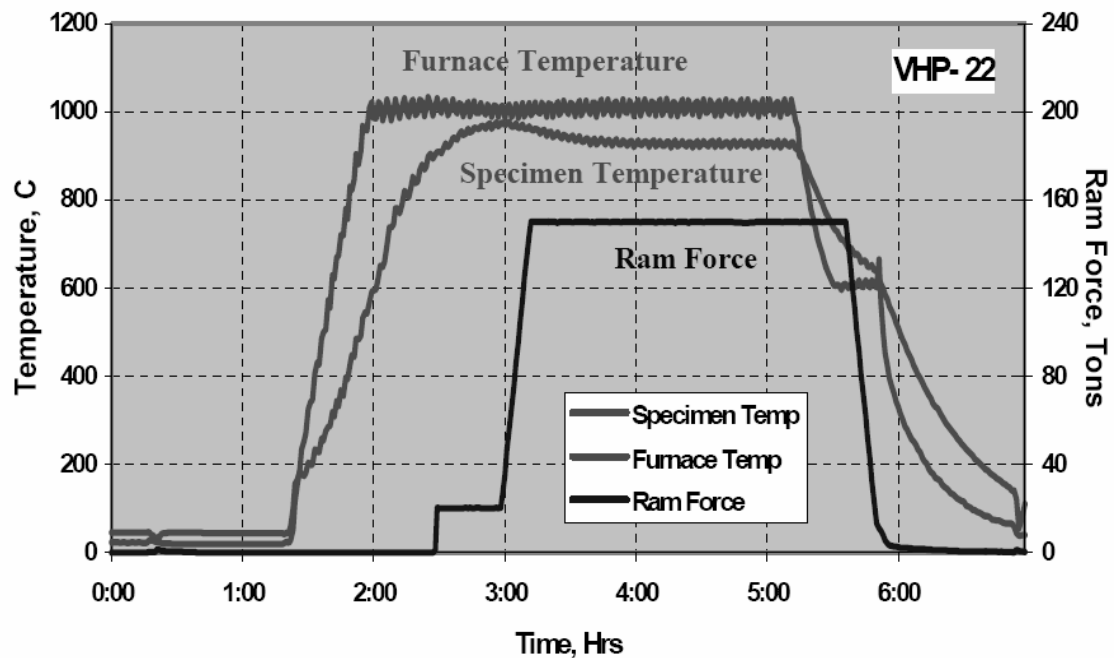


Figure 4.7: Typical VHP temperature/force profile [80]

### 4.3 Analytical Modeling Using AGLPLY

AGLPLY is a 2-D laminate analysis code that predicts the elastic-plastic response of metal matrix composites to thermal and/or mechanical loads. It is also described in Section 2.3.2.1. The model predicts the laminate response based on the constituents'



properties, which can be entered either as fiber and matrix properties or overall lamina properties. The program runs on a DOS prompt. It employs the vanishing fiber diameter (VFD) model, first proposed by Dvorak and Bahei-El-Din [42]. This model assumes that the cylindrical fibers have a vanishing diameter, yet occupy a finite volume in the composite. In this model, the fibers contribute to the longitudinal stress state, but do not interfere with the transverse deformation of the matrix. This assumption models the orthotropic symmetry of the composite by creating a uniform stress state in the transverse plane. The governing equations are simplified by the single-constraint condition in the axial direction, which eliminates the need for complex numerical analysis.

Inputs to AGLPLY can be entered as lamina properties or fiber and matrix properties. These properties include Young's modulus, Poisson's ratio, coefficients of thermal expansion (CTE), yield stress, and stress-plastic strain curves. Each material property can be specified as a piece-wise function of temperature. Property data is linearly interpolated between specified points. AGLPLY has been used extensively to estimate modulus and strengths of various metal matrix composites [22, 27, 89]. AGLPLY is used in this study since no time dependent properties are available for the gamma titanium being studied. If time dependent properties were available, the next iteration of the program, VISCOPLY would have been used, as it accounts for viscoplastic behavior.

For AGLPLY, loads that can be simulated include in-plane stress, out-of-plane normal stress, and uniform temperature change. The program has restart capabilities, allowing for input of piece-wise linear load-time functions in sequential jobs. This option allows for simulation of fabrication and experiments in sequential job steps. Spectrum

load conditions can be applied as well. The program is capable of simulating load-control and strain-control conditions.

## **CHAPTER 5**

### **RESULTS AND DISCUSSION**

In this chapter, the results from the mechanical characterization testing and the analytical results from AGPLY modeling are presented and discussed. The results of the composite manufacturing attempts are also presented.

#### **5.1 Experimental Tests**

Experimental tests were conducted to characterize the  $\gamma$ -MET titanium aluminide, so that this information could be used to predict the behavior of the material in a composite system. The results from the CTE testing, tensile testing, and fatigue testing are presented in the following sections.

##### ***5.1.1 Coefficient of Thermal Expansion***

CTE was determined from dilatometry testing and according to the procedure described in Section 4.1.1. Three specimens were tested to ensure the repeatability of the results. The results from the CTE testing for the three  $\gamma$ -MET sheet material specimens are plotted as a function of temperature in Figure 5.1.

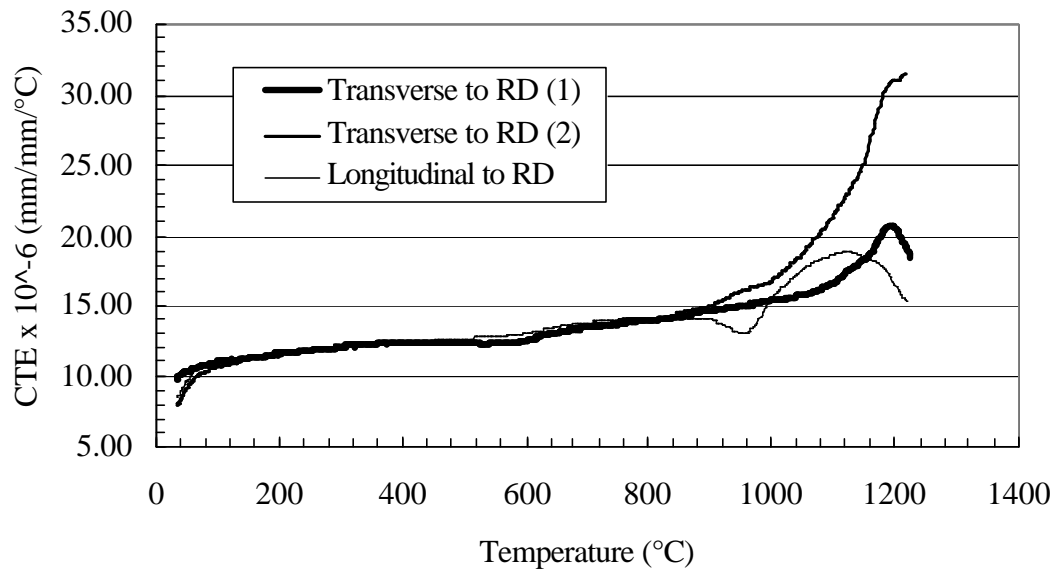


Figure 5.1: Coefficient of thermal expansion vs. temperature for 3 specimens

All three specimens have similar CTE data from room temperature up to around 900-925°C, at which point they begin to diverge. The “dip” in the curve for the specimen that was longitudinal to the rolling direction can perhaps be attributed to the thinness and flatness of the specimens. The thinness of the specimens may have allowed them to bend or curl slightly, which would result in an abnormal change in length reading by the dilatometer, as part of the expansion may have been out of plane from what the pushrods in the dilatometer could detect.

The AGLPLY analysis required the value of the CTE of the matrix material up to 900°C, and the three specimens correlated very well up to that value. Data points used for the analysis were chosen so that the linear interpolation between them would correspond with the average measured CTE values, as can be seen in Figure 5.2.

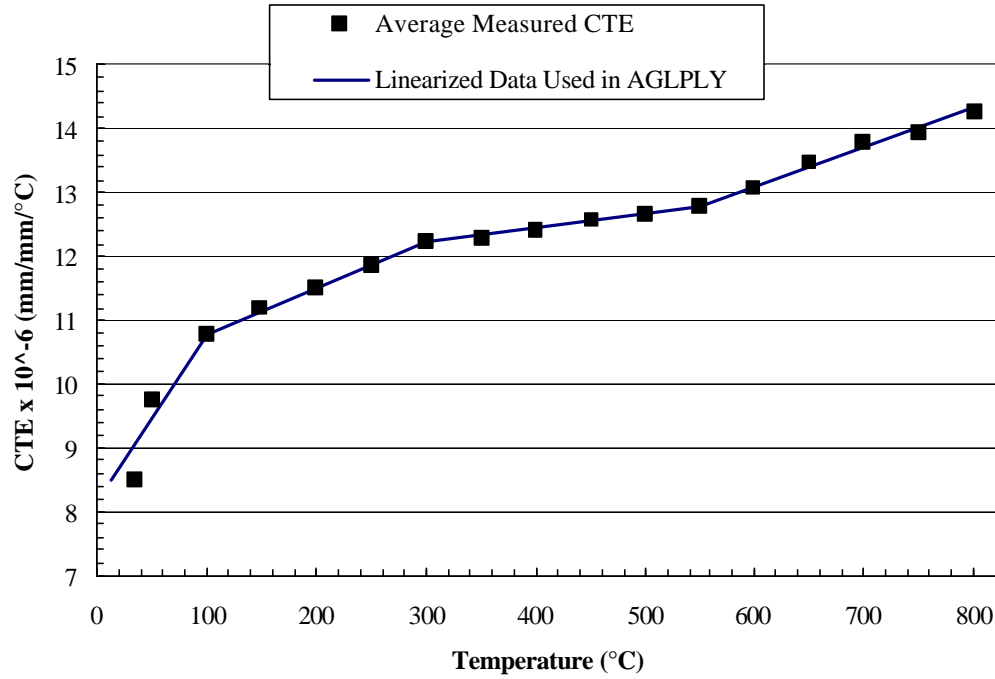


Figure 5.2: Average measured CTE with the linear interpolation of the data used in AGLPLY simulations

### 5.1.2 Poisson's Ratio

Prior to tensile testing, a series of cyclic tests was conducted to verify the room temperature modulus and determine Poisson's ratio. In load control, the load cycled 5 times in the elastic zone. The results from the 0°/90° strain gage rosette from one of these cyclic tests can be seen in Figure 5.3. After 5 tests, conducted to verify the repeatability of the experiments, the average Poisson ratio was 0.237. The average Young's modulus was 153 GPa. This test was only conducted at room temperature, as the strain gages were not rated for elevated temperatures.

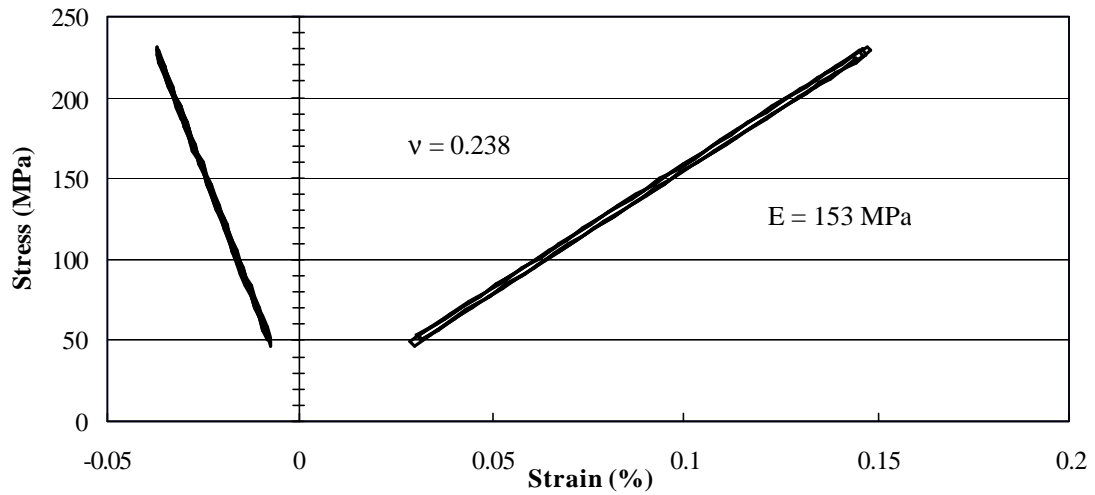


Figure 5.3: Poisson's ratio measured at room temperature under cyclic loading

### 5.1.3 Tensile Testing

Tensile testing of the rolled sheet material was done in both load and displacement control. The curves generated from the load control testing at room temperature, 700°C, and 800°C can be seen in Figure 5.4. Tabulated results from the tensile tests are provided in Table 5.1. The alloy shows good stiffness retention at elevated temperatures. At room temperature, the modulus is 152 GPa; it degrades by only 12% and then 42% at 700°C and 800°C respectively. The RT moduli correlate well with the previously published data seen in Table 2.1, where the reported RT modulus ranges from 139-162 GPa. At 700°C, the modulus is 18% higher than one literature source [79], and 2% lower than another source [81]. At 800°C it is 26% higher than one literature source [62] and 30% lower than another source [81], thus falling between the two. Ductility improves with temperature, with inelastic elongation increasing from 0.56% at room temperature up to 4.72% at 800°C. The results also show good strength retention. The high yield strength at room temperature was degraded by only 18% and

28% at 700°C and 800°C. The ultimate tensile strength, on the other hand, remained relatively unchanged with increasing temperature. The increase in ductility at elevated temperatures and unchanged high tensile strength result in a tougher material at elevated temperatures.

The failure occurred at the top or bottom edges of the reduced section for both the elevated temperature tests. This was attributed in part to the large thermal gradient occurring at those locations, as only the center of the specimens were inductively heated. Another possible reason for the failure occurring near the ends of the reduced section is possible poor alignment. The bottom of the test machine can rotate, which would induce an additional torsional load that would be greatest at the ends of the reduced sections. Additionally, stress may have been induced in the specimens during gripping if the pressure used to grip the thin specimens was not optimal.

For brittle materials such as this alloy, an accurate stress-strain curve is difficult to obtain under a steady loading rate due to the rapidly increasing strain rate above the yield stress. Therefore, it is not unexpected that the ductility data from these tests is lower than those reported from strain-controlled testing in Table 2.1. The trend of increasing ductility with temperature, however, remained the same.

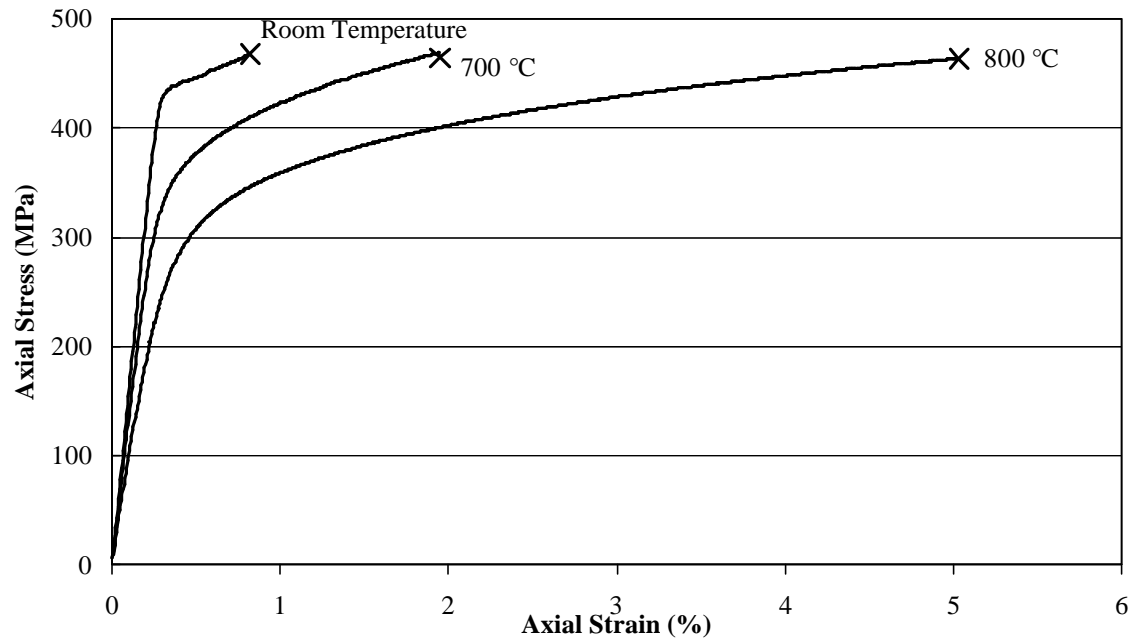


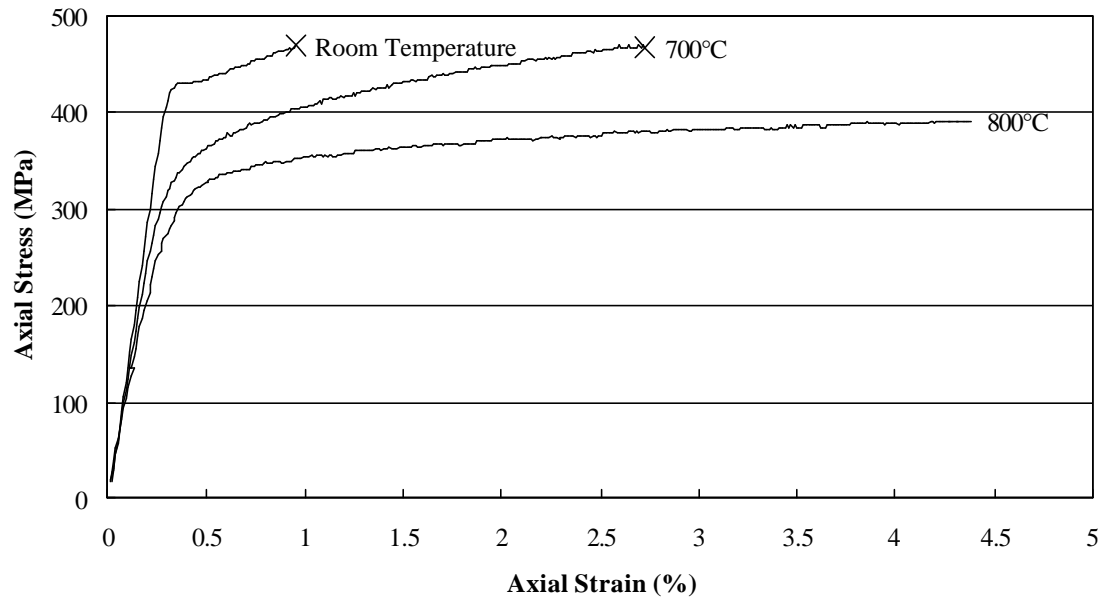
Figure 5.4: Stress-strain curves of sheet material from load control testing

Table 5.1: Material properties results from load control testing

Temperature, °C	Young's Modulus, GPa	0.2% Yield Strength, MPa	Ultimate Tensile Strength, MPa	Total Elongation, %	Plastic Elongation, %
RT	152	445	468	0.82	0.56
700	133	365	469	1.95	1.45
800	88.5	320	464	5.03	4.47



Monotonic tensile tests in displacement control, with a crosshead displacement rate chosen to approximate a strain rate of  $10^{-4}$  mm/mm/sec, were also performed at room temperature, 700°C, and 800°C. Two tests were performed at room temperature. Typical stress-strain curves from those tests can be seen in Figure 5.5. Tabulated data for the material properties found from this testing can be examined in Table 5.2. The trends for the displacement control testing were very similar to those from load control testing. The modulus degraded with temperature, by about 20% and 30% at 700°C and 800°C respectively. The ductility again increased with temperature, though in greater amounts. This is unsurprising, as load control testing of brittle materials often leads to lower ductility findings. At 800°C, the specimen strained by more than 20% before breaking which correlates well with the data given in the literature. Good yield strength retention was seen again, with an average degradation of 20% and 27% at 700°C and 800°C. The ultimate tensile strength did not appear to degrade in this case until the testing at 800°C.



\* Only partial curve at 800°C is shown

Figure 5.5: Stress-strain curves of sheet material from displacement control testing

Table 5.2: Material properties results from displacement control testing

Temperature, °C	Young's Modulus, GPa	0.2% Yield Strength, MPa	Ultimate Tensile Strength, MPa	Total Elongation, %	Plastic Elongation, %
RT	144	469	497	0.90	0.38
RT	147	434	469	0.96	0.47
700	118	362	466	2.72	2.23
800	105	330	401	>20	>20

The test at 700°C again resulted in failure near the end of the reduced section, although the specimen tested at 800°C failed near the middle of the gage length. This is attributed to the lesser temperature gradient that occurs when the specimen is heated to 800°C, as the temperature at the ends of the reduced section is higher and ductility there is increased.

Additional monotonic tensile testing was performed on specimens that had been exposed to elevated temperatures (700°C and 800°C respectively) for 5 hours. The specimens exposed to 800°C formed a visible thin, brittle whitish oxide layer, whereas only a few, very thin isolated islands of the whitish oxide were observed on the specimens exposed to 700°C. Those specimens were slightly discolored with yellow and rust colored tones, however, compared to the silver metallic color of the unexposed specimens. The stress-strain curves generated from tensile testing of those specimens can be seen in Figure 5.6 and Figure 5.7 along with comparison curves from tensile testing of unexposed samples.

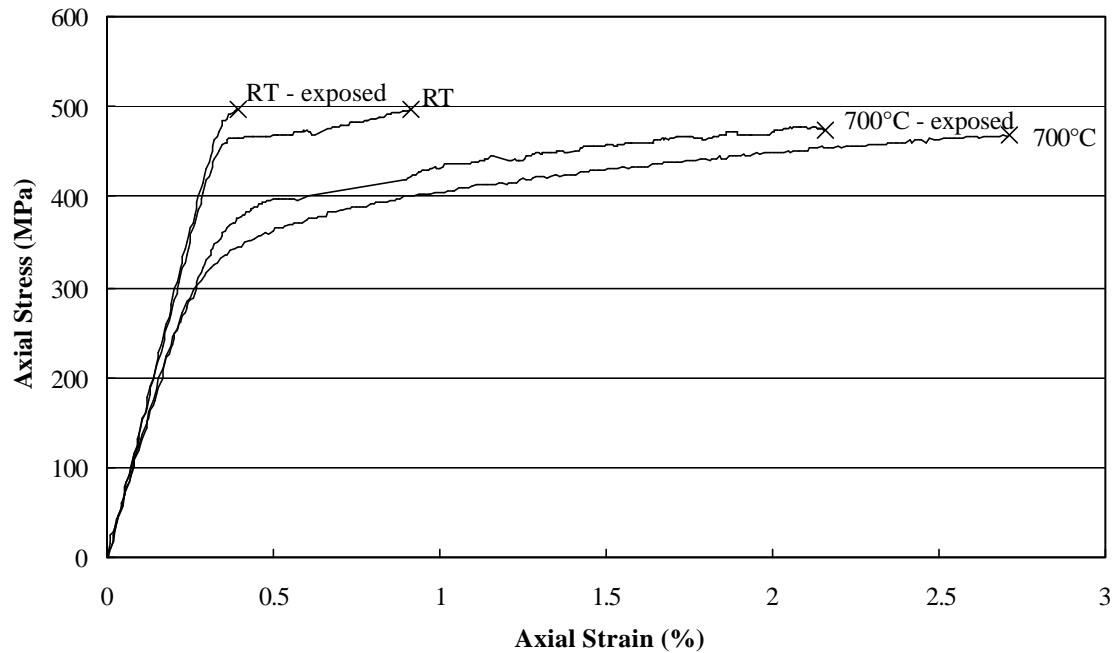


Figure 5.6: Stress-strain curve comparisons of unexposed specimens and specimens exposed to 700°C for 5 hours

The testing of specimens exposed to 700°C was disappointing in that several specimens broke in the grip section during both the room temperature test and the test at 700°C. The curves in Figure 5.6 include the one exposed specimen that failed in the reduced area at room temperature. This specimen did not demonstrate any plastic strain, however, indicating a loss of room temperature ductility. Though no significant visible oxide layer was formed, the discoloration of these specimens indicates some oxygen or hydrogen uptake that had an embrittling effect. As mentioned previously, Pather, et al. [73] observed a decrease in RT ductility of another gamma alloy after exposures as short as 2 hr at 700°C, which was also attributed in part to the surface residual stresses induced from the exposure. The exposed specimen tested at 700°C failed in the grip area, but did strain plastically before failure. From the data obtained, the exposure does not seem to

indicate a great loss of ductility at 700°C – the loss was about 20%, keeping in mind that failure occurred in the grip area. The exposure did not affect either the modulus or the ultimate tensile strength at room temperature or at 700°C. The exposed specimens exhibited an increase in 0.2% yield strength at both temperatures, as can be seen in Table 5.3.

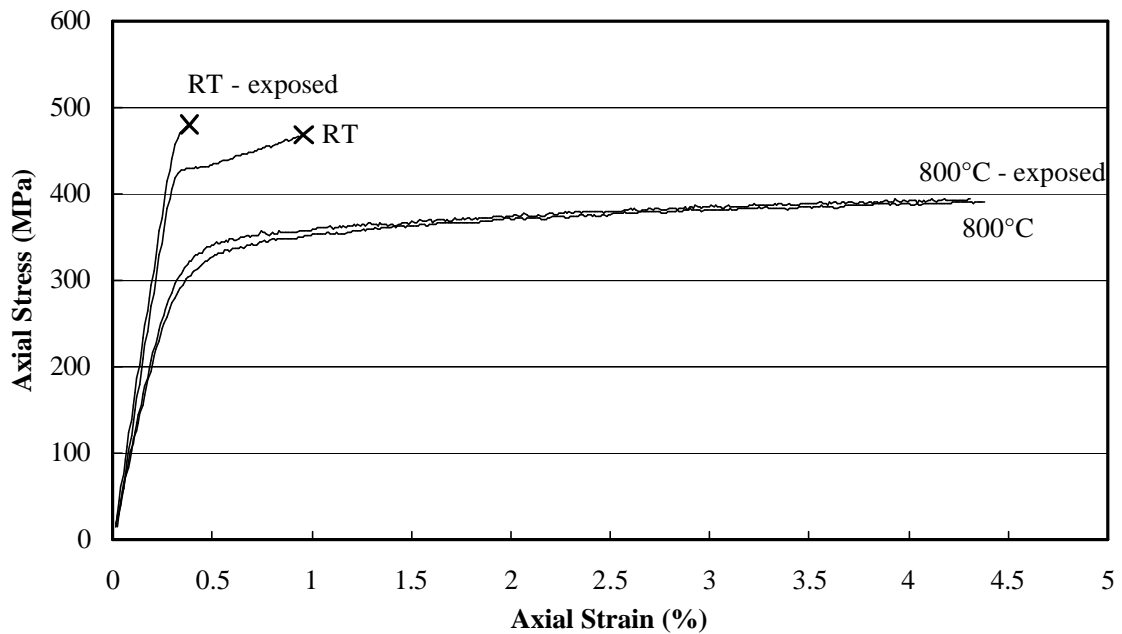


Figure 5.7: Stress-strain curve comparisons of unexposed specimens and specimens exposed to 800°C for 5 hours

The specimens exposed to 800°C exhibited behavior very similar to those exposed to 700°C. The brittle oxide layer that formed on the specimens exposed to 800°C did not significantly affect the mechanical properties of the alloy when tested at 800°C. When tested at room temperature, however, the oxide layer appeared to slightly strengthen and stiffen the alloy, increasing the modulus and yield strength by 6% and the ultimate tensile strength by 10%. The oxide formed was previously determined to be comprised of  $\text{Al}_2\text{O}_3$  and  $\text{TiO}_2$ . This strong, stiff, and very thin oxide layer may contribute

slightly to the strength and stiffness of the thin specimen. However, as has been seen with other gamma alloys, these effects were accompanied with a loss of room temperature ductility (of about 30% in this case) when compared to the unexposed material properties. The oxide layer is very brittle and can cause surface cracking; it provides preferential locations for microcracks to start on the surface or at the oxide/alloy interface. The material properties extracted from these tests can be seen in Table 5.3.

Table 5.3: Material properties comparison for exposed and unexposed specimens

Temperature, °C	Exposure Condition	Young's Modulus, GPa	0.2% Yield Strength, MPa	Ultimate Tensile Strength, MPa	Total Elongation, %	Plastic Elongation, %
RT	Unexposed*	148	452	483	0.92	0.42
RT	5 hr at 700°C	149	505**	505	0.42	--
RT	5 hr at 800°C	157	480	533	0.66	0.33
700	Unexposed	118	362	466	2.72	2.23
700	5 hr at 700°C	118	399	477	2.17	1.62
800	Unexposed	105	330	401	>20	>20
800	5 hr at 800°C	113	340	403	>20	>20

\*Average values used for unexposed RT properties

\*\*Failed before yielding

#### 5.1.4 Fractography

The fracture surfaces of the specimens tested were examined to evaluate the damage mechanisms. The micrographs provide a cross-sectional view of the entire thickness. Figure 5.8 shows fracture surfaces for the material tested at room temperature. Both the unexposed and exposed materials showed brittle cleavage fracture at room temperature. The brittle oxide layer on the exposed specimen is almost too thin to be discernible in the micrograph. The fracture mechanism was not affected by the elevated temperature exposure, as brittle cleavage fracture occurred in every case.

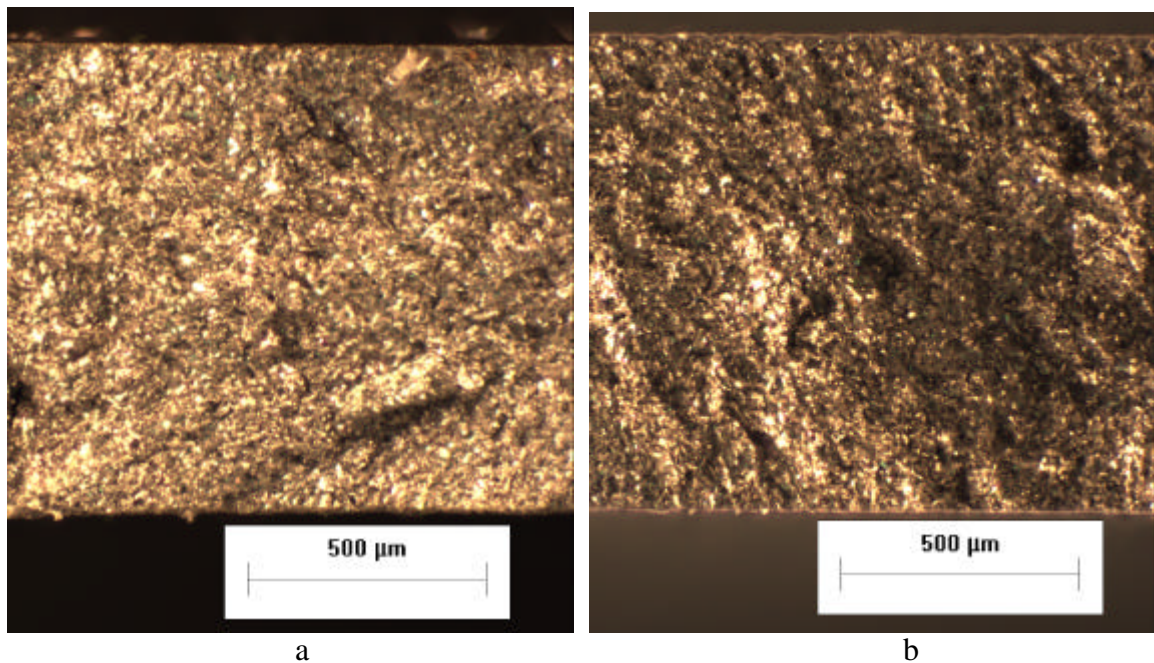


Figure 5.8: Cross-sectional fracture surfaces of material tested at room temperature in conditions: a) unexposed and b) exposed to 800°C for 5 hours

Unfortunately, at 700°C the specimens broke near the ends of the gage length. The fracture surfaces there also involved brittle cleavage, similar to the surfaces seen in



Figure 5.8. This is unsurprising, considering the temperature gradient from the hot center 25.4 mm (1”) section at 700°C to the grips, which are estimated to be around 100°C. The susceptors were not “glowing” hot near the ends of the reduced section, implying the temperature is lower in those locations. The transition from cleavage fracture to intergranular fracture usually occurs somewhere above 600°C for gamma titanium aluminides [4]; the fracture location is not estimated to have been above that temperature.

For the specimens tested at 800°C, fracture did occur in the 25.4 mm (1”) gage section at 800°C. Unfortunately, with the susceptors in place, it was difficult to safely remove the fracture surface from the elevated temperatures without the surface oxidizing. The oxidation on the surface prevented determination of the fracture mechanism. The specimen did exhibit necking behavior before fracture, and the fracture surface was much flatter than those tested at room temperature. Previous testing of the sheet material at 650°C demonstrated a transition to more intergranular fracture at higher temperatures [79], as would be expected for these specimens.

## **5.2 Analytical Predictions**

Analytical modeling was performed to assess the potential performance of  $\gamma$ -MET/Ultra-SCS and  $\gamma$ -MET/Nextel 610 composite systems. The analysis utilized an  $[0]_4$  lay-up in order to mimic the lay-up of the samples manufactured at NASA LaRC. It is important to note that most high temperature applications would require a more complex lay-up than the unidirectional setup modeled here. Observations from previous consolidation attempts and the mechanical performance of the “fiberless” coupons tested previously were used to calculate a “lock-up” temperature of 925°C, as will be described. The subsequent analysis assumed this “lock-up” temperature and used the optimal matrix

properties found in the literature to determine potential composite behavior. The first step of the analysis determined the residual stress-state that develops from thermal mismatch during cooling. The second step predicted subsequent loading behavior of the composite systems at various temperatures, including the residual stresses induced during cooling.

As time-dependent material parameters were not available, the composite analysis was based on the assumption of no time dependent effects. As mentioned earlier, if time dependent properties were available, the analysis would have utilized a code that takes those properties into effect, such as VISCOPLY. However, with the data available, the laminate code AGLPLY was used for this analysis.

### **5.2.1 *Material Parameters***

As this analysis was performed to find the *potential* performance of these composite systems, the higher properties seen in the literature for the alloy were used to determine the feasibility of manufacturing these laminates *assuming that optimal matrix properties could be achieved*. For the analysis, the tensile data published in Clemens et al. [59], shown graphically in Figure 2.16, was used to approximate the Young's modulus, yield strength, and stress-plastic strain behavior of the matrix material. Upon reviewing the other published property data of this alloy and experimental test results, the tensile results from Figure 2.16 exhibit higher stiffness and strength retention characteristics at elevated temperatures compared to the results reported in Table 2.1. It should be mentioned that mechanical properties vary significantly with alloy content and processing; the variance amongst reported data for material with the same nominal content could be seen in Table 2.1.

Stress-strain curves were approximated using the published yield strength, ultimate tensile strength and failure strain data. The Poisson ratio was measured experimentally using a 0°/90° strain gage rosette under tensile cyclic loading, as described in Section 5.1.2. The experimental data for the CTE from Section 5.1.1 was also used. A summary of matrix material properties used in AGLPLY is given in Table 5.4.

Specialty Material's Ultra-SCS silicon carbide fiber was one of the fibers considered in the analysis. This fiber is desirable because of its high stiffness and tensile strength, but it has a much more significant thermal mismatch with gamma titanium aluminides than the alumina fiber. Room temperature modulus was obtained for the Ultra-SCS fiber from Specialty Materials. Temperature dependent property data is readily available for the SCS-6 fiber (also from Specialty Materials) [33, 45]. As the composition of the two fibers is very similar, the assumption was made that temperature dependent trends would correlate between the SCS-6 and the Ultra-SCS fiber. The temperature dependent Young's modulus of the Ultra-SCS fiber was estimated by applying a 10% increase to the modulus of the SCS-6 fiber at all temperatures. A summary of representative material property data used for the Ultra-SCS silicon carbide fiber is provided in Table 5.5.

Table 5.4:  $\gamma$ -MET material parameters used in AGLPLY simulations

Temperature, °C	Elastic Modulus <sup>1</sup> , GPa	Poisson's Ratio, v	CTE, mm/mm/°C	Yield Stress <sup>1</sup> , MPa	Plastic Stress-Strain Curve <sup>1</sup> , MPa		Ultimate Tensile Strength <sup>1</sup> , MPa	Total Elongation <sup>1</sup> , %
					(0.6% Elong.)	(1.2% Elong.)		
21	155	0.244	8.50E-06	545	588	616	627	1.4
100	153	0.244	10.77E-06	527	580	610	615	1.6
300	149	0.244	12.22E-06	498	566	583	595	2.1
550	140	0.244	12.77E-06	475	530	550	672	5.0
700	135	0.244	13.76E-06	471	510	518	668	21.9
800	127	0.244	14.35E-06	380	399	400.6	437	69

<sup>1</sup> Clemens, et al. in Gamma Titanium Aluminides 1999 [59]

Table 5.5: Ultra-SCS material parameters used in AGLPLY simulations

Temperature, °C	Young's Modulus, GPa	Poisson's Ratio, v	CTE, mm/mm/°C
21	415	0.25	3.56E-06
315	403	0.25	3.73E-06
537	395	0.25	4.07E-06
871	381	0.25	4.57E-06

Table 5.6: Nextel 610 material parameters used in AGLPLY simulations [90, 91]

Young's Modulus, GPa	Poisson's Ratio, v	CTE, mm/mm/°C
372	0.26	8.00E-06

The other fiber considered in this analysis was 3M's Nextel 610 alumina fiber. Though less stiff than the silicon carbide fibers, it has a higher CTE that is a closer match to the CTE of the matrix material. Room temperature Young's Modulus and CTE property data for the Nextel 610 fiber was obtained from 3M Corporation [90]. An estimate for Poisson's ratio was used for  $\text{Al}_2\text{O}_3$  [91]. Since temperature dependent property data was unavailable, mechanical properties were modeled as independent of temperature for the Nextel 610 fiber. As CTE generally increases with temperature, this model serves as a conservative estimate for the residual stresses that would occur, as the thermal mismatch may be less at higher temperatures. A summary of representative material property data used for the Nextel 610 alumina fiber is provided in Table 5.6.

### ***5.2.2 Calculating the "Lock-up" Temperature***

The "lock-up" temperature is essentially the temperature at which the fibers and matrix become perfectly bonded. Generally, it is not known at what temperature the fiber and matrix "lock-up" during cooling from consolidation. In the past for TMCs, it has been assumed that creep relieves any thermal stresses that develop at temperatures greater than one half the melting point of the matrix [33]. This rule-of-thumb assumption would give a "lock-up" temperature of about 725°C for a  $\gamma$ -MET matrix system. However, the first step of the analysis, determining the residual stress state, is very sensitive to the "lock-up" temperature, such that a more accurate estimate for it was desirable. Therefore the "lock-up" temperature was calculated using observations of past consolidation attempts and data from the previous experimental testing previously performed on the fiberless composite coupons in the AGLPLY analysis.

In past consolidation attempts of a  $\gamma$ -MET/SCS-6 laminate at NASA LaRC, transverse cracking due to thermal mismatch was observed for fiber volume fractions as low as ~20%. This observation implies a higher “lock-up” temperature than the initially assumed 725°C, as no cracking is predicted assuming this lower “lock-up” temperature. Therefore an AGLPLY analysis of the residual stresses induced from thermal mismatch was run using a volume fraction of 20%, various “lock-up” temperatures, and the material properties from Table 5.4 and Table 5.5. The tensile data for the fiber-less composite tested previously at MPRL demonstrated an ultimate stress of 497 MPa at room temperature (see Table 2.1). This data was used as the criterion for thermal mismatch cracking at room temperature. As the “lock-up” temperature used in the analysis increased, the residual stress predicted at room temperature increased. A “lock-up” temperature of 925°C was determined to induce a residual stress of 497 MPa at room temperature with a volume fraction of 20%, which would presumably cause cracking. Therefore this “lock-up” temperature was assumed for all subsequent analyses. This temperature also correlates with the temperature at which the CTE results diverged for the three test specimen, as was seen in Figure 5.1. The temperature is also very similar to the assumed “lock-up” temperature used for other TMCs [92].

### **5.2.3 Residual Stresses**

After calculating the “lock-up” temperature, the next step was to analyze the residual stresses that developed as a result of thermal mismatch during consolidation. The constituents are consolidated at high temperatures and then the materials are allowed to cool in the furnace to room temperature. As the CTE of the matrix is larger than that

of the fiber, tensile residual stresses develop in the matrix upon cooling. If the stresses in the matrix exceed the material's tensile strength, cracking will result.

As could be seen in Table 2.1, the consolidated fiber-less samples resulting from the recent trials at NASA LaRC do not possess the optimal properties that have been seen in this alloy. Therefore an analysis using the “lock-up” temperature determined above was used to determine the feasibility of manufacturing a SCS-6/ $\gamma$ -MET laminate assuming that optimal matrix properties could be achieved. The potential residual stress state was determined using the optimal matrix properties, listed in Table 5.4, and the determined “lock-up” temperature. As the resulting residual axial tensile stress in the matrix material seems to be the limiting factor for the manufacturing of these composite systems, these stresses for various fiber volumes of an  $[0]_4$  Ultra-SCS/ $\gamma$ -MET composite are shown in Figure 5.9.

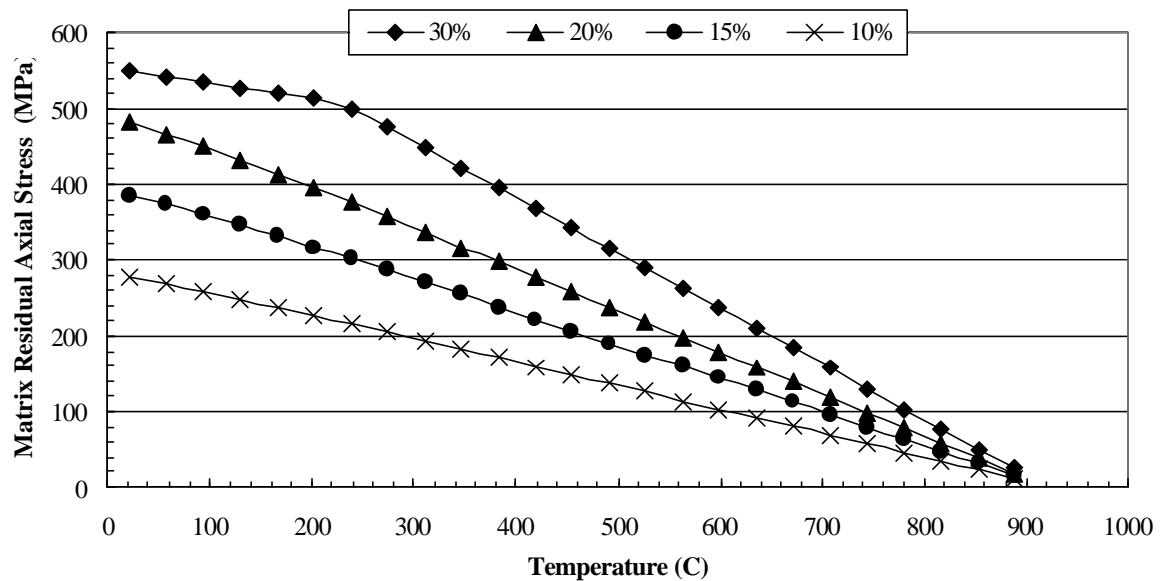


Figure 5.9: Matrix residual axial stress due to thermal mismatch for various fiber volumes of an  $[0]_4$  Ultra-SCS/ $\gamma$ -MET composite

The residual axial stress that develops in the matrix is high, with yielding predicted at about 225°C during cool-down for a composite with 30% volume fraction. Ideally, the residual stress state would remain elastic in cooling to room temperature. Given the poor room temperature ductility of the fiberless consolidated material, which did not yield plastically at all in one case [79], it is predicted that cracking would result in this laminate upon cooling to room temperature. To prevent cracking upon cooldown, it is necessary to reduce the fiber volume fraction in order to reduce the amount of thermal mismatch taking place. While AGLPLY does not predict matrix yielding upon cool-down with a volume fraction of 20%, the usefulness of the laminate is unclear when considering the amount of additional load that can be applied in service before eventual yielding and/or cracking occurs in the matrix.

The residual axial stress of the matrix modeled with various volume fractions of Nextel 610 fibers is shown in Figure 5.10. Similar trends were observed in this laminate, when comparing it with the [0]<sub>4</sub> Ultra-SCS/ $\gamma$ -MET composite. The overall magnitude of residual stresses was lower than the previous analysis, attributed to the higher CTE of the Nextel 610 alumina fiber which is a better match for the CTE of the matrix material. For this reason, no yielding was observed for the 30% volume fraction of this laminate.



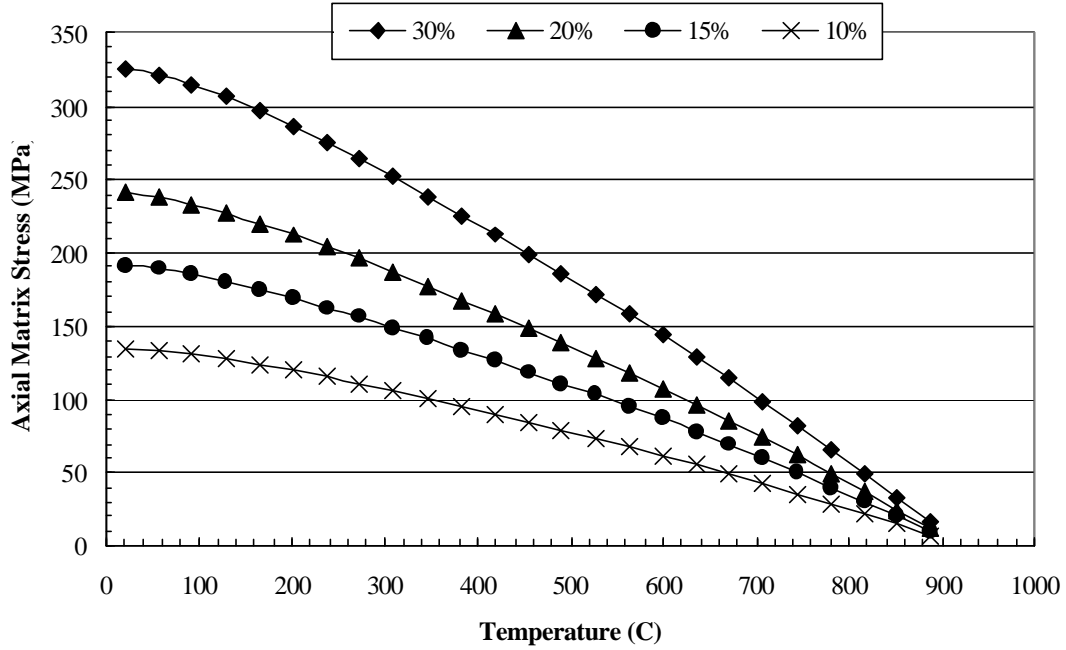


Figure 5.10: Matrix residual axial stress due to thermal mismatch for various fiber volumes of an  $[0]_4$  Nextel 610/ $\gamma$ -MET composite

Since no mechanical loads were applied to the laminates, the residual stress contributions of the constituents must result in zero stress overall. As the constituents were constrained in the axial direction because of the interfacial bond, the stresses were governed by the rule of mixtures:

$$\sigma_L = v_f \sigma_f + (1 - v_f) \sigma_f = 0 \quad (5.1)$$

The residual stresses in the fibers found from the analysis were compressive for both the Ultra-SCS/ $\gamma$ -MET and Nextel 610/ $\gamma$ -MET systems, as expected, and were increasingly compressive with increasing fiber volume fraction. No shear residual stresses developed.

#### 5.2.4 Subsequent Monotonic Loading Capabilities

The generic flight profile previously generated for TMCs in the NASP program [44, 45] seen in Figure 5.11 was used as a guideline in evaluating the monotonic response of these laminates. Though this guideline was not developed necessarily for unidirectional laminates, it was used simply to determine the practicality of using these material systems in a generic high temperature application. Tensile stress-strain curves were generated for the laminates at 21°C, 400°C, and 700°C under isothermal conditions and monotonic loading. The flight profile calls for a laminate stress of nearly 300 MPa at room temperature. The laminate must also carry a peak load of up to 350 MPa at 400°C. From Craft's work [79], the maximum allowable temperature exposure with no significant oxide degradation is 700°C, and thus the maximum load at this temperature is predicted as well. Matrix yielding is applied as the failure criterion since the room temperature ductility is very low.

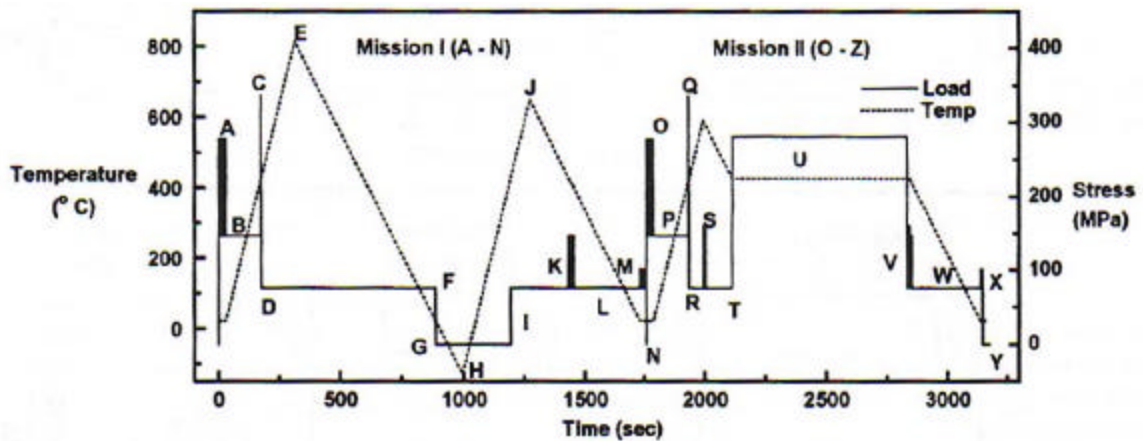


Figure 5.11: Generic hypersonic flight profile [45]

Table 5.7 lists stiffness and maximum laminate stress (based on pure elastic behavior in the constituents) for Ultra-SCS/ $\gamma$ -MET laminates with various fiber volume fractions. With a RT composite strength (based on matrix yield criteria) of 315 MPa and an effective Young's Modulus of 181 GPa, a fiber volume fraction of 10% was close to a maximum reinforcement without sacrificing the usefulness of the laminate. At 400°C, the laminate with a fiber volume fraction of 10% is predicted to carry less load than the non-reinforced matrix material, though the stiffness at this temperature would be improved by about 20%. The reinforced material is predicted to carry 380 MPa, which satisfies the specification of carrying a 350 MPa load at 400°C. At the maximum allowable temperature without degradation, 700°C, the laminate is predicted to carry about the same load as the non-reinforced material, but again improves the stiffness by about 20%. The addition of Ultra-SCS fibers to the  $\gamma$ -MET matrix material therefore improves the stiffness, but generally degrades the load carrying capacity of the non-reinforced matrix material.

Table 5.7: Overall laminate properties of  $[0]_4$  Ultra-SCS/ $\gamma$ -MET

At 21°C			At 400°C			At 700°C		
Fiber Content	Young's Modulus, GPa	Load Capacity, MPa	Fiber Content	Young's Modulus, GPa	Load Capacity, MPa	Fiber Content	Young's Modulus, GPa	Load Capacity, MPa
30%	129	0						
20%	207	74						
15%	194	200						
10%	181	315	10%	170	380	10%	160	475
0%	155	545	0%	144	488	0%	135	470

The trends in stress-strain behavior of the Nextel 610/ $\gamma$ -MET laminates were similar to laminates with silicon carbide reinforcement. One difference to note is a lower stiffness for equal fiber content because of the lower modulus of the alumina fiber. However, with lower residual stresses, larger fiber content can be used; this results in a stiffer laminate that can withstand higher loads.

Table 5.8 lists stiffness and maximum laminate stress (based on pure elastic behavior in the constituents) for Nextel 610/ $\gamma$ -MET laminates with various fiber volume fractions. With a composite strength of 312 MPa and a modulus of 214 GPa at room temperature, a fiber volume fraction of up to 30% could be achieved without sacrificing the usefulness of the laminate. At 400°C, the laminate with a fiber volume fraction of 30% is predicted to carry a lower load than the non-reinforced matrix material, though the stiffness at this temperature is improved by almost 50%. The load carried by this laminate again meets the required 350 MPa load carrying capacity at 400°C from the generic hypersonic flight profile. Finally at 700°C, as the residual stresses relax, the  $v_f = 30\%$  laminate improves both in stiffness as well as in load carrying capacity over the non-reinforced material. This combination of fibers and matrix provides an improved thermal match. Therefore the Nextel 610 alumina fibers can better improve the stiffness of the laminate compared to the non-reinforced matrix material without sacrificing as much load carrying capacity as the Ultra SCS/ $\gamma$ -MET combination.

Table 5.8: Overall laminate properties of  $[0]_4$  Nextel 610/-MET

At 21°C			At 400°C			At 700°C		
Fiber Content	Young's Modulus, GPa	Load Capacity, MPa	Fiber Content	Young's Modulus, GPa	Load Capacity, MPa	Fiber Content	Young's Modulus, GPa	Load Capacity, MPa
30%	214	312	30%	213	396	30%	206	563
20%	204	389						
15%	194	428						
10%	184	582						
0%	155	545	0%	144	488	0%	135	470

As temperature increases, the toughness of the alloy increases while the stiffness decreases. The matrix residual stresses also relax with increasing temperature. The overall effect is that the laminate could carry more load, and thus these materials show great promise for elevated temperature application. However, it is important to note that even though the structures heat up during flight, significant loads would be applied at lower temperatures, during take-off and initial flight maneuvers. Therefore, focus on room temperature performance is critical.

The analytical modeling results reinforce that thermal mismatch limits the use of gamma titanium aluminides in composite systems. With Ultra-SCS reinforcements, a maximum fiber content of 10% can be added without compromising the load carrying capability of the laminate. The result is an improvement in stiffness of 16% at room temperature compared with the un-reinforced alloy. The thermal mismatch is reduced when using alumina Nextel 610 fibers as reinforcements. A larger fiber content of 30% could be used without compromising the load carrying capability of the laminate with these fibers. The stiffness in this case is improved by 38% over the un-reinforced alloy

### 5.3 Manufacturing at NASA LaRC

Two attempts were made at NASA LaRC to manufacture small panels of plasma sprayed  $\gamma$ -MET foil matrix composites with SCS-6 fibers. The first panel had about twice the number of fibers as the second. For the second panel, every other fiber in the mat was removed. They were both consolidated at 1050°C and 15 ksi for hours. For the first run, labeled VHP-110, the panel was cooled to 900°C, near the estimated lock-up temperature, and then the load was removed. For the second run, labeled VHP-113, the load was removed immediately after consolidation (at 1050°C).

The temperature at which the pressure was released has been varied in past consolidation attempts – observations indicated that the amount of surface cracking decreased when the pressure was relieved at 800°C as opposed to 700°C [93]. If the pressure remains after the “lock-up” temperature, the applied pressure will induce even larger residual stresses than the thermal mismatch alone. The “lock-up” temperature is essentially the point at which the constituents become perfectly bonded. In the past for TMCs, generally it has been assumed that creep relieves any thermal stresses that develop at temperatures greater than one half the melting point of the matrix [45]. However, the analysis (see Section 5.1.4.2) suggested a “lock-up” temperature of 925°C, implying that releasing the pressure at a higher temperature may help relieve some of the induced residual stress and lead to successful consolidation.

Even with the higher release temperature, external surface cracking still occurred in the samples as can be seen in Figure 5.12. The cracking is transverse to the fiber direction, and is due to the high longitudinal tensile stresses induced in the matrix by the thermal mismatch.

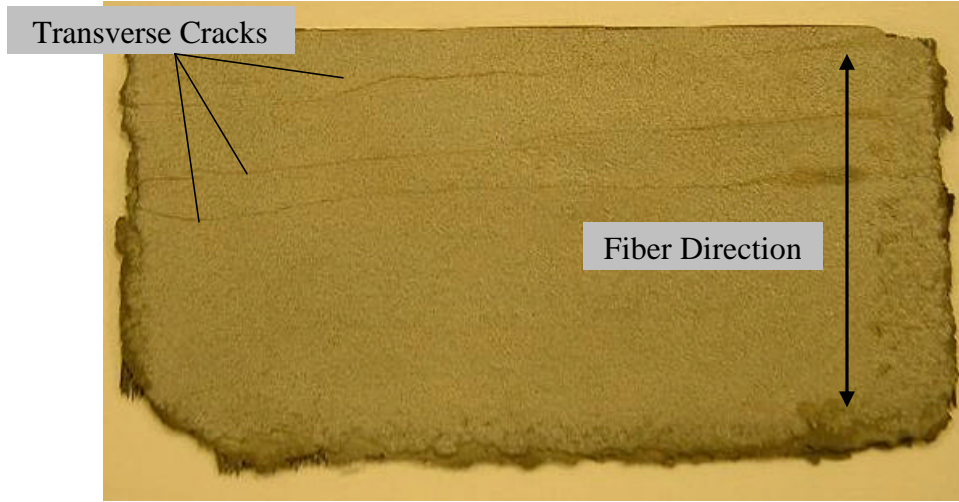
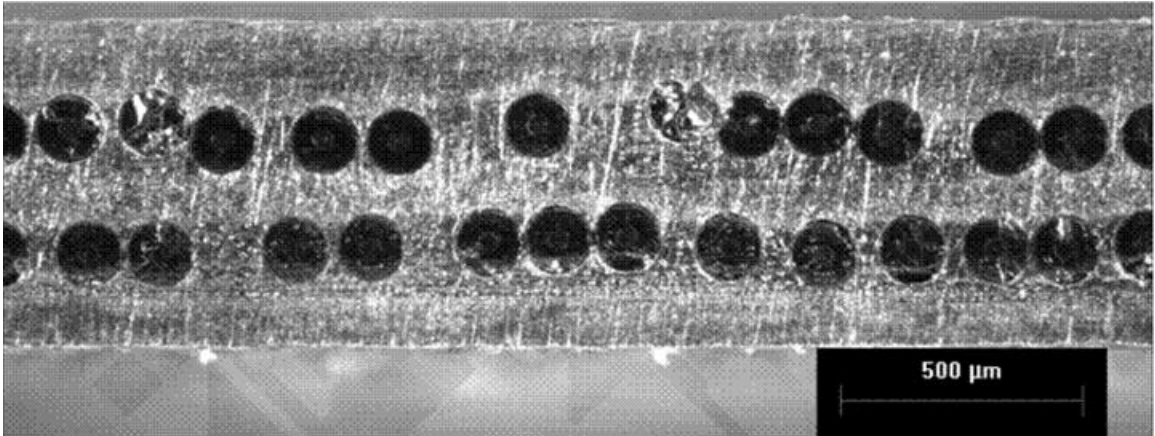


Figure 5.12: Cracking in  $[0]_2$  SCC-6/ $\gamma$ -MET panel (VHP-110) after consolidation

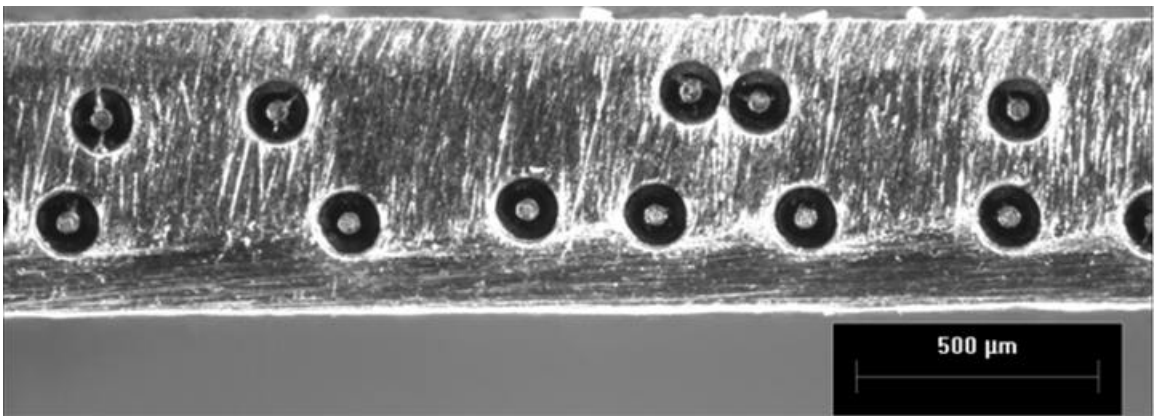
The cracking is attributed to the thermal mismatch between the SCS-6 fibers and the gamma matrix material. The fiber volume fraction,  $v_f$ , was determined by a simple area ratio:

$$v_f = \frac{A_f}{A_{tot}} \quad (5.2)$$

where  $A_f$  is the area covered by the fibers and  $A_{tot}$  is the total area of a cross-sectional view of the consolidated sample (see Figure 5.13). The fiber volume fraction was calculated to be about 22% for VHP 110 and 11% for VHP 113.



(a)



(b)

Figure 5.13: Cross-sectional view of composite samples a) VHP 110 and b) VHP 113



The cracking is unsurprising in the VHP 110 panel with the volume fraction of fibers of 22%, as this is the cusp of the allowable volume fraction noted in the AGLPLY analysis section. Additionally, internal cracking between adjacent fibers was seen in this panel. This is likely due to the close transverse spacing of the fibers, as can be seen in Figure 5.13(a). The fibers are spaced much more closely in the transverse direction than in the through thickness direction, and have a higher likelihood of fiber-touching in that direction. Even with the lower volume fraction in the VHP 113 panel, the method of hand-laying up the plies can allow some fiber-touching, as can be seen in Figure 5.13(b), which is detrimental to the properties of the panel.

The cracking in the VHP 113 panel was disappointing, as no matrix cracking was predicted with the lower volume fraction of ~11%. In this case, the lower fiber volume fraction should decrease the residual stresses resulting from the thermal mismatch. However, in the mechanical testing of the consolidated “fiber-less” plies, this material did not yield plastically at all, as was noted in Section 3.2. The already limited room temperature ductility of this alloy may be decreased even further during consolidation attempts with the foil sheets of the material. The quality of consolidation can also vary with these foil sheets, which was also noted in Section 3.2. These factors could lead to the matrix cracking that was seen during cool-down, as the thermal mismatch is too great for the thin foil sheets with the high limited room temperature ductility. The procedure used to manufacture the thin foil material and consolidate it with the fibers needs to be optimized in order to ensure successful and repeatable laminate consolidation.

## CHAPTER 6

### CONCLUSIONS

This research considered a gamma titanium aluminide for use at elevated temperatures, in applications such as skin materials in future hypersonic vehicles. The CTE of the alloy was determined using a dilatometer. Monotonic testing was conducted on rolled sheet material samples of the alloy at room temperature, 700°C, and 800°C to obtain material properties. Monotonic testing was also conducted on specimens exposed to elevated temperatures (700°C and 800°C) for 5 hours to determine the degradation effects of high temperature exposure and oxidation. Analytical modeling was conducted to evaluate the residual stress state after composite consolidation due to thermal mismatch and potential mechanical behavior of  $[0]_4$  laminates with a  $\gamma$ -MET matrix. Silicon carbide (Ultra-SCS) and alumina (Nextel 610) fibers were selected as reinforcing materials. Two coupons of SCS-6/ $\gamma$ -MET with different fiber volume fractions were manufactured.

The experimental testing included dilatometry work as well as monotonic tensile testing at various temperatures on as-received specimens and specimens exposed to elevated temperatures. The following were significant findings:

- The CTE of the  $\gamma$ -MET alloy ( $8.50\text{E-}6$  /°C) was significantly higher than the Ultra-SCS silicon carbide fiber ( $3.56\text{E-}6$  /°C), such that thermal mismatch would be a problem in composites.

- A Poisson ratio of 0.237 was measured at room temperature with a 0°/90° strain gage rosette.
- The alloy has low room temperature ductility, with total strain just under 1% and inelastic strain of 0.4%. The ductility increases with elevated temperatures, with inelastic strain of 2.23% at 700°C and greater than 20% at 800°C.
- The toughness of the alloy increases at higher temperatures, as its ductility increases while it retains much of its room temperature tensile strength and stiffness.
- Fracture surface analysis showed cleavage fracture at room temperature.
- Exposure for only 5 hours at 800°C caused the alloy to form a thin brittle oxide layer. Exposure at 700°C for 5 hours caused minimal visible oxide uptake.
- The minimal exposure of only 5 hours at either 700°C or 800°C caused a significant reduction in room temperature ductility, and an increase in tensile strength.
- Elevated temperature exposure did not significantly affect the mechanical properties of the alloy when tested at elevated temperatures.
- A maximum use temperature of 700°C is suggested for high temperature applications. Above this threshold, formation of an oxide scale becomes a factor.

Modeling was conducted to predict the residual stresses that would occur due to thermal mismatch during composite consolidation of a laminate with a  $\gamma$ -MET matrix.

An  $[0]_4$  lay-up was chosen for the model to mimic the concurrent consolidation attempts. Alumina (Nextel 610) fibers and silicon carbide (Ultra-SCS) fibers were compared as reinforcing materials. Potential composite behavior to loading after consolidation was also predicted. Since viscoplastic parameters were not available, the analysis was conducted using AGLPLY. The following were significant findings from the analytical modeling:

- The “lock-up” temperature of the matrix and fibers was calculated to be around 925°C.
- Modeling of consolidation trials with a 30% fiber content predicted in high residual stresses matrix yielding in the Ultra-SCS/ $\gamma$ -MET laminate and high residual stress in the Nextel 610/ $\gamma$ -MET laminate. Because the matrix is brittle at room temperature, cracking is expected above the yield point.
- With a higher CTE, the Nextel 610 is a closer thermal match with the  $\gamma$ -MET alloy, and lower residual stresses develop as a result.
- For laminates with Ultra-SCS reinforcement, it was predicted that a maximum of ~10% fiber content could be added, resulting in a laminate with an elastic modulus of 181 GPa and a maximum load capacity of 315 MPa at room temperature without yielding in the matrix.
- For laminates with Nextel 610 reinforcement, it was predicted that up to a ~30% fiber content could be added, resulting in an effective modulus of 214 GPa and a maximum load capacity of 312 MPa at room temperature without yielding in the matrix.

- From this analysis, it appears that Nextel 610/ $\gamma$ -MET offers the potential for a stronger composite system, assuming optimal matrix properties could be achieved.

Finally, attempts were made to manufacture coupons of an SCS-6/ $\gamma$ -MET laminate with two different volume fractions. The temperature at which the 103.4 MPa (15 ksi) of pressure applied during consolidation was released varied with the different attempts. From these composite consolidation attempts, the following observations are significant:

- Even with low fiber volume fractions of about 20% and 10%, transverse cracking occurred in the matrix due to the thermal mismatch between the laminate constituents.
- Observations of foil fabrication and consolidation indicate that this process must be optimized to achieve optimal matrix room temperature ductility in order to successfully manufacture  $\gamma$ -MET matrix composites.

## CHAPTER 7

### RECOMMENDATIONS

There are many areas for further investigation into the properties of gamma titanium aluminides and their composite systems. Research is needed to further understand the behavior of this alloy and its response to elevated temperature exposure. Further work is also necessary in the composite area to address the thermal mismatch with reinforcing fibers for this TMC to become a viable structural material.

The degradation of room temperature ductility of this alloy with a modest elevated temperature exposure time of 5 hours demonstrates a need for development of a protective coating for this alloy at elevated temperatures. At the conclusion of this research, the next generation of this alloy, in this case called  $\gamma$ -MET-px, has already been developed and is undergoing mechanical characterization testing at the AFRL [94]. This next generation alloy has been modified to improve the room temperature ductility, creep resistance, and oxidation resistance amongst other mechanical property improvements. A next step after mechanical characterization of this next generation alloy would be to incorporate the mechanical property data into an analytical model to evaluate its potential use as a matrix material in advanced TMCs.

For the alloy examined,  $\gamma$ -MET, time dependent effects of the sheet material should also be evaluated. With this data, viscoplastic effects can then be incorporated into the analysis, and more accurate composite modeling could occur. In a possible application as a structural material for hypersonic vehicles, mechanical and thermal

cycling would be expected. For this reason, additional testing should also investigate fatigue behavior of the alloy over the spectrum of usage temperatures.

This research began the exploration of the effect of elevated temperature exposure on this alloy, however additional testing is necessary. Additional tests are needed to ensure the repeatability of the experimental results from the monotonic tensile tests. Also, fatigue testing should be conducted on specimens exposed to high temperatures in order to determine if any resulting degradation occurs at either room temperature or elevated temperatures.

Of the two composite systems analyzed in this research,  $\gamma$ -MET/Nextel 610 showed the better potential for structural applications because they are a better thermal match than the  $\gamma$ -MET/Ultra-SCS system. However, the small diameter of these fibers somewhat limits their practical use when attempting to manufacture laminates. Therefore it would be beneficial to investigate other fibers with a higher CTE and a larger diameter. The manufacturing results showed that even with a 10% volume fraction of SCS-6 fibers in the  $\gamma$ -MET matrix that thermal mismatch is still a significant problem with this alloy. If the thermal mismatch cannot be overcome, then investigations should pursue other titanium classes, such as the more compatible orthorhombic class of titanium aluminides, as matrix materials in advanced TMCs.

## REFERENCES

1. Butkus, L., "Review of the Columbia Accident Investigation." *Seminar at the Woodruff School of Engineering, Georgia Institute of Technology*, March 3, 2004.
2. NASA. *The Vision for Space Exploration*. February 2004. Retrieved Nov. 11, 2004, from [http://www.nasa.gov/pdf/55584main\\_vision\\_space\\_exploration-hires.pdf](http://www.nasa.gov/pdf/55584main_vision_space_exploration-hires.pdf)
3. Appel, F., et al., "Recent Progress in the Development of Gamma Titanium Aluminide Alloys." *Advanced Engineering Materials*, 2000. **2**(11): p. 699-720.
4. Appel, F. and R. Wagner, "Microstructure and Deformation of Two-Phase Gamma Titanium Aluminides." *Materials Science and Engineering A*, 1998. **22**(5): p. 187-268.
5. Clemens, H. and H. Kestler, "Processing and Applications of Intermetallic  $\gamma$ -TiAl Based Alloys." *Advanced Engineering Materials*, 2000. **2**(9): p. 551-570.
6. Lipsitt, H.A., "Titanium Aluminides - An Overview." *Material Resource Society Symposium Proceedings*, 1985. **39**: p. 351-364.
7. Scotti, S.J., C. Clay, and M. Rezin, "Structures and Material Technologies for Extreme Environments Applied to Reusable Launch Vehicles," in *AIAA/ICAS International Symposium and Exposition*. 2003, American Institute of Aeronautics and Astronautics: Dayton, OH.
8. Bertin, J.J. and R.M. Cummings, "Fifty Years of Hypersonics: Where We've Been, Where We're Going." *Progress in Aerospace Sciences*, 2003. **39**: p. 511-536.
9. Pike, J. *X-30 National Aerospace Plane (NASP)*. 1997. FAS Intelligence Resource Program: Mystery Aircraft. Retrieved December 7, 2004, from <http://www.fas.org/irp/mystery/nasp.htm>
10. Strauss, B. and J. Hulewicz, "X-33 Advanced Metallic Thermal Protection System." *Advanced Materials & Processes*, 1997. **151**(5): p. 55-56.
11. NASA. *X-34: Demonstrating Reusable Launch Vehicle Technologies*. October 1999. Fact Sheet Number FS-1999-10-137-MSFC. Retrieved December 7, 2004, from <http://www1.msfc.nasa.gov/NEWSROOM/background/facts/x-34.html>
12. NASA. *X-37 Technology Demonstrator: Blazing the Trail for the Next Generation of Space Transportation Systems*. September 2003. FS-2003-09-121-



- MFSC. Retrieved December 8, 2004, from <http://www1.msfc.nasa.gov/NEWSROOM/background/facts/x37-historical.pdf>
13. NASA. *NASA Hyper-X Program Demonstrates Scram-Jet Technologies: X-43A Flight Makes Aviation History*. October 2004. FS-2004-10-98-LaRC. Retrieved December 8, 2004, from [http://www.nasa.gov/pdf/67456main\\_X-43A\\_Fa.pdf](http://www.nasa.gov/pdf/67456main_X-43A_Fa.pdf)
  14. *Report of the President's Commission on Implementation of United States Space Exploration Policy: A Journey to Inspire, Innovate, and Discover*. June 2004. Retrieved December 8, 2004, from [http://www.nasa.gov/pdf/60736main\\_M2M\\_report\\_small.pdf](http://www.nasa.gov/pdf/60736main_M2M_report_small.pdf)
  15. Morris, W.D., N.H. White, and E. C.E., *Analysis of Shuttle Orbiter Reliability and Maintainability for Conceptual Studies*, in *Space Programs and Technologies Conference*. 1996, AIAA Paper 96-4245: Huntsville, AL.
  16. Kelly, H.N. and M.L. Blosser, "Active Cooling from the Sixties to NASP." *Current Technology for Thermal protection systems*, 1992. NASA(CP 3157).
  17. NASA. *X-33's Innovative Metallic Thermal Shield 'Ready for Flight'*. 1999. Retrieved December 14, 2004, from <http://www1.msfc.nasa.gov/NEWS/news/photos/1999/photos99-022.htm>
  18. Loria, E.A., "Gamma Titanium Aluminides as Prospective Structural Materials." *Intermetallics*, 2000. **8**(9-11): p. 1339-1345.
  19. Loria, E.A., "Quo Vadis Gamma Titanium Aluminide." *Intermetallics*, 2001. **9**(12): p. 997-1001.
  20. Bartolotta, P.A. and D.L. Krause, "Titanium Aluminide Applications in the High Speed Civil Transport (HSCT)," in *Gamma Titanium Aluminides 1999*, Y.W. Kim, D.M. Dimiduk, and M.H. Loretto, Editors. 1999, TMS: Warrendale, PA. p. 3-10.
  21. Mallick, P.K., *Fiber-Reinforced Composites: Materials, Manufacturing, and Design*. 2nd ed. 1993, New York: Marcel Dekker, Inc.
  22. Johnson, W.S., "Fatigue Testing and Damage Development in Continuous Fiber Reinforced Metal Matrix Composites, ASTM STP 1032," in *Metal Matrix Composites: Testing, Analysis, and Failure Modes*, W.S. Johnson, Editor. 1989, American Society for Testing and Materials: Philadelphia, PA. p. 194-221.
  23. Mall, S., T. Fecke, and M.A. Foringer, "Introduction," in *Titanium Matrix Composites: Mechanical Behavior*, S. Mall and T. Nicholas, Editors. 1998, Technomic Publishing: Lancaster, PA. p. 1-22.
  24. Jin, O. and W.S. Johnson, "Role of Oxidation on the Thermomechanical Fatigue of Timetal(R)21S Matrix Composites," in *Thermomechanical Behavior of*

- Material, ASTM STP 1371*, H. Sehitoglu and H.J. Maier, Editors. 2000, American Society for Testing and Materials: West Conshohocken, PA. p. 204-220.
25. Parris, W.M. and P.J. Bania, "Oxygen Effects on the Mechanical Properties of Timetal(R)21s," in *Titanium '92: Science and Technology*. 1993. p. 153-160.
  26. Smith, P.R. and A.H. Rosenberger, "Orthorhombic Titanium Aluminide Metal Matrix Composites (O TMCs) - A Review." *Report # AFRL-ML-WP-TR-2000-4083*, 1999.
  27. Johnson, W.S., S.J. Lubowinski, and A.L. Highsmith, "Mechanical Characterization of Unnotched SCS6/Ti-15-3 Metal Matrix Composites at Room Temperature," in *Symposium on Thermal and Mechanical Behavior of Metal Matrix and Ceramic Matrix Composites, ASTM STP 1080*, J.M. Kennedy, H.H. Moeller, and W.S. Johnson, Editors. 1990, American Society for Testing and Materials: Philadelphia, PA. p. 193-218.
  28. Nimmer, R.P., "Fiber-Matrix Interface Effects in the Presence of Thermally Induced Residual Stress." *Journal of Composites Technology & Research*, 1990. **12**(2): p. 65-75.
  29. Newaz, G.M., "Monotonic Response," in *Titanium Matrix Composites: Mechanical Behavior*, S. Mall and T. Nicholas, Editors. 1998, Technomic Publishing: Lancaster, PA. p. 23-68.
  30. Gabb, T.P., J. Gayda, P.A. Bartolotta, and M.G. Castelli, "A Review of Thermomechanical Fatigue Damage Mechanisms in Titanium and Titanium Aluminide Matrix Composites." *International Journal of Fatigue*, 1993. **15**: p. 413-422.
  31. Neu, R.W. and I. Roman, "Acoustic Emission Monitoring of Damage in Metal Matrix Composites Subjected to Thermomechanical Fatigue." *Composites Science and Technology*, 1994. **52**: p. 1-8.
  32. Mirdamadi, M., W.S. Johnson, Y.A. Bahei-El-Din, and M.G. Castelli, "Analysis of Thermomechanical Fatigue of Unidirectional Titanium Metal Matrix Composites," in *Composite Materials: Fatigue and Fracture, Fourth Volume, ASTM STP 1156*, W.W. Stinchcomb and N.E. Ashbaugh, Editors. 1993, American Society for Testing and Materials: Philadelphia, PA. p. 591-607.
  33. Pollock, W.D. and W.S. Johnson, "Characterization of Unnotched SCS-6/Ti-15-3 Metal Matrix Composites at 650C," in *Composite Materials: Testing and Design, ASTM STP 1120*, G.C. Grimes, Editor. 1992, American Society for Testing and Materials: Philadelphia. p. 175-191.
  34. Mall, S. and J.J. Schubbe, "Thermomechanical Fatigue Behavior of a Cross-Ply SCS-6/Ti-15-3 Metal Matrix Composite." *Composite Science and Technology*, 1994. **50**: p. 49-57.

35. Neu, R.W. and T. Nicholas, "Thermomechanical Fatigue of SCS-6/TIMETAL Under Out-of-Phase Loading," in *Proceedings of the 1993 ASME Winter Annual Meeting: Thermomechanical Behavior of Advanced Structural Materials*. 1993, American Society of Mechanical Engineers. p. 97-111.
36. Foulk III, J.W., D.H. Allen, and K.L.E. Helms, "A Model for Predicting the Damage and Environmental Degradation Dependent Life of SCS-6/Timetal(R)21S [0]4 Metal Matrix Composite." *Mechanics of Materials*, 1998. **29**: p. 53-68.
37. Bigelow, C.A., "Thermal Residual Stresses in a Silicon-Carbide/Titanium [0/90] Laminate." *Journal of Composites Technology & Research*, 1993. **15**(4): p. 304.
38. Nicholas, T., "An Approach to Fatigue Life Modeling in Titanium Matrix Composites." *Materials Science and Engineering A*, 1995. **20**: p. 28-37.
39. Neu, R.W., D. Coker, and T. Nicholas, "Cyclic Behavior of Unidirectional and Cross-Ply Titanium Matrix Composites." *International Journal of Plasticity*, 1996. **12**(3): p. 361-385.
40. Neu, R.W., "Life Prediction of Cross-Ply Metal Matrix Composites Undergoing Thermomechanical Fatigue." *Fatigue & Fracture of Engineering Materials & Structures*, 1998. **21**: p. 130-139.
41. Chamis, C.C., P.L.N. Murthy, and D.A. Hopkins, "Computational Simulations of High Temperature Metal Matrix Composites Cyclic Behavior," in *Thermal and Mechanical Behavior of Metal Matrix and Ceramic Matrix Composites*, ASTM STP 1080, J.M. Kennedy, H.H. Moeller, and W.S. Johnson, Editors. 1990, American Society for Testing and Materials: Philadelphia, PA. p. 56.
42. Dvorak, G.J. and Y.A. Bahei-El-Din, "Plasticity Analysis of Fibrous Composites." *Journal of Applied Mechanics*, 1982. **49**(2): p. 327-335.
43. Majumdar, B.S. and G.M. Newaz, "Inelastic Deformation of Metal Matrix Composites: Plasticity and Damage Mechanisms." *Philosophical Magazine*, 1992. **A66**(2): p. 187.
44. Johnson, W.S., M. Mirdamadi, and Y.A. Bahei-El-Din, "Stress-Strain Analysis of a [0/90]<sub>2s</sub> Titanium Matrix Laminate Subjected to a Generic Hypersonic Flight Profile." *Journal of Composites Technology & Research*, 1993. **15**(4): p. 297-303.
45. Mirdamadi, M. and W.S. Johnson, "Prediction of Stress-Strain Response of SCS-6/Timetal-21S Subjected to a Hypersonic Flight Profile." *Composites Part A*, 1996. **27A**: p. 1033-1040.
46. Bahei-El-Din, Y.A., *User's Manual: AGLPLY Computer Program for Elastic-Plastic Analysis of Composite Laminates Under Thermomechanical Loads*. 1989, Troy, NY: Dept of Civil Engineering, Rensselaer Polytechnic Institute.

47. Bigelow, C.A., W.S. Johnson, and R.A. Naik, "A Comparison of Various Micromechanics Models for Metal Matrix Composites," in *Mechanics of Composite Materials and Structures*, Reddy and Teply, Editors. 1989, ASME. p. 21-31.
48. Kim, Y.W., "Ordered Intermetallic Alloys, Part III: Gamma Titanium Aluminides." *JOM*, 1994. **46**(7): p. 30-39.
49. Lipsitt, H.A., D. Shechtman, and R.E. Schafrik, "The Deformation and Fracture of TiAl at Elevated Temperatures." *Metallurgical and Materials Transactions A*, 1975. **6**: p. 1991-1996.
50. Al-Haik, M.S. and H. Garmestani, "A Composite Cylinder Model for the Prediction of Residual Stresses in Gamma-Titanium Composites." *Journal of Materials Engineering and Performance*, 2002. **11**(5): p. 530-536.
51. Dixon, D. and J.W. Newkirk, "Gamma-Titanium Aluminide Reinforced with Al<sub>2</sub>O<sub>3</sub> and TiB<sub>2</sub> fibers," in *Materials Research Society Symposium Proceedings*. 1993. p. 1063-1068.
52. Garmestani, H., M. Al-Haik, T.A. Townsley, and C. Sabinash, "Residual Stress Development During Fabrication and Processing of Gamma-Titanium Based Composites." *Scripta Materialia*, 2001. **44**(1): p. 179-185.
53. Papakonstantinou, C.G., P. Balaguru, and R.E. Lyon, "Comparative Study of High Temperature Composites." *Composites Part B*, 2001. **32**: p. 637-649.
54. Weber, C.H., et al., "Creep and Fracture Resistance of Gamma-TiAl Reinforced with Al<sub>2</sub>O<sub>3</sub> Fibers." *Acta Metallurgica et Materialia*, 1993. **41**(9): p. 2681.
55. Vassel, A., "Continuous Fibre Reinforced Titanium and Aluminum Composites: A Comparison." *Materials Science and Engineering A*, 1999. **A263**(2): p. 305-313.
56. Kim, Y.-W., "Gamma Titanium Aluminides: Their Status and Future." *JOM*, 1995. **47**(7): p. 39-41.
57. Moll, J.H., C.F. Yolton, and B.J. McTiernan, "P/M Processing of Titanium Aluminides." *International Journal of Powder Metallurgy*, 1990. **26**(2): p. 149-155.
58. Zhao, L., J. Beddoes, P. Au, and W. Wallace, "Evaluations of P/M Gamma Titanium Aluminides." *Advanced Performance Materials*, 1997. **4**: p. 421-434.
59. Clemens, H., H. Kestler, N. Eberhardt, and W. Knabl, "Processing of  $\gamma$ -TiAl Based Alloys on an Industrial Scale," in *Gamma Titanium Aluminides 1999*, Y.W. Kim, D.M. Dimiduk, and M.H. Loretto, Editors. 1999, TMS: Warrendale, PA. p. 209-222.

60. Seetharaman, V. and S.L. Semiatin, "Microstructures and Tensile Properties of Ti-45.5Al-2Nb-2Cr Rolled Sheets." *Materials Science and Engineering A*, 2001. **299**(1-2): p. 195-209.
61. Clemens, H., et al., "Processing, Properties and Applications of Gamma Titanium Aluminide Sheet and Foil Materials," in *Proceedings of the 1996 MRS Fall Meeting, Dec 2-5 1996*. 1997, Materials Research Society, Pittsburgh, PA, USA: Boston, MA, USA. p. 29-43.
62. LeHolm, R., H. Clemens, and H. Kestler, "Powder Metallurgy (PM) Gamma-Based Titanium Aluminide Structures for Use in Various High Temperature Aerospace Applications," in *Gamma Titanium Aluminides 1999*, Y.W. Kim, D.M. Dimiduk, and M.H. Loretto, Editors. 1999, TMS: Warrendale, PA. p. 25-33.
63. LeHolm, R., B. Norris, and A. Gurney, "High Temperature Alloys for Aerospace Structures." *Advanced Materials and Processes*, 2001. **159**(5): p. 27-31.
64. Kim, Y.-W., "Intermetallic Alloys Based on Gamma Titanium Aluminide." *JOM*, 1989. **41**(7): p. 24-30.
65. Chan, K.S. and D.S. Shih, "Fundamental Aspects of Fatigue and Fracture in a TiAl Sheet Alloy." *Metallurgical and Materials Transactions A*, 1998. **29A**(1): p. 73-87.
66. Gnanamoorthy, R., Y. Mutoh, N. Masahashi, and M. Matsuo, "High Temperature Strength and Fracture Toughness in  $\gamma$ -Phase Titanium Aluminides." *Journal of Materials Science*, 1993. **28**(24): p. 6631-6638.
67. Chan, K.S. and Y.W. Kim, "Influence of Microstructure on Crack-Tip Micromechanics and Fracture Behaviors of a Two-Phase TiAl Alloy." *Metallurgical Transactions A*, 1992. **23A**(6): p. 1663-1677.
68. Gnanamoorthy, R., Y. Mutoh, N. Masahashi, and Y. Mizuhara, "Fracture Properties of  $\gamma$ -Based TiAl Alloys with Lamellar Microstructure at Room Temperature." *Materials Science and Engineering A*, 1994. **A184**(1): p. 37-44.
69. Becker, S., a. Rahmel, M. Schorr, and M. Schutze, "Mechanism of Isothermal Oxidation of the Intermetallic TiAl and of TiAl Alloys." *Oxidation of Metals*, 1992. **38**(5/6): p. 425-464.
70. Meier, G.H., "Fundamentals of the Oxidation of High-Temperature Intermetallics," in *Oxidation of High-Temperature Intermetallics*, T. Grobstein and J. Doychak, Editors. 1989, TMS. p. 1-15.
71. Brady, M.P., W.J. Brindley, J.L. Smialek, and I.E. Locci, "The Oxidation and Protection of Gamma Titanium Aluminides." *JOM*, 1996. **48**(11): p. 46-50.

72. Dowling, W.E. and W.T. Donlon, "The Effect of Surface Film Formation from Thermal Exposure on the Ductility of Ti-48Al-1V-0.2C(at%)." *Scripta Metallurgica et Materialia*, 1992. **27**: p. 1663-1668.
73. Pather, R., et al., "The Effect of High Temperature Exposure on the Tensile Properties of  $\gamma$ -TiAl Alloys." *Intermetallics*, 2003. **11**(10): p. 1015-1027.
74. Kelly, T.J., C.M. Austin, P.J. Fink, and J. Schaeffer, "Effect of Elevated Temperature Exposure on Cast Gamma Titanium Aluminide (Ti-48Al-2Cr-2Nb)." *Scripta Metallurgica et Materialia*, 1994. **30**(9): p. 1105-1110.
75. Lee, D.S., M.A. Stucke, and D.M. Dimiduk, "Effects of Thermal Exposure on the Properties of Two  $\gamma$ -Alloys." *Materials Science and Engineering A*, 1995. **192-193**(2): p. 824-829.
76. Planck, S.K. and A.H. Rosenberger, "The Effects of Prolonged High Temperature Air Exposure on the Monotonic and Cyclic Properties of a Gamma Titanium Aluminide Alloy," in *Gamma Titanium Aluminides 1999*, Y.W. Kim, D.M. Dimiduk, and M.H. Loretto, Editors. 1999, TMS: Warrendale, PA. p. 791-798.
77. Chatterjee, A., et al., "Mechanical Properties of Heat Treated Gamma TiAl Sheet Material," in *Gamma Titanium Aluminides 1999*, Y.W. Kim, D.M. Dimiduk, and M.H. Loretto, Editors. 1999, TMS: Warrendale, PA. p. 401-408.
78. LeHolm, R., H. Clemens, H. Kestler, and P.A. Bartolotta, "Gamma-Based Titanium Aluminide Sheet and Foil Structures for Use in High Temperature Aerospace Environments," in *Titanium '99: Science and Technology*. 1999: St. Petersburg, Russia. p. 269-277.
79. Craft, J.S., "Evaluation of Advanced Titanium Matrix Composites for 3rd Generation Reusable Launch Vehicles," in *Woodruff School of Mechanical Engineering*. 2003, Georgia Institute of Technology: Atlanta, GA.
80. Hales, S.J., M. Saquib, and J.A. Alexa, "An Innovative Method for Manufacturing  $\gamma$ -TiAl Foil," in *Gamma Titanium Aluminides 2003*, K. Y-W., H. Clemens, and A.H. Rosenberger, Editors. 2003, TMS (The Minerals, Metals & Materials Society): San Diego, CA. p. 257-264.
81. Planck, S.K. and A.H. Rosenberger, "The Influence of High Temperature Exposure on the Mechanical Performance of a  $\gamma$  Titanium Aluminide Alloy." *Materials Science and Engineering A*, 2002. **325**(1-2): p. 270-280.
82. Pippan, R., et al., "Fatigue Threshold and Crack Propagation in  $\gamma$ -TiAl Sheets." *Intermetallics*, 2001. **9**(1): p. 89-96.
83. Bird, K., T. Wallace, and S. Sankaran, "Development of Protective Coatings for High-Temperature Metallic Materials," in *Elevated Temperature Coatings*:

- Science and Technology IV*. 2001, Minerals, Metals and Materials Society/AIME: New Orleans, LA. p. 181-196.
84. Alexa, J.A. Personal communication at NASA LaRC, 12/17/2003.
  85. Church, B.C., *Fabrication and Characterization of Solid Oxide Fuel Cell Interconnect Alloys*, in *School of Materials Science and Engineering*. 2004, Georgia Institute of Technology: Atlanta, GA.
  86. James, J.D., J.A. Spittle, S.G.R. Brown, and R.W. Evans, "A Review of Measurement Techniques for the Thermal Expansion Coefficient of Metals and Alloys at Elevated Temperatures." *Measurement Science and Technology*, 2001. **12**: p. R1-R15.
  87. "ASTM E1237-93, Standard Guide for Installing Bonded Resistance Strain Gauges," in *Annual Book of ASTM Standards*. 1999, ASME: West Conshohocken, PA.
  88. "ASTM E21-92, Standard Test Methods for Elevated Temperature Tests of Metallic Materials," in *Annual Book of ASTM Standards*. 2001, ASME: West Conshohocken, PA.
  89. Johnson, W.S., "Modeling Stiffness Loss in Boron/Aluminum Laminates Below the Fatigue Limit," in *Long-Term Behavior of Composites*, ASTM STP 813, T.K. O'Brien, Editor. 1983, American Society for Testing and Materials: Philadelphia, PA. p. 160-176.
  90. *3M Metal Matrix Composites Technical Data: Nextel 610*. Retrieved June 10, 2004, from <http://www.3m.com/market/industrial/mmc/nextel.html>
  91. Askeland, D.R., *The Science and Engineering of Materials*, 3rd Ed. 1994, Boston, MA: PWS Publishing Co., p. 743-746.
  92. Kroupa, J.L., et al., "Comparison of Analysis Tools for Predicting the Inelastic Cyclic Response of Cross-Ply Titanium Matrix Composites, ASTM STP 1253," in *Life Prediction Methodology for Titanium Matrix Composites*, W.S. Johnson, J.M. Larsen, and B.N. Cox, Editors. 1996, American Society for Testing and Materials: Philadelphia, PA. p. 297-327.
  93. Bird, K. Personal communication at NASA LaRC, 12/15/2003.
  94. Bartolotta, P.A. "Titanium Aluminide Applications for Hypersonic Systems." in *Aeromat 2004 Conference and Exposition*. Seattle, WA: ASM International.